

RIGHT VENTRICLE SEGMENTATION USING CARDIAC MAGNETIC RESONANCE  
IMAGES

by

José A. Rosado-Toro

---

Copyright © José A. Rosado-Toro 2016

A Dissertation Submitted to the Faculty of the

DEPARTMENT OF ELECTRICAL AND COMPUTER ENGINEERING

In Partial Fulfillment of the Requirements

For the Degree of

DOCTOR OF PHILOSOPHY

In the Graduate College

THE UNIVERSITY OF ARIZONA

2016

THE UNIVERSITY OF ARIZONA  
GRADUATE COLLEGE

As members of the Dissertation Committee, we certify that we have read the dissertation prepared José A. Rosado-Toro, titled Right Ventricle Segmentation using Cardiac Magnetic Resonance Images and recommend that it be accepted as fulfilling the dissertation requirement for the Degree of Doctor of Philosophy.

\_\_\_\_\_  
Jeffrey J. Rodríguez Date: 5-17-2016

\_\_\_\_\_  
María I. Altbach Date: 5-17-2016

\_\_\_\_\_  
Ali Bilgin Date: 5-17-2016

\_\_\_\_\_  
Michael M. Marefat Date: 5-17-2016

Final approval and acceptance of this dissertation is contingent upon the candidate's submission of the final copies of the dissertation to the Graduate College.

I hereby certify that I have read this dissertation prepared under my direction and recommend that it be accepted as fulfilling the dissertation requirement.

\_\_\_\_\_  
Dissertation Director: Jeffrey J. Rodríguez Date: 5-17-2016

## STATEMENT BY AUTHOR

This dissertation has been submitted in partial fulfillment of the requirements for an advanced degree at the University of Arizona and is deposited in the University Library to be made available to borrowers under rules of the Library.

Brief quotations from this dissertation are allowable without special permission, provided that an accurate acknowledgement of the source is made. Requests for permission for extended quotation from or reproduction of this manuscript in whole or in part may be granted by the head of the major department or the Dean of the Graduate College when in his or her judgment the proposed use of the material is in the interests of scholarship. In all other instances, however, permission must be obtained from the author.

SIGNED: José A. Rosado-Toro

## ACKNOWLEDGMENTS

First I wish to thank Dr. Jeffrey Rodríguez. Thank you for allowing me to achieve my dream of pursuing a PhD degree. When I needed help you were able to put me in the right path.

Dr. María Altbach, thank you for pushing me to the finish line. Your support and guidance has been invaluable.

Dr. Ali Bilgin, thank you for introducing me to dynamic programming. It was in your class that I first learned of this technique, which is the basis of my dissertation.

Dr. Michael Marefat, thank you for being a friend. Your course of computing graphics helped me with my dissertation immensely.

Dr. Ryan Avery, thank you for your clinical insight and enthusiasm. When I was feeling down your positive attitude always cheered me up.

I also wish to thank Dr. Aiden Abidov and Dr. Isabel Oliva among the professors and mentors who helped me get to where I am today. I would also like to thank all my lab peers, in particular Sundaresh Ram and Tomoe Hagio. I also want to thank our great academic advisor Tami Whelan. She was never too busy to hear me out and give me great advice.

Finally, I wish to thank my parents and my wife, Glorimar Noriega. Without your love, understanding and support none of this would have been possible.

## TABLE OF CONTENTS

<b>LIST OF TABLES.....</b>	<b>8</b>
<b>LIST OF FIGURES.....</b>	<b>9</b>
<b>LIST OF ACRONYMS .....</b>	<b>11</b>
<b>ABSTRACT.....</b>	<b>12</b>
<b>1 INTRODUCTION.....</b>	<b>14</b>
1.1 CARDIAC IMAGING MODALITIES.....	16
1.1.1 <i>Echocardiography</i> .....	17
1.1.2 <i>Magnetic Resonance Imaging</i> .....	18
1.2 RV CARDIAC PATHOLOGIES .....	27
1.2.1 <i>Pulmonary Hypertension</i> .....	27
1.2.2 <i>Congestive Heart Failure</i> .....	28
1.2.3 <i>Congenital Heart Disease</i> .....	28
1.3 VENTRICULAR CARDIAC FUNCTION.....	29
1.3.1 <i>Imaging Planes</i> .....	29
1.3.1.1 SAX View.....	31
1.3.1.2 4CH View .....	31
1.3.2 <i>Stroke Volume</i> .....	31
1.3.3 <i>Ejection Fraction</i> .....	32
1.3.4 <i>Tricuspid Annular Plane Systolic Excursion</i> .....	32
1.3.5 <i>Fractional Area Change</i> .....	32
<b>2 DIGITAL IMAGE PROCESSING TECHNIQUES.....</b>	<b>33</b>
2.1 GRAPH THEORY .....	33
2.1.1 <i>Dijkstra's Shortest Path Algorithm</i> .....	35
2.1.2 <i>A* Algorithm</i> .....	35
2.1.3 <i>Dynamic Programming</i> .....	37
2.2 SEGMENTATION .....	38
2.2.1 <i>Active Contour Methods</i> .....	39
2.2.2 <i>Level Sets Method</i> .....	41
2.2.3 <i>Polar Dynamic Programming</i> .....	44
2.3 REVIEW OF STATE-OF-THE-ART SAX SEGMENTATION ALGORITHMS.....	45
2.3.1 <i>LV Segmentation Algorithms</i> .....	46
2.3.2 <i>RV Segmentation Algorithms</i> .....	46
<b>3 POLAR DYNAMIC PROGRAMMING USING POLAR VARIANCE .....</b>	<b>47</b>
3.1 ALGORITHM DESCRIPTION .....	47
3.1.1 <i>Polar Variance Image</i> .....	48
3.1.2 <i>Cost Function</i> .....	50
3.1.2.1 <i>Polar Resampling</i> .....	51
3.1.2.2 <i>Interpolation</i> .....	52
3.1.3 <i>Dynamic Programming</i> .....	53
3.1.4 <i>Optimizing for Multiple <math>\Delta\theta</math> Values</i> .....	54
3.1.5 <i>Localized Region Growing</i> .....	54
3.2 RESULTS AND ANALYSIS.....	56
3.2.1 <i>Parameter Selection</i> .....	56

3.2.2	<i>Sensitivity to Additive Gaussian Noise</i> .....	59
3.2.3	<i>Grayscale Images</i> .....	61
3.2.4	<i>Parameter Robustness</i> .....	65
3.3	CONCLUSION.....	69
<b>4</b>	<b>4CH RV SEGMENTATION USING DYNAMIC PROGRAMMING.....</b>	<b>70</b>
4.1	ALGORITHM DESCRIPTION .....	70
4.1.1	<i>Identify Cardiac Region of Interest</i> .....	71
4.1.2	<i>Identify landmarks in ED and ES frames</i> .....	74
4.1.3	<i>Propagate landmarks throughout the cardiac cycle</i> .....	74
4.1.4	<i>Identify Septum</i> .....	77
4.1.5	<i>Segment RV Using Landmarks</i> .....	78
4.1.5.1	Right Ventricular Region of Interest (RV-ROI).....	78
4.1.5.2	Outline the Free Wall .....	79
4.1.5.3	Identifying septum-BP border .....	81
4.1.6	<i>Incorporate Temporal Smoothness</i> .....	81
4.1.7	<i>Identifying Blood Pool</i> .....	81
4.2	MANUAL TRACING PROTOCOL.....	82
4.3	DATA AND PERFORMANCE METRICS.....	83
4.3.1	<i>Data</i> .....	83
4.3.2	<i>Performance Metrics</i> .....	83
4.3.3	<i>Parameter Selection</i> .....	84
4.4	RESULTS .....	85
4.5	ANALYSIS .....	92
4.6	CONCLUSION.....	95
<b>5</b>	<b>SAX RV SEGMENTATION USING DYNAMIC PROGRAMMING.....</b>	<b>96</b>
5.1	ALGORITHM DESCRIPTION .....	96
5.1.1	<i>Find geometric relationship between SAX and 4CH views</i> .....	98
5.1.2	<i>Segment 4CH LV epicardial border</i> .....	99
5.1.3	<i>Identify SAX Slices</i> .....	100
5.1.4	<i>Transform 4CH RV and LV Segmentation into SAX Slices</i> .....	102
5.1.5	<i>Identify ROI for each SAX Slice</i> .....	103
5.1.6	<i>Segment SAX LV</i> .....	105
5.1.6.1	Segment SAX LV Endocardial Border .....	105
5.1.6.2	Segment SAX LV Epicardial Border .....	106
5.1.7	<i>Segment SAX RV</i> .....	108
5.1.7.1	Reducing the ROI.....	108
5.1.7.2	Finding Rough Segmentation.....	109
5.1.7.3	Identifying Origin Candidates .....	111
5.1.7.4	Upgrade Gradient Image .....	112
5.1.7.5	Using PDP to Segment the RV.....	113
5.1.7.6	Joining Segmentation Masks.....	113
5.1.7.7	Refining Segmentation Masks.....	114
5.2	DATA AND PERFORMANCE METRIC .....	115
5.2.1	<i>Data Acquisition</i> .....	115
5.2.2	<i>Performance Metric</i> .....	115
5.3	RESULTS .....	115
5.4	ANALYSIS .....	117
5.5	CONCLUSION AND FUTURE WORK .....	119

**REFERENCES..... 120**

## LIST OF TABLES

TABLE 1.1 VELOCITY OF SOUND THROUGH DIFFERENT MEDIUMS. ....	17
TABLE 1.2 $T_1$ AND $T_2$ VALUES FOR HEART TISSUE COMPONENTS AT 1.5T. ....	21
TABLE 3.1 ALGORITHM SPECIFIC PARAMETERS. ....	58
TABLE 3.2 PERFORMANCE OF SEGMENTATION ALGORITHMS. ....	63
TABLE 3.3 ROBUSTNESS TO CHANGES IN ALGORITHM-SPECIFIC PARAMETERS. ....	67
TABLE 4.1 INTER-PHYSICIAN MANUAL TRACING PERFORMANCE. THIS TABLE SHOWS THE OVERLAP BETWEEN DIFFERENT TRAINED PHYSICIANS USING THE TRACING PROTOCOL (DESCRIBED IN THE MANUAL TRACING PROTOCOL SECTION) TO MANUALLY TRACE THE 4CH RV THROUGHOUT THE CARDIAC CYCLE. ....	85
TABLE 4.2 COMPARING PHYSICIAN MANUAL TRACING TO SEMI-AUTOMATED TRACING (RV AND BP) USING PHYSICIAN LANDMARKS. ....	86
TABLE 4.3 INTER-PHYSICIAN PERFORMANCE USING SEMI-AUTOMATED TECHNIQUES TO DO THE TRACING. THE TABLES CALCULATES THE MUTUAL OVERLAP WHEN COMPARING (A) SEMI-AUTOMATED RV MASKS AND (B) SEMI-AUTOMATED BLOOD POOL (BP) MASKS. ..	87
TABLE 4.4 COMPARISON OF FAC DERIVED FROM THREE DIFFERENT MEASUREMENTS; MANUAL TRACES, RV AND BP. ....	90
TABLE 4.5 R SCORE AND P VALUE USING FAC. (A) INTER-PHYSICIAN MANUAL TRACING PERFORMANCE, (B) PHYSICIAN MANUAL TRACING TO SEMI-AUTOMATED TRACING (RV AND BP) USING PHYSICIAN LANDMARKS, AND (C) INTER-PHYSICIAN PERFORMANCE USING SEMI-AUTOMATED TECHNIQUE TO DO THE TRACING. ....	91

## LIST OF FIGURES

FIGURE 1.1 EFFECT OF AN EXTERNAL MAGNETIC FIELD ( $B_0$ ) ON THE SPINS. (A) WHEN NO EXTERNAL MAGNETIC FIELD IS APPLIED THE SPINS ARE RANDOMLY ORIENTED. (B) IN THE PRESENCE OF AN EXTERNAL MAGNETIC FIELD, THE SPINS ALIGN WITH THE FIELD. (C) NET MAGNETIZATION OF THE SPINS IS NOW ALONG THE DIRECTION OF $B_0$ . NOTE THAT THERE IS NO NET MAGNETIZATION IN THE X-Y PLANE. ....	19
FIGURE 1.2 SIGNAL DEPHASING IN THE X-Y PLANE DUE TO $T_2^*$ RELAXATION MECHANISM. ....	20
FIGURE 1.3 SLICE SELECTION PROCESS. ....	22
FIGURE 1.4 CREATION OF AN MR IMAGE. ....	23
FIGURE 1.5 BALANCED STEADY STATE FREE PRECESSION (SSFP) PULSE SEQUENCE ILLUSTRATING THE SLICE SELECTION MODULE (YELLOW) AND THE GRADIENT WAVEFORMS USED TO TRAVERSE K-SPACE. ....	24
FIGURE 1.6 CARDIAC GATING PROCEDURE USED FOR CINE MRI. ....	26
FIGURE 1.7 COMMON MR IMAGING ANGLES. ....	30
FIGURE 1.8 VIEWING ANGLES USED FOR FUNCTIONAL RV ASSESSMENT. ....	30
FIGURE 2.1 3X3 NEIGHBORHOOD REPRESENTED USING VERTICES AND EDGES. ....	34
FIGURE 2.2 FINDING THE SHORTEST PATH USING DYNAMIC PROGRAMMING. ....	37
FIGURE 2.3 PARAMETRIC REPRESENTATION OF A CLOSED CONTOUR, $\mathcal{P}(0) = \mathcal{P}(1)$ . ....	39
FIGURE 2.4 VFK WITH RADII 4. ....	41
FIGURE 2.5 CHANGE IN PARAMETERIZATION FOR CURVE EVOLUTION USED BY CHAN-VESE. ....	42
FIGURE 2.6 CARTESIAN TO POLAR COORDINATE CHANGE. ....	45
FIGURE 3.1 GRAYSCALE AND POLAR VARIANCE IMAGES. (A) SAX CARDIAC MR IMAGE AND (B) HAND IMAGE. (C-D) POLAR VARIANCE IMAGES OF (A) AND (B) RESPECTIVELY. THE DOT DENOTES THE OBJECT WE WISH TO OUTLINE (RV IN (A), THE ENTIRE HAND IN (B)) AND IS USED TO CALCULATE THE POLAR VARIANCE IMAGE. BLACK IN THE POLAR VARIANCE IMAGES REPRESENTS LOW VARIANCE. ...	50
FIGURE 3.2 ASSESSING HOW $\Delta\theta$ AFFECTS CLOSED CONTOUR. FOR THIS EXAMPLE, A AND B EQUAL 0.5. THE DOT IS THE ORIGIN USED FOR PDP. RESULTS USING A $\Delta\theta$ OF (A) $5^\circ$ AND (B) $0.1^\circ$ . CLOSED CONTOURS HAVE BEEN DILATED FOR VIEWING PURPOSES. ....	52
FIGURE 3.3 PSEUDO CODE OF LOCALIZED REGION-GROWING (SECTION 3.1.5). ....	55
FIGURE 3.4 SIMULATED IMAGES WITH SNR VALUES OF (A) $\infty$ , (B) 5 dB AND (C) 0 dB. OUTLINE IN (A) IS THE INITIAL CLOSED CONTOUR USED FOR L2S, DRLSE, VFC AND CV; DOT IS THE ORIGIN LOCATION USED FOR PDP. CLOSED CONTOUR HAS BEEN DILATED FOR VIEWING PURPOSES. ....	60
FIGURE 3.5 NOISE SENSITIVITY PERFORMANCE ANALYSIS FOR (A) AVERAGE DICE PERFORMANCE AND (B) AVERAGE BORDER POSITIONING ERROR (BPE) IN PIXELS. ONE HUNDRED NOISY IMAGES WERE CREATED FOR EACH SNR LEVEL BY ADDING GAUSSIAN NOISE TO THE IMAGE SHOWN IN FIGURE 3.4A. ....	60
FIGURE 3.6 NON-MEDICAL AND MEDICAL IMAGES. FROM LEFT TO RIGHT (A) FLAG, (B) HAND, (C) HORSE, (D) RETINA, (E) SHORT-AXIS AND (F) 4CH CARDIAC IMAGE. UPPER ROW SHOWS THE INITIALIZATION FOR THE DIFFERENT ALGORITHMS. SHORT-AXIS CARDIAC IMAGES (E) HAVE BEEN CROPPED FOR DISPLAY PURPOSES. THE IMAGE USED FOR ANALYSIS IS SHOWN IN FIGURE 3.1A. CLOSED CONTOURS HAVE BEEN DILATED FOR VIEWING PURPOSES. ....	62
FIGURE 3.7 SCHEMATIC OF THE TAIL REGION OF THE HORSE SHOWN IN FIGURE 3.6C. THE THIN BLACK LINE REPRESENTS THE HIGH GRADIENT REGION AND THE WHITE BACKGROUND IS THE LOW GRADIENT REGION. (A) THE GRAY THICK LINE SHOWS PART OF THE HIGH GRADIENT EXTRACTED CONTOUR OF THE ORIGINAL MASK. THE BLACK THICK LINE IS THE WEAK SUB-CONTOUR. (B) THE DOT IS THE NEW ORIGIN POSITIONED IN THE MIDDLE OF THE WEAK SUB-CONTOUR SHOWN IN (A). (C) THE GRAY THICK LINE IS THE HIGH GRADIENT EXTRACTED CONTOUR THAT DOES NOT INTERSECT WITH THE ORIGINAL MASK, (A). ....	64
FIGURE 4.1 4CH SEGMENTATION FLOWCHART. MAGENTA DENOTES THE MODULE THAT REQUIRES USER INTERACTION; BLUE DENOTES OPTIONAL MODULES. ....	71
FIGURE 4.2 4CH CMR IMAGE AT (A) ED AND (B) ES. THE ZOOMED CARDIAC REGION OF INTEREST AT ED AND ES IS SHOWN IN (C) AND (D). THE RV ANATOMICAL LANDMARKS ARE ANNOTATED IN (C) AND (D). LANDMARKS THAT WILL BE SELECTED BY USERS OF THE TECHNIQUE ARE SHOWN AS CIRCLES IN (C) AND (D). ....	73
FIGURE 4.3 THE RV-ROI IS THE OVERLAP BETWEEN THE RECTANGLE CREATED BY LINES $L_1$ , $L_2$ , $L_3$ AND $L_4$ AND THE CARDIAC REGION OF INTEREST. ....	79

FIGURE 4.4 ES PHYSICIANS' TRACE. TRACE FROM PHYSICIAN 1 (IN RED) INCLUDES MOST OF THE TRABECULAE, WHILE THE OTHER TRACE (ORANGE) EXCLUDES MOST OF THE TRABECULAE.....	93
FIGURE 4.5 BP FAC FOR DIFFERENT USER-SELECTED LANDMARKS IN THE (A) ED AND (B) ES FRAME. THE OUTLINE IN GREEN YIELDED THE HIGHEST BP FAC, WHILE THE OUTLINE IN CYAN YIELDED THE LOWEST BP FAC. ....	94
FIGURE 5.1 SAX RV SEGMENTATION FLOWCHART. ....	97
FIGURE 5.2 LV EPICARDIAL BORDER (MAGENTA OUTLINE). ....	100
FIGURE 5.3 OVERLAP BETWEEN SAX AND 4CH VIEWS. THE YELLOW LINES SHOW HOW THE SAX VIEWS OVERLAP WITH THE 4CH VIEW. CMR IMAGES OF SAX VIEWS ARE SHOWN FROM THE BASE (UPPER LEFT FROM THE SAX STACKS) ALL THE WAY TO THE APEX (LOWER RIGHT FROM THE SAX STACKS). ....	102
FIGURE 5.4 4CH RV (CYAN) AND LV SEGMENTATION (MAGENTA) (A) DISPLAYED ONTO THE 4CH VIEW. (B) THE 4CH SEGMENTATIONS ARE ROTATED INTO SAX SLICES AND DISPLAYED AS LINES EACH OF THE SAX SLICES. LINES IN SAX SLICES HAVE BEEN DILATED FOR VIEWING PURPOSES. ....	103
FIGURE 5.5 IDENTIFYING SAX ROI. (A) AN IMAGE IN THE SAX VIEW; (B) STANDARD DEVIATION IMAGE FOR THE GIVEN SLICE; (C) THRESHOLDED STANDARD DEVIATION IMAGE; (D) ROI REDUCTION USING HORIZONTAL PROFILING; (E) ROI REDUCTION USING VERTICAL PROFILING AND (F) FINAL ROI USED FOR LV AND RV SEGMENTATION.....	105
FIGURE 5.6 SEGMENTATION OF LV ENDOCARDIAL BORDER. (A) CROPPED SAX VIEW OF REPRESENTATIVE SLICE; (B) BP REGIONS; (C) 4CH EPICARDIAL BORDER OF LV ON SAX VIEW; (D) LV BP REGION AND (E) LV ENDOCARDIAL BORDER.....	106
FIGURE 5.7 CHANGE OF COST FUNCTION AS EXPLAIN IN SECTION 5.1.6.2. ....	107
FIGURE 5.8 ROUGH SEGMENTATION FOR BASAL, MID-RV AND APICAL SLICES. ....	111
FIGURE 5.9 FINDING CANDIDATE ORIGINS IN REPRESENTATIVE SLICE IN THE ED FRAME. (A) BP REGIONS, (B) 4CH RV ROTATED INTO THE REPRESENTATIVE SAX SLICE (CYAN LINE), (C) BP REGION ASSOCIATED WITH THE RV, (D) DISTANCE TRANSFORM OF (C), (E) BINARY MASK OF DISTANCE TRANSFORM AND (F) CANDIDATE ORIGINS.....	112
FIGURE 5.10 GRADIENT IMAGE CREATION. (A) GRADIENT IMAGE, DEFINED BY (5.7), WHERE REGIONS THAT ARE OUTSIDE THE REDUCED ROI ARE REMOVED. (B) SETTING AIR PIXELS IN THE GRADIENT IMAGE TO 0, AND (C) HIGH GRADIENT VALUE GIVEN TO THE RIGHT LATERAL PORTION OF THE LV EPICARDIAL BORDER. ....	113
FIGURE 5.11 JOINING SEGMENTATION MASKS EXAMPLES. FOR THE BASAL SLICES, THE TECHNIQUE WILL ONLY PASS TWO MASKS WITH THE LARGEST AREA, WHILE IN THE APICAL SLICES IT WILL PASS THE NUMBER OF MASKS THAT MINIMIZE THE AMOUNT OF OVERLAP. ....	114
FIGURE 5.12 DICE METRIC FOR RV EPICARDIAL BORDER IN THE ED FRAME. THE SEMI-AUTOMATED RESULTS ARE SHOWN IN CYAN; MANUAL TRACE IN YELLOW. ....	116
FIGURE 5.13 14 DICE METRIC FOR RV EPICARDIAL BORDER IN THE ES FRAME. THE SEMI-AUTOMATED RESULTS ARE SHOWN IN CYAN; MANUAL TRACE IN YELLOW.....	117
FIGURE 5.15 PURPLE CIRCLES DENOTES BP REGIONS THAT FORM PART OF THE SAX RV SEGMENTATION AND ARE ADJACENT TO LV EPICARDIAL BORDER. RED CIRCLES DENOTE BP REGIONS THAT DO NOT FORM PART OF THE SAX RV SEGMENTATION BUT ARE ADJACENT TO THE LV EPICARDIAL BORDER.....	118

## LIST OF ACRONYMS

1D	One-dimensional	ESV	End-systolic volume	TE	Time to echo
2D	Two-dimensional	FAC	Fractional area change	TR	Time to repetition
3D	Three-dimensional	FT	Fourier transform	TV	Tricuspid valve
4CH	Four-chamber	GVF	Gradient vector field	US	Ultrasound
4D	Four-dimensional	L2S	Legendre level sets	VFC	Vector field convolution
ALCT	A* algorithm that uses length, curvature, torsion penalties	LV	Left ventricle	VFK	Vector field kernel
BP	Blood pool	MICCAI	Medical Image Computing and Computer-Assisted Intervention		
BPE	Border positioning error	MRI	Magnetic resonance imaging		
CHF	Congestive heart failure	PDP	Polar dynamic programming		
CMR	Cardiac Magnetic Resonance	PIG	Poisson inverse gradient		
CV	Chan-Vese	RA	Right atrium		
DIP	Digital image processing	RF	Radiofrequency		
DRLSE	Distance-regularized level-set evolution	ROI	region-of-interest		
EAOS	Equal area opposite sign	RV	Right ventricle		
ECG	Electrocardiogram	SAX	Short-axis		
ED	End-diastolic	sPDP	simple PDP		
EDV	End-diastolic volume	SSFP	Steady state free precession		
EF	Ejection Fraction	SV	Stroke Volume		
ES	End-systolic	TAPSE	Tricuspid annular plane systolic excursion		

## ABSTRACT

The world health organization has identified cardiovascular disease as the leading cause of non-accidental deaths in the world. The heart is identified as diseased when it is not operating at peak efficiency. Early diagnosis of heart disease can impact treatment and improve a patient's outcome. An early sign of a diseased heart is a reduction in its pumping ability, which can be measured by performing functional evaluations. These are typically focused on the ability of the ventricles to pump blood to the lungs (right ventricle) or to the rest of the body (left ventricle). Non-invasive imaging modalities such as cardiac magnetic resonance have allowed the use of quantitative methods for ventricular functional evaluation. The evaluation still requires the tracing of the ventricles in the end-diastolic and end-systolic phases. Even though manual tracing is still considered the gold standard, it is prone to intra- and inter-observer variability and is time consuming. Therefore, substantial research work has been focused on the development of semi- and fully automated ventricle segmentation algorithms.

In 2009 a medical imaging conference issued a challenge for short-axis left ventricle segmentation. A semi-automated technique using polar dynamic programming generated results that were within human variability. This is because a path in a polar coordinate system yields a circular object in the Cartesian grid and the left ventricle can be approximated as a circular object. In 2012 there was a right ventricle segmentation challenge, but no polar dynamic programming algorithms were proposed. One reason may be that polar dynamic programming can only segment circular shapes.

To use polar dynamic programming for the segmentation of the right ventricle we first expanded the capability of the technique to segment non-circular shapes. We apply this new polar dynamic programming in a framework that uses user-selected landmarks to segment the right ventricle in the four chamber view. We also explore the use of four chamber right ventricular segmentation to segment short-axis views of the right ventricle.

# 1 INTRODUCTION

The heart is an organ that uses a four-chambered double pump to circulate blood in the body [1]. The heart consists of two receiving chambers (atria) and two pumping chambers (ventricles). In humans, the right atrium receives deoxygenated blood from the body. When enough blood is inside the right atrium, pressure builds up, opening the tricuspid valve (TV), and delivering blood to the right ventricle (RV). The RV in turn sends blood to the lungs to get oxygenated. Once the blood is oxygenated, it fills the left atrium. When enough blood is inside the left atrium, pressure builds up and opens the mitral valve delivering blood to the left ventricle (LV). Once the pressure builds up in the LV, blood is circulated to the body. Functional evaluations of the heart are normally focused on the ability of the ventricles to pump blood to the lungs (i.e., RV) or to the entire body (i.e., LV). A problem in either of the ventricles will lead to heart failure. To provide accurate cardiac diagnosis and prognosis, ventricular specific parameters must be assessed.

Non-invasive imaging modalities allow physicians to quantitatively assess ventricular function, particularly for the LV. Two main factors propelled the use of LV analysis. First, common cardiac diseases such as congestive heart failure (CHF) related to coronary artery disease, or alcohol- or viral- induced cardiomyopathies<sup>1</sup> have a disproportionate effect on the LV [2]. Second, imaging modalities such as plane x-ray and echocardiography had trouble imaging the RV [3]. Improved imaging modalities, such as cardiac magnetic resonance (CMR), allowed the extraction of volumetric information for both the LV and the RV, thus making analysis of both

---

<sup>1</sup> Heart muscle disease. Inability of the myocardium to contract.

ventricles viable. The ability to analyze the RV has identified RV-specific pathologies, such as CHF, pulmonary hypertension and congenital heart disease [4]-[6]. Early and accurate detection of these pathologies can have a lasting health benefit for the patient.

Performing ventricular quantitative analysis requires tracing of the ventricle. Even though manual tracing is still considered the gold standard [7][8], it is prone to intra- and inter-observer variability and it is time consuming, taking a physician an average of 15 minutes per ventricle [9]. Therefore, substantial research work has been focused on the development of semi-automated and fully automated ventricular segmentation algorithms.

In 2009 at the Medical Image Computing and Computer-Assisted Intervention (MICCAI) conference, an LV segmentation challenge was issued [10]. The challenge consisted of outlining the LV in the end-diastolic (ED<sup>2</sup>) and end-systolic (ES<sup>3</sup>) frame in 45 patients. Fifteen patients were used for training, 15 for testing and 15 for validation. The results of the challenge showed that some algorithms were within human variability [11]. A similar challenge was issued for the RV segmentation at the 2012 MICCAI conference [9], but the results were not within human variability. For both MICCAI segmentation challenges, the owners of the data sets had to manually parse the data and identify the slices associated with different parts of the RV anatomy. This type of overhead will make implementation of most of those algorithms in a clinical setting challenging.

The purpose of this dissertation is to provide a semi-automated segmentation technique for the RV. Unlike most techniques that focus only on the short-axis (SAX) views, this dissertation

---

<sup>2</sup> ED frame denotes the frame where the ventricles (LV and RV) contain the most amount of blood.

<sup>3</sup> ES frame denotes the frame where the ventricles (LV and RV) contain the least amount of blood.

focuses mainly on the segmentation of the RV in four chamber (4CH) views with user-specified inputs. We focus on the 4CH because generally SAX images poorly represent some key anatomic elements of the RV (RV apex, conus, tricuspid annular plane) which are important for functional assessment. Standard 4CH views may represent most of the relevant RV landmarks (i.e., tricuspid valvular (TV) plane, apex, free wall) and do not require any change to the existing CMR protocols. We understand that volumetric analysis<sup>4</sup> is done using SAX views; in the last chapter of the dissertation, we explore the use of RV segmentation in 4CH views to automatically segment the RV in the SAX views. The rationale is that the initial delineation and identification of the relevant RV landmarks in the 4CH view could provide a concise framework for the automatic segmentation of the RV in the SAX views.

## 1.1 Cardiac Imaging Modalities

The invention of the x-ray started the field of non-invasive imaging. X-ray used in conjunction with cinematography allowed physicians to non-invasively image the heart, particularly the LV, throughout the cardiac cycle [12]. Due to the effects of ionizing radiation, physicians looked for an alternative technique for imaging the heart. In 1953, inspired in part by the success of radio detection and ranging (RADAR), Inge Edler and Hellmuth Hertz recorded the first ultrasound (US) generated moving pictures of the heart using M-mode echocardiography [13]. By the early 70s the first 2D echocardiography instrument was developed and brought to market [14]. Even though it had tremendous popularity, 2D echocardiography suffered from a series of drawbacks, particularly the inability to correctly image the RV. In the mid to late 90s, CMR emerged as a

---

<sup>4</sup> The current gold standard for ventricular functional analysis.

non-invasive modality capable of imaging the heart. With the use of electrocardiogram (ECG) pulse gated sequences, CMR has become the gold standard for ventricular function and is recognized by many as the “one-stop-shop” for cardiovascular imaging [15].

### 1.1.1 Echocardiography

Echocardiography is based on US imaging and consists of sending high frequency (MHz) pulse waves to the body and measuring their reflection. The reflection of the pulse wave is characterized by:

$$v = \lambda f \quad (1.1)$$

where  $v$  is the velocity,  $f$  is the frequency and  $\lambda$  is the wavelength. The velocity of the pulse wave is determined by the medium where it is being sent. Some common media are shown in Table 1.1.

Table 1.1 Velocity of sound through different mediums.

Medium	Fat	Water	Soft Tissue	Kidney	Blood	Muscle	Bone	Air
Velocity (m/sec)	1450	1480	1540	1560	1570	1580	4080	331

Pulse waves traveling through a medium can experience other interactions besides reflection, including attenuation, absorption, scattering, refraction and diffraction. The reflection of the beam occurs at the boundary between two different materials. When pulse waves pass through areas containing bone or air they can produce large echoes, thus reducing the ability to image further. Since the RV sits behind the sternum, echocardiography performs poorly when trying to image the RV.

### 1.1.2 Magnetic Resonance Imaging

Clinical magnetic resonance imaging (MRI) is an imaging modality that detects the *spin* or intrinsic angular moments of the hydrogen ( $^1\text{H}$ ) atoms or protons in the body. In the absence of an external magnetic field ( $\vec{B}_0$ ) the spins are randomly oriented resulting in no net magnetization ( $\vec{M}_0$ ) (Figure 1.1a). In the presence of an external magnetic field (e.g., 1.5T), the spins align with  $\vec{B}_0$  (Figure 1.1b) generating  $\vec{M}_0$  in the direction of  $\vec{B}_0$  (Figure 1.1c).  $\vec{M}_0$  precesses at a frequency defined by the Larmor equation:

$$f = \frac{\gamma B_0}{2\pi} \quad (1.2)$$

where  $f$  is the precession frequency and  $\gamma$  is the *gyromagnetic ratio*<sup>5</sup>. For  $^1\text{H}$ :

$$\frac{\gamma}{2\pi} = 42.58 \times 10^6 \frac{\text{Hz}}{\text{Tesla}} \quad (1.3)$$

---

<sup>5</sup> Ratio of the magnetic dipole moment to its angular momentum.

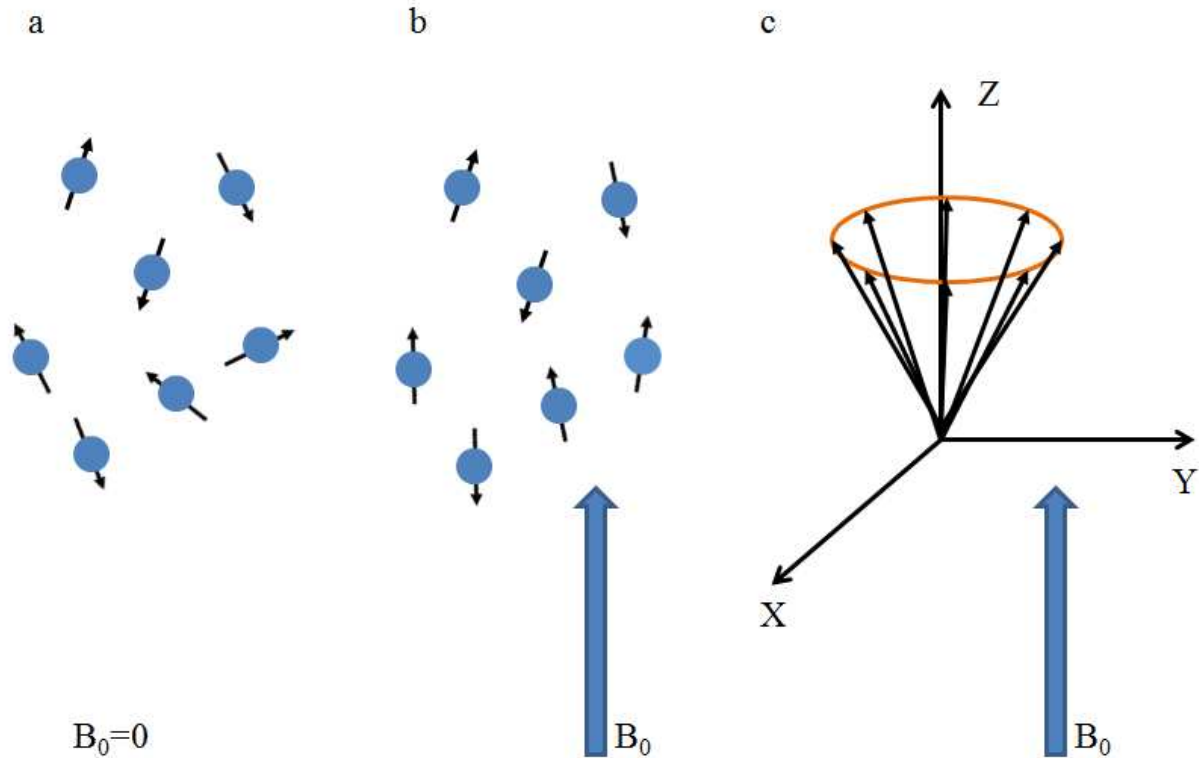


Figure 1.1 Effect of an external magnetic field ( $B_0$ ) on the spins. (a) When no external magnetic field is applied the spins are randomly oriented. (b) In the presence of an external magnetic field, the spins align with the field. (c) Net magnetization of the spins is now along the direction of  $B_0$ . Note that there is no net magnetization in the X-Y plane.

To detect the MR signal, a radiofrequency (RF) excitation pulse is necessary. RF excitation consists of applying an external magnetic field  $\vec{B}_1$  with frequency  $f$  perpendicular to  $\vec{B}_0$  (i.e., in the X-Y plane). The strength of the RF pulse determines whether the spins are flipped partially or entirely into the X-Y plane. When the flip angle ( $\alpha$ ) of the RF pulse is  $90^\circ$ , the magnitude of the magnetization in the X-Y plane ( $M_{xy}$ ) right after excitation equals  $M_0$ . Once the RF pulse is turned off, the signal in the X-Y plane can be detected with a receiver coil.  $\vec{M}_{XY}$ , and thus the magnitude of the signal in the X-Y plane ( $|s(t)|$ ), will decay via  $T_2^*$  (shown in Figure 1.2), which

is due to the combined spin-spin ( $T_2$ ) relaxation<sup>6</sup> and the dephasing due to static magnetic fields ( $T_2^\dagger$ ).

$$|s(t)| = M_0 \sin(\alpha) e^{-\frac{t}{T_2^*}} \quad (1.4)$$

where

$$\frac{1}{T_2^*} = \frac{1}{T_2} + \frac{1}{T_2^\dagger} \quad (1.5)$$

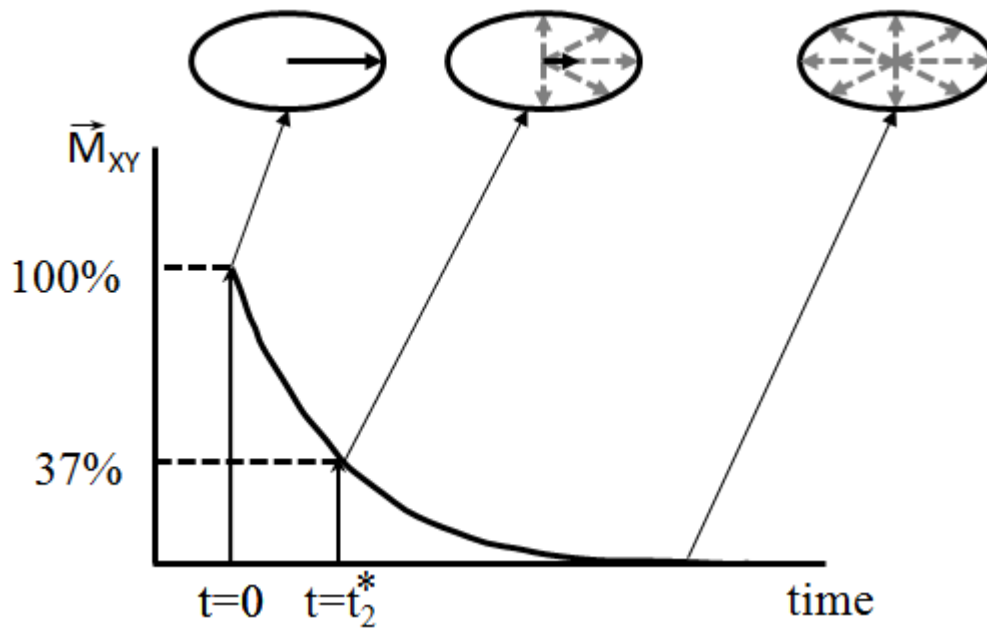


Figure 1.2 Signal dephasing in the X-Y plane due to  $T_2^*$  relaxation mechanism.

$\vec{M}_{XY}$  will also recover to its equilibrium state along  $\vec{B}_0$  (typically represented along the z-axis) due to  $T_1$ , or spin-lattice relaxation mechanism. Thus, the recovery of the magnetization along z can be expressed as:

$$M_z(t) = M_0 \left( 1 - (1 - \cos(\alpha)) e^{-\frac{t}{T_1}} \right) \quad (1.6)$$

<sup>6</sup> Spins experiencing the effect of fluctuating magnetic fields created by other spins.

Table 1.2  $T_1$  and  $T_2$  values for heart tissue components at 1.5T.

	$T_1$ (ms)	$T_2$ (ms)
Myocardium	1100	50
Arterial blood	1600	250
Fat	260	110
Skeletal muscle	880	45
Lung	820	140

To obtain an image we use magnetic field gradients to change  $B_0$  linearly with position

$$B(x, y, z) = B_0 + xG_x + yG_y + zG_z \quad (1.7)$$

which in turn changes the precession frequency of the spins:

$$f(x, y, z) = \frac{\gamma}{2\pi} B(x, y, z) \quad (1.8)$$

In 2D MRI, which is the focus of this dissertation, the first step is to select the slice to be imaged (for nomenclature purposes the slice selection plane is defined to be along the  $z$  axis). This is done by turning on the  $G_z$  gradient in order to vary  $f$  across the  $z$  axis:

$$f(z) = \frac{\gamma}{2\pi} (B_0 + zG_z) \quad (1.9)$$

By using a band-limited RF pulse while  $G_z$  is on, only the spins within the selected range of frequencies corresponding to a specific slice thickness are excited into the X-Y plane, as shown in Figure 1.3.

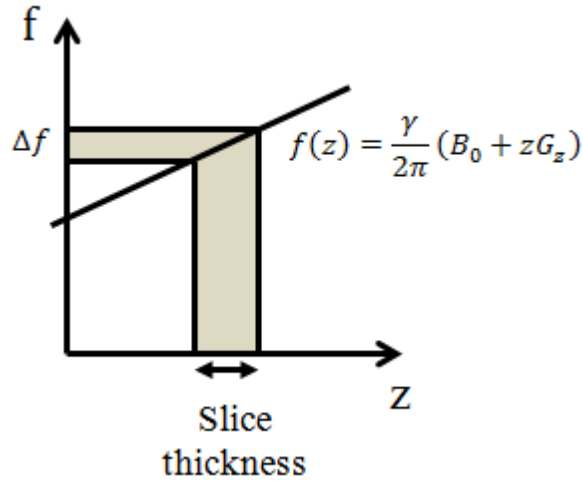


Figure 1.3 Slice selection process.

Once the slice is selected the signal detected by the receiver coil can be written as:

$$s(t) = A \int \int M_{XY}(x, y) e^{-it2\pi f} dx dy \quad (1.10)$$

where  $A$  is a constant. Note that there is no specificity for  $(x, y)$  so we need to use frequency encoding ( $G_x$ ) and phase encoding ( $G_y$ ) magnetic field gradients to encode spatial information within the slice. When  $G_x$  and  $G_y$  are turned on, the Larmor frequency becomes:

$$f(x, y) = \frac{\gamma(B_0 + xG_x + yG_y)}{2\pi} \quad (1.11)$$

Therefore, the signal detected by the receiving coil is:

$$s(t) = A e^{-i\gamma B_0 t} \int \int M_{XY}(x, y) e^{-i\gamma t(xG_x + yG_y)} dx dy \quad (1.12)$$

The baseline signal can be obtained by demodulating (1.12) from the carrier frequency. The resulting signal is shown in (1.13):

$$s'(t) = s(t) e^{i\gamma B_0 t} = A \int \int M_{XY}(x, y) e^{-i\gamma t(xG_x + yG_y)} dx dy \quad (1.13)$$

Defining  $k_x(t) = \frac{\gamma t G_x}{2\pi}$  and  $k_y(t) = \frac{\gamma t G_y}{2\pi}$ , we can rewrite (1.13) as

$$s'(t) = A \int \int M_{XY}(x, y) e^{-i2\pi(xk_x + yk_y)} dx dy \quad (1.14)$$

Equation (1.14) shows that the data acquired by the receiver coil is the Fourier transform (FT) of the object and  $k_x$  and  $k_y$  gives us the frequency localization in *k-space* (Figure 1.4). Therefore, once *k-space* is sampled, we can recover the image by doing a 2D inverse FT (2D IFT). This creates an MR image.

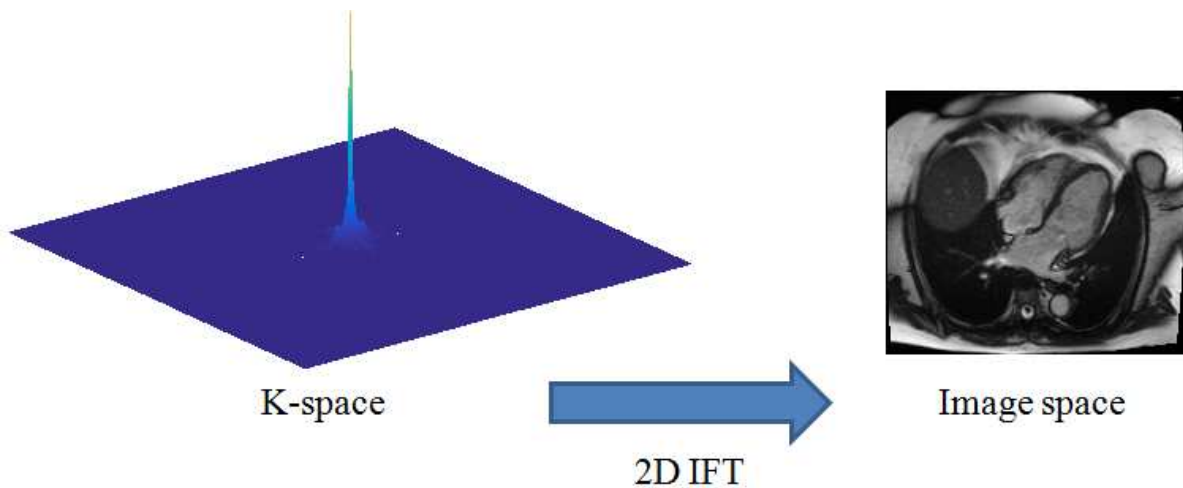


Figure 1.4 Creation of an MR image.

To sample the *k-space* pulse sequences are used. A pulse sequence is a programmed set of magnetic field gradients waveforms. One of the most common pulse sequences used for cardiac imaging is the balanced steady state free precession (SSFP) pulse sequence (Figure 1.5).

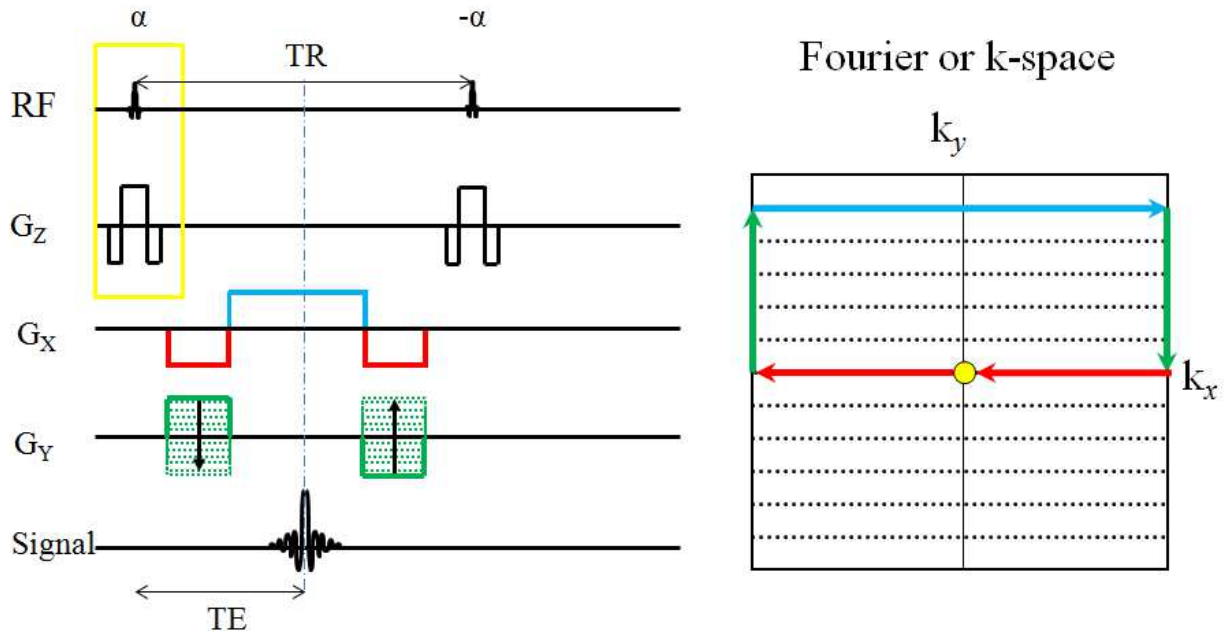


Figure 1.5 Balanced steady state free precession (SSFP) pulse sequence illustrating the slice selection module (yellow) and the gradient waveforms used to traverse k-space.

The 2D SSFP pulse sequence follows the same series of steps as most MRI pulse sequences. First, spins are excited within the imaging slice by using a band limited RF pulse while the  $G_z$  gradient is on (yellow module in Figure 1.5); at this point we are at the k-space origin (yellow circle). Next, the prepositioning  $G_x$  and  $G_y$  gradients (red and green left waveforms in Figure 1.5) are turned on to move to the upper left corner of k-space. Then, the  $G_y$  gradient is turned off and  $G_x$  changes polarity to acquire a  $k_y$  line of data (blue line in Figure 1.5). Once a  $k_y$  line has been read, data acquisition is turned off. To return to the k-space origin, the polarity of  $G_y$  and  $G_x$  is reversed as indicated by the red and green right waveforms in Figure 1.5. The experiment continues by re-exciting the spins in the slice and changing  $G_y$  to sample the complete k-space

(i.e., 160-256 k-space lines with 160-256 points along each line). Some common parameters for the pulse sequences are the time to repetition (TR<sup>7</sup>) and the time to echo (TE<sup>8</sup>).

Analyzing the functional properties of the heart requires imaging of the heart throughout the cardiac cycle. There are two problems when imaging the heart related to physiological motion: first is the chest motion due to respiration and second is the beating of the heart. To solve the first problem, cardiac imaging is typically done during a breath hold that lasts between 10-16 seconds. To image the heart throughout the cardiac cycle a technique called cardiac gating is used (Figure 1.6). Given the QRS complex<sup>9</sup>, which is measured using ECG leads, the technique identifies two nearby R peaks. Then, it divides the time between the R peaks into a set of equally spaced time frames of approximately 30-50 ms/frame. On each time frame, only a subset of the total k-space lines is read depending on the temporal resolution and TR (~3ms). The heart rate may range from 60 to 100 beats per minute (bpm). If we assume a heart rate of 75 bpm, and we want to reconstruct images for 25 time frames, the number of k-space lines collected for each time frame within a single heartbeat is

$$\text{round}\left(\frac{1 \text{ minute}}{75 \text{ bpm}} \cdot \frac{60 \text{ sec}}{1 \text{ minute}} \cdot \frac{1 \text{ b}}{25 \text{ frame}} \cdot \frac{1 \text{ line}}{3 \times 10^{-3} \text{ sec}}\right) = 11 \frac{\text{lines}}{\text{frame}} \quad (1.15)$$

which in this case will give us a temporal resolution of 33 ms/frame. Note that in order to sample the k-space with adequate spatial resolution (e.g., 168 k-space lines) we need 16 heartbeats which is approximately 12 seconds of scan time. Current clinical and research

---

<sup>7</sup> Measures the time between RF pulses.

<sup>8</sup> Time between an RF pulse and the midpoint of signal detection.

<sup>9</sup> Electrical signal caused by the depolarization of the RV and LV.

guidelines consider cine CMR using the balanced SSFP pulse sequence the gold standard for evaluation of the left and right ventricular function [16].

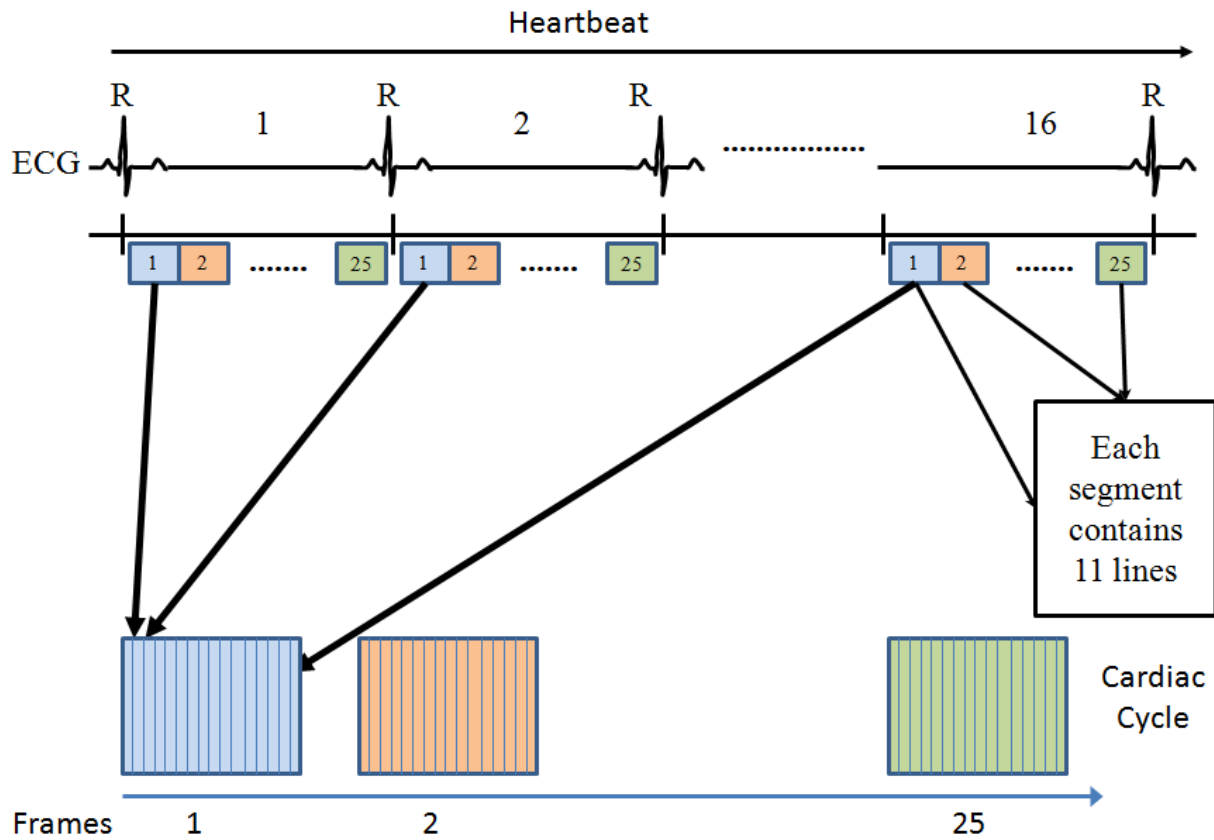


Figure 1.6 Cardiac gating procedure used for cine MRI.

## 1.2 RV Cardiac Pathologies

### 1.2.1 Pulmonary Hypertension

The Evian classification protocol outlines multiple reasons for pulmonary hypertension. Among them are: pulmonary arterial hypertension, pulmonary hypertension with left heart disease, pulmonary hypertension associated with lung diseases and/or hypoxemia<sup>10</sup> and pulmonary hypertension due to chronic thrombotic and/or embolic disease [17]. An initial response to pulmonary hypertension is the hypertrophy of the myocardium, followed by contractile dysfunction<sup>11</sup>. As contractile weakening progresses, the residual blood in the RV increases requiring an increase in RV pressure (i.e., increases the pressure necessary for the RV to send blood to the lungs), which may in turn produce diastolic dysfunction of the LV [18]. In patients with end-stage pulmonary hypertension, the shape of the RV becomes abnormal [19].

One of the first treatments for pulmonary hypertension is giving the patient oxygen. Other treatments include medications that may: 1) help decrease blood pressure, 2) assist the pumping of the heart, 3) remove excess fluids, 4) reduce clotting, 5) prevent blood vessels from narrowing and 6) allow lungs to produce natural vasodilators [20]. Definitive therapy for end-stage pulmonary hypertension is lung transplantation that has been shown in some cases to reduce the dilation of the RV [21][22].

---

<sup>10</sup> An abnormally low concentration of oxygen in the blood.

<sup>11</sup> Inability to fully contract the myocardium muscle. This is usually caused by a lack of oxygen in the myocardium.

### 1.2.2 Congestive Heart Failure

CHF is a condition that reduces the ability of the ventricles to pump blood to the body. CHF in the LV results in the reduced capability to pump blood to the organs in the body, whereas in the RV it reduces the ability to pump blood to the lungs resulting in a decrease of oxygenated blood. This lack of circulation causes leakage and fluid retention. Symptoms of this disease are shortness of breath and lower extremity fluid retention related to pulmonic and systemic edema<sup>12</sup>, respectively.

CHF cannot be cured, yet the symptoms can be treated. Primary treatment options include reducing the amount of salt in the diet, elimination of alcohol intake, monitor weight, exercise, and taking medications (similar to pulmonary hypertension).

### 1.2.3 Congenital Heart Disease

Congenital heart disease (CHD) relates to an abnormality in a newborn's cardiac structure. Symptoms of this disease include arrhythmias<sup>13</sup>, cyanosis<sup>14</sup>, and edema among others. If left untreated CHD can give rise to cardiac pathologies such as arrhythmias, strokes, CHF, and pulmonary hypertension among others [23].

Main treatment options include taking medications (similar to pulmonary hypertension), implantation of heart devices, open-heart surgery, and heart transplant.

---

<sup>12</sup> Swelling of body tissue or organs

<sup>13</sup> Abnormal heart rhythms

<sup>14</sup> Bluish skin color

### 1.3 Ventricular Cardiac Function

The assessment of ventricular cardiac function is key to diagnosing LV and RV pathologies. The best way to assess the ventricular cardiac function is to utilize a 3D approach, with a development of the Beutel model [24][25][26]. However, the vast majority of CMR exams are currently done using a 2D approach because Simpson's rule can be used to find volumetric information from a series of 2D MR images. Simpson's rule is an integration approximation that uses parabolas to approximate a curve [27].

$$\int_a^b f(x)dx = \frac{b-a}{3n} [f(x_0) + 4f(x_1) + 2f(x_2) + \dots + 2f(x_{n-2}) + 4f(x_{n-1}) + f(x_n)] \quad (1.16)$$

where  $[b, a]$  are the integration interval,  $n$  is an even number of subintervals and  $[x_0 \dots x_n]$  are  $n$  equally-spaced values between  $a$  and  $b$ . Simpson's rule can be extended to approximate volumetric values from a series of 2D images by changing  $f(x)$  from a 1D function to a 2D function (e.g., ventricle outline).

#### 1.3.1 Imaging Planes

In Section 1.1.2 we described how to generate a 2D MR image where slice selection was done axially<sup>15</sup>. Other common slice selection axes such as coronal<sup>16</sup> and sagittal<sup>17</sup> are shown in Figure 1.7. Due to the orientation of the heart within the body, oblique planes are generally used for slice selection. The oblique planes used for RV functional assessment are shown in Figure 1.8 .

---

<sup>15</sup> Plane that divides the head from the toes

<sup>16</sup> Plane that divides the body into back and front

<sup>17</sup> Plane that divides the body into left and right

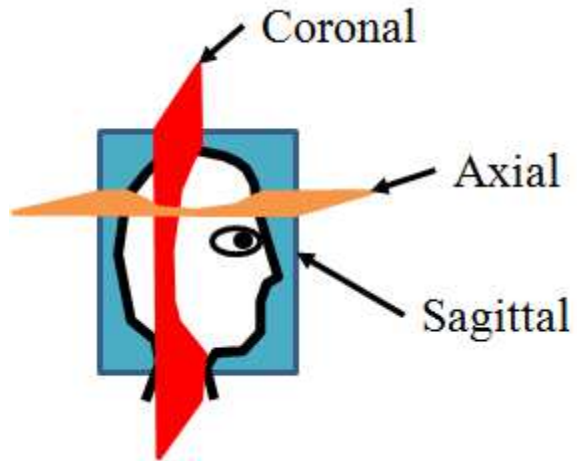


Figure 1.7 Common MR imaging angles.

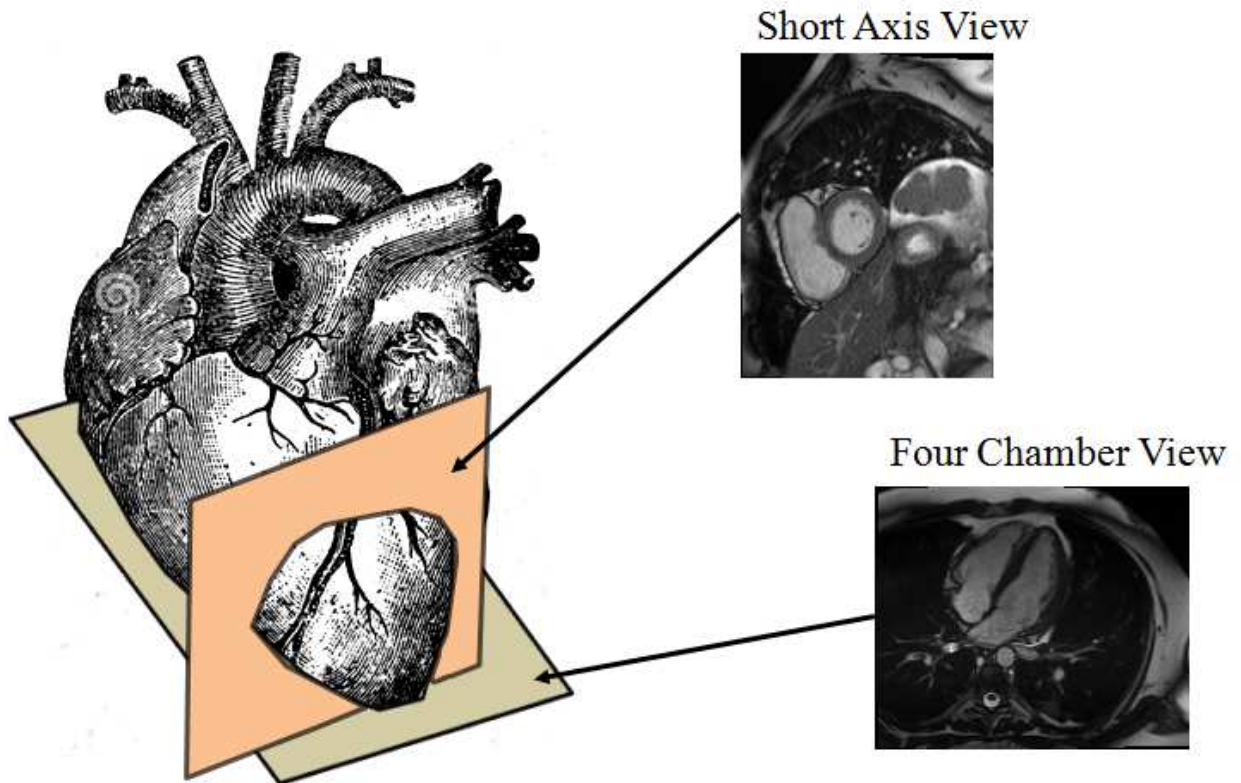


Figure 1.8 Viewing angles used for functional RV assessment.

### *1.3.1.1 SAX View*

SAX views are considered the gold standard [28][29] for ventricular function assessment. This is due to the fact that the volumetric measurements derived from these views correlate well with anatomical features. SAX views show cross-sections that are perpendicular to 4CH views. Features that are commonly calculated from the SAX views include end-diastolic volume (EDV), end-systolic volume (ESV), ejection fraction (EF), and stroke volume (SV), among others.

### *1.3.1.2 4CH View*

Even though SAX views are the gold standard due to their volumetric information, SAX images poorly represent some key anatomic elements of the RV (RV apex, conus, tricuspid annular plane) that are important for functional assessment. In this regard, standard 4CH views may represent most of the relevant RV landmarks (i.e., tricuspid valvular plane, apex, free wall) and do not require any change to the existing CMR protocols. There is also the fact that longitudinal shortening is a greater contributor to RV stroke volume than SAX shortening [30]. Features that are commonly calculated from the 4CH views include tricuspid annular plane systolic excursion (TAPSE) and fractional area change (FAC).

## 1.3.2 Stroke Volume

SV is the volume of blood pumped by a given ventricle. It is calculated by:

$$SV = EDV - ESV \quad (1.17)$$

where EDV is the volume of the ventricle in the ED frame and ESV is the volume of the ventricle in the ES frame.

### 1.3.3 Ejection Fraction

EF is defined as SV divided by EDV:

$$EF = SV/EDV \quad (1.18)$$

### 1.3.4 Tricuspid Annular Plane Systolic Excursion

TAPSE is a cardiac functional metric that measures the apex-to-base shortening. TAPSE is commonly used in echocardiography to analyze ventricular function, although it has a weak correlation with EF (i.e., R=0.16) [31][32].

### 1.3.5 Fractional Area Change

FAC is defined as follows:

$$FAC = \frac{EDA - ESA}{EDA} \quad (1.19)$$

where  $EDA$  and  $ESA$  are the area of the RV in the ED and ES frames, respectively. FAC is commonly used in echocardiography to analyze ventricular function [33] and it has a correlation with EF fraction around 0.68 [32].

## 2 DIGITAL IMAGE PROCESSING TECHNIQUES

Digital image processing (DIP) is the process of applying mathematical operators to process a digital image with a digital computer [34]<sup>18</sup>. The smallest element in a digital image is referred to as a pixel. DIP is a well-studied area of research that spans many subjects, but for the purpose of this dissertation we will talk about graph theory and segmentation. The latter part of the chapter will focus on segmentation techniques that have been applied to segment the LV and RV.

### 2.1 Graph Theory

Graph theory is the study of graphs, which are mathematical structures that measure relationship between vertices. These vertices are connected to one another through lines or edges. A graph is usually described as:

$$G = (V, E) \quad (2.1)$$

where  $G$  is a graph,  $V$  are a set of vertices and  $E$  are a set of edges that connect the vertices. In DIP, graph theory can be used to represent pixels in the image where  $V$  is a pixel, and  $E$  is the relationship between nearby pixels. An example is shown in Figure 2.1.

---

<sup>18</sup>DIP, digital image analysis and computer vision are usually used interchangeably as there is no consensus between authors. In our dissertation we will use DIP to encompass the three concepts.

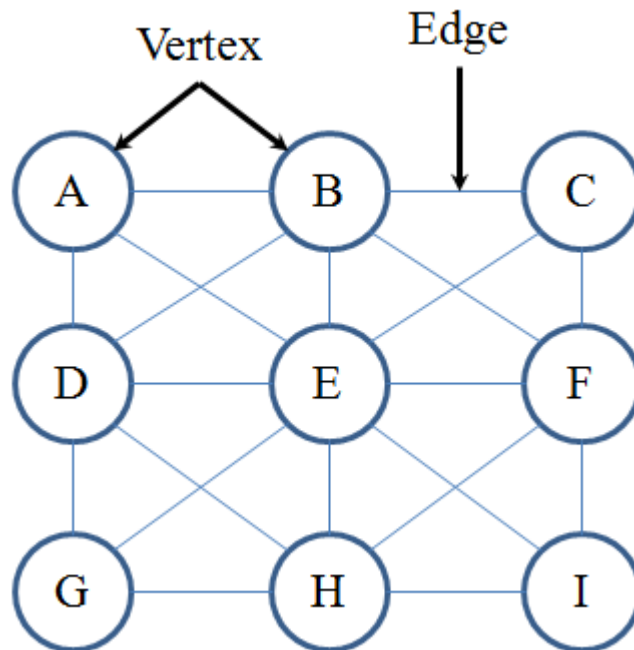


Figure 2.1 3x3 neighborhood represented using vertices and edges.

The example in Figure 2.1 will yield a graph with vertices:

$$V = \{A, B, C, D, E, F, G, H, I\} \quad (2.2)$$

and edges:

$$E = \left\{ \begin{array}{l} (A, B), (A, E), (A, D), (B, E), (B, D), (B, F), \\ (B, C), (C, E), (C, F), (D, E), (D, G), (D, H), \\ (E, F), (E, G), (E, H), (E, I), (F, H), (F, I), (G, H), (H, I) \end{array} \right\} \quad (2.3)$$

A path in  $G = (V, E)$  is a finite sequence that alternates vertices and edges passing through them just once [35][36]. The minimum cost path techniques described below (i.e., Sections 2.1.1-2.1.3), are paths that minimize cost or distance traveled from the initial vertex to the final vertex.

### 2.1.1 Dijkstra's Shortest Path Algorithm

In 1956, Edsger W. Dijkstra developed an algorithm for finding the shortest path between two vertices in a graph, given that the edges (e.g., distance) are non-negative [37]. The algorithm is as follows:

- 1) Set the distance in the source vertex to 0. The source vertex is initialized to be the current vertex. Close the source vertex.
- 2) Set all the other distances to  $\infty$ . All the other vertices are open.
- 3) For the current vertices<sup>19</sup> consider all the adjacent open vertices and calculate the distance from the origin to the adjacent open vertex<sup>20</sup>. If the new distance in the adjacent open vertex is smaller than the previous distance, replace the distance with the new value.
- 4) When all the adjacent vertices for the current vertex have been evaluated, flag the current vertex as closed. Closed vertices will not be analyzed again.
- 5) Set the adjacent open vertex with the lowest distance to the current vertex and continue from step 3. This is repeated until the current vertex is the final vertex or all the vertices are closed.

### 2.1.2 A\* Algorithm

In 1968, Peter Hart, Nils Nilsson and Bertram Raphael described the A\* algorithm [38]. It consisted of adding a heuristic to the cost function used by Dijkstra in order to speed up the

---

<sup>19</sup> There may be more than one.

<sup>20</sup> This is calculated by adding the edge between the current vertex and the adjacent vertex.

search by reducing the number of vertices that needed to be analyzed. The new cost function is defined as:

$$f(n) = h(n) + g(n) \quad (2.4)$$

where  $n$  is the last vertex on the path,  $g(n)$  is the total cost path from the starting vertex to  $n$  and  $h(n)$  is a heuristic that estimates the cost from vertex  $n$  to the final vertex. Note that Dijkstra's shortest path algorithm is a specific formulation of the A\* algorithm ( $h(n) = 0$ ).

The A\* algorithm is then defined as follows:

- 1) Select a vertex (i.e., initial vertex), set it as the current vertex and calculate  $f(n)$ . All other vertices are open.
- 2) Select the open adjacent vertex that yields the smallest  $f(n)$  and name it new vertex. Ties are resolved arbitrarily, unless one of the ties is the ending vertex, which in that case make the ending vertex the new vertex.
- 3) If the new vertex is the ending vertex terminate the algorithm.
- 4) Otherwise mark the current vertex as closed and set the current vertex to be the new vertex. Go to step 2.

Let's define  $g(n) = \sum_{i=1}^n c_i$ , which means that there is a cost associated with going from the initial vertex to any given vertex. If we go from  $n + 1$  until the ending vertex, we can set the equation to:  $g(K) = \sum_{i=n+1}^K c_i$ . What [38] says is that as long as  $h(n) \leq g(K)$  then the A\* algorithm is admissible (i.e., yields a minimum cost path while "opening" fewer vertices).

### 2.1.3 Dynamic Programming

Dynamic programming is an optimization method that solves a complex problem by applying the principle of optimality<sup>21</sup> [39]. Unlike greedy algorithms which select the best locally optimal solutions, dynamic programming solves smaller sub-problems and combines them to yield the optimum solution [40]. An example of this is shown in Figure 2.2.

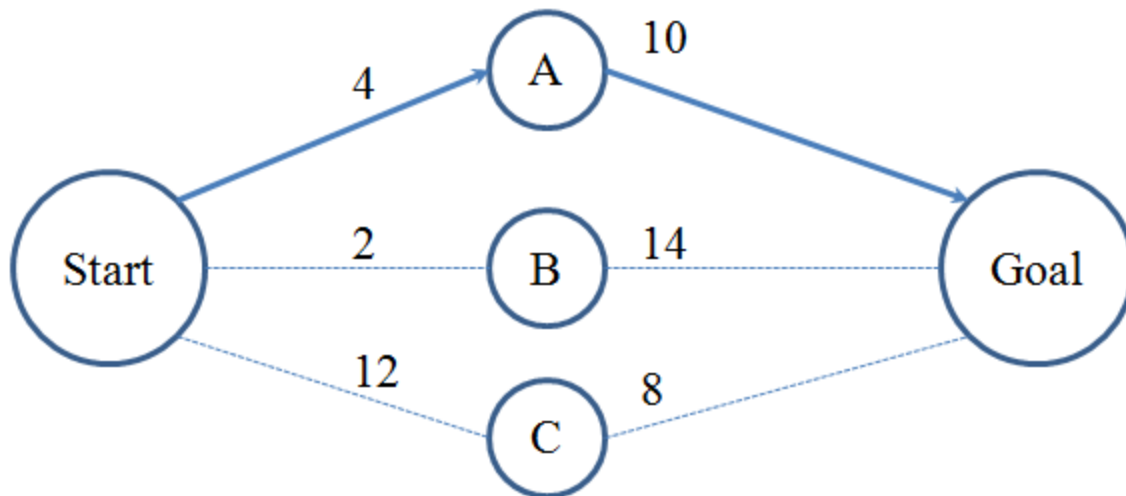


Figure 2.2 Finding the shortest path using dynamic programming.

Note that a greedy algorithm starting from the start node, may select the path that goes through vertex B, while a greedy algorithm that backtracks may select the path that goes through vertex C. To use dynamic programming for DIP, the algorithm divides in two parts, first forward propagation<sup>22</sup>:

- 1) Mark all the starting vertices (i.e., there may be more than one) as closed. The other vertices are marked as open.
- 2) Look at open vertices that are adjacent to the closed vertices.

<sup>21</sup> The idea that complex problems can be divided into simpler sub problems.

<sup>22</sup> Assigns cost to each vertex.

- 3) For each open vertex, select the adjacent closed vertex that has the lowest cost.
- 4) Combine the cost of the adjacent closed vertex with the smallest cost to the cost of the analyzed open vertex.
- 5) Proceed to the next open vertex.
- 6) Repeat 3-5 until no more open vertices are adjacent to closed vertices.
- 7) Close all the open vertices that are adjacent to the closed vertices.
- 8) Repeat 2-4 until no open vertices are left.

Second algorithm is back propagation<sup>23</sup>:

- 1) Mark the ending vertex with the lowest cost as closed. In case of a tie, resolve arbitrarily. The other vertices are marked as open.
- 2) Select the open vertex with the lowest cost that is adjacent to the closed vertex. The cost is the result of forward propagation algorithm. In case of a tie, resolve arbitrarily.
- 3) Close the vertex selected from step 2.
- 4) Repeat 2-3 until the closed vertex is a starting vertex.

The dynamic programming algorithms assume that all the cost values are positive. A mathematical implementation of the algorithm is described in Chapter 3.1.3.

## 2.2 Segmentation

Image Segmentation is the process of partitioning a digital image ( $I(x, y)$ ) into non-overlapping homogenous regions (or segments) [34]. The regions may have additional properties such as

---

<sup>23</sup> Finds the minimum cost path by backtracing from the end vertex

smoothness of the region border or high gradient on the region borders, among others. The final goal of segmentation is to simplify the analysis of a digital image. There are multiple ways to segment a digital image, but for this dissertation we shall focus on three methods of segmentation: active contours, level sets, and PDP.

### 2.2.1 Active Contour Methods

In 1987, Michael Kass, Andrew Witkin and Demetri Terzopoulos developed an energy-minimizing spline that uses image forces and external constraint forces (e.g., high gradients) to arrive to a minimum energy state [42]. The authors termed this technique “snakes”. The initial curve or snake can be parameterized as  $v(s) = \{x(s), y(s)\}$ , where  $s \in [0,1]$ . A snake where  $v(0) = v(1)$  is deemed closed (i.e., closed contour), whereas a snake where  $v(0) \neq v(1)$  is deemed open (i.e., open contour). For our purposes we will focus on closed contours. An example of a closed contour is shown in Figure 2.3.

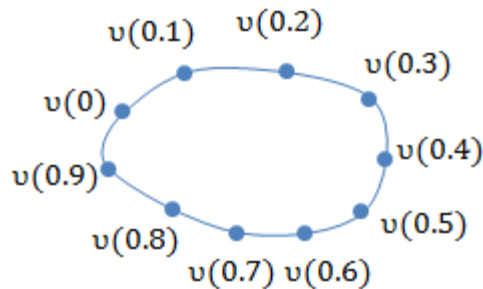


Figure 2.3 Parametric representation of a closed contour,  $v(0) = v(1)$ .

The parametric equation is as follows:

$$E_{snake}^* = \int_0^1 E_{snake}(v(s)) ds = \int_0^1 (E_{int}(v(s)) + E_{image}(v(s)) + E_{con}(v(s))) ds \quad (2.5)$$

where  $E_{int}$  is the internal energy of the spline,  $E_{image}$  is the energy of the image forces and  $E_{con}$  are external constraint forces (i.e., user interaction). The end-goal of the algorithm is to minimize (2.5). For simplicity most techniques assume that  $E_{con} = 0$ . The internal force of the closed contour  $E_{int}$  looks at the curvature and stiffness of the closed contour, thus yielding:

$$E_{int}(v(s)) = \frac{(\alpha(s)|v'(s)|^2 + \beta(s)|v''(s)|^2)}{2} \quad (2.6)$$

For simplicity most active contour techniques set  $\alpha(s) = \alpha$ ,  $\beta(s) = \beta$ . Having  $E_{int} = 0$  implies making the final closed contour a dot. Regularly  $E_{image}$  is based on the gradient of the image:

$$E_{image}(v(s)) = -|\nabla(G_\sigma(x,y) * I(x,y))|^2 \quad (2.7)$$

Here,  $G_\sigma(x,y)$  is a 2D Gaussian function with standard deviation  $\sigma$ ,  $*$  denotes linear convolution, and  $\nabla$  is the gradient operator. Minimizing  $E_{image}$  makes the closed contour move toward high gradients. The snake that yields the lowest energy must satisfy the equation:

$$\alpha v''(s) - \beta v'''(s) - \nabla E_{image}(v(s)) = 0 \quad (2.8)$$

Visually, the proper balance between  $E_{int}$  and  $E_{image}$  produces a smooth closed contour with high gradients on the region border.

The main drawbacks of the technique are: the reliance on a good initialization<sup>24</sup> and the inability to outline concavities [43][44]. To address these problems, Xu and Prince [45] introduced the gradient vector flow (GVF). GVF diffuses  $E_{image}(v(s))$ , as defined by (2.7), to generate a new  $E_{image}(v(s))$  and proceeds to find the optimum closed contour by balancing  $E_{image}$  and  $E_{int}$

---

<sup>24</sup> A good initialization is a initial mask that is near the final high gradient regions of the closed contour.

(i.e., (2.8)). The diffusion of  $E_{image}$  allows closed contours to move toward high gradient regions even when the initial closed contour is far from the optimum closed contour.

The main drawback of GVF is the susceptibility to noise. To address this problem, Bing Li and Scott T. Acton developed a new static image force robust to noise which they termed vector field convolution (VFC) [46]. The idea behind VFC is to create a vector field kernel (VFK) where all the vectors point to the origin and convolve this VFK with an edge map similar to the one shown in (2.7). By finding the density of high gradient regions, this technique is more robust to noisy edge maps. An example of a VFK of radii 4 is shown in Figure 2.4. In their work Li and Acton show how their technique outperforms GVF in noisy images.

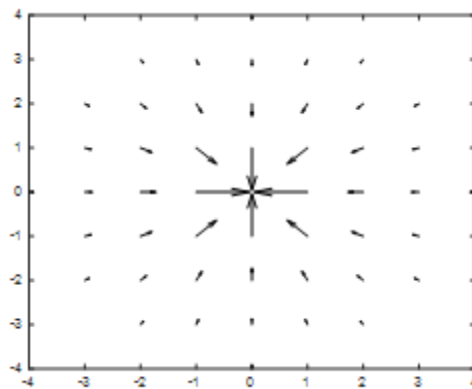


Figure 2.4 VFK with radii 4.

### 2.2.2 Level Sets Method

Level set method is a framework that captures dynamic shapes. It was introduced by Osher and Sethian in 1987 [47]. An application for image segmentation was introduced by Caselles *et al.* [48] and Malladi *et al.* [49]. The contour propagation used by [45] and [42] is based on the gradient descent equation:

$$\frac{\partial v(s,t)}{\partial t} = \left( E_{int}(v(s,t)) + E_{image}(v(s,t)) \right) \quad (2.9)$$

where  $v(s,0)$  is the initial closed contour. By changing the representation from the closed contour (i.e.,  $v(s,t)$ ) to a fixed Cartesian grid (i.e.,  $\phi(x,y,t)$ ) the contour propagation can be described as:

$$\frac{\partial \phi}{\partial t} = \text{div} \left( \frac{\nabla \phi}{|\nabla \phi|} \right) \nabla \phi \quad (2.10)$$

where  $\nabla$  is a gradient operator [42], and  $\text{div} \left( \frac{\nabla \phi}{|\nabla \phi|} \right)$  measures the curvature of  $\phi$  passing through  $(x,y)$ .



Figure 2.5 Change in parameterization for curve evolution used by Chan-Vese.

A desirable advantage of the level set methodology is their ability to handle complex topological changes such as splitting and merging.

To make use of these properties, Chan-Vese (CV) [50] developed a new active contour segmentation technique using level-sets. To do this, the authors defined  $E_{image}$  as follows:

$$E_{image}(\phi) = \lambda_1 \iint |I(x,y) - \bar{I}_1(x,y)|^2 H(-\phi(x,y)) dx dy \quad (2.11)$$

$$+ \lambda_2 \iint |I(x,y) - \bar{I}_2(x,y)|^2 H(\phi(x,y)) dx dy$$

where

$$\bar{I}_1(x, y) = \iint I(x, y)H(-\phi(x, y))dxdy \quad (2.12)$$

and

$$\bar{I}_2(x, y) = \iint I(x, y)H(\phi(x, y))dxdy \quad (2.13)$$

$H(x)$  is the Heaviside function [51], both  $\lambda_1, \lambda_2$  are bigger than zero, for most numerical calculations  $\lambda_1 = \lambda_2 = 1$ . To account for the fact that the change to a fixed Cartesian grid does not implicitly minimize the curvature of  $\phi$ , CV make an approximation of the internal energy as follows:

$$E_{int}(\phi) = \mu \iint \delta(\phi(x, y)) |\nabla\phi(x, y)|dxdy + v \iint H(-\phi(x, y)) dxdy \quad (2.14)$$

In the numerical implementation of the algorithm  $v = 0$ . This technique allows the segmentation of low gradient regions and multiple objects by using the properties of the level-set function.

The technique proposed by CV models  $I(x, y)$  as an image with constant illumination region and thus they perform two-class segmentation. In cases where the illumination is not constant, such as medical images, the technique fails. Mukherjee and Acton generalize (2.11) to model non-linear illumination in an image using Legendre basis functions. They termed this technique Legendre Level Set or L2S [52].

The main drawback of level set methods is the numerical stability. The method becomes unstable when the signed distance property of  $\phi$  is lost. CV reinitializes the level set to make sure it does not become numerically unstable. Unfortunately due to the complexity of the algorithm it is done in an *ad hoc* manner [51]. To make the level set evolution numerically stable, Li *et al.* [54] introduced a distance regularization step (DRLSE), defined as:

$$E_{int}(\phi) = \mu R_p(\phi) \quad (2.15)$$

where  $\mu$  is a constant, and  $R_p$  is the level set regularization term defined as:

$$R_p(\phi) \triangleq \iint p(\nabla\phi) \, dx dy \quad (2.16)$$

where  $p(s)$  is the potential used for distance regularization. In their work, they propose using:

$$p(s) = \begin{cases} \frac{1}{(2\pi)^2} (1 - \cos(2\pi s)), & \text{if } s \leq 1 \\ \frac{1}{2} (s - 1)^2, & \text{if } s \geq 1 \end{cases} \quad (2.17)$$

This potential allows the use of level set without the need of reinitialization.

### 2.2.3 Polar Dynamic Programming

In section 2.2.1 we discussed image segmentation using active contour models. Although the techniques incorporate a smoothness constraint on the shape of the closed contour, it can have any shape. If the object we want to segment is circular techniques such as circular Hough transform (CHT) could be used [55], although with a high cost in storage and processing. Sheila Timp and Nico Karssemeijer [70] developed a segmentation technique that uses dynamic programming, as defined in section 2.1.3, to segment mammogram masses. The first step is to calculate the cost function ( $c(x, y)$ ), which they define as:

$$c(x, y) = w_s s(x, y) + w_d d(x, y) + w_g g(x, y) \quad (2.18)$$

where  $s(x, y)$  is the gradient strength,  $d(x, y)$  is the expected size of the mass and  $g(x, y)$  is the mean expected grayscale value. The weight for each component is given by  $w_s, w_d$  and  $w_g$ . Once the cost function is created, they changed the coordinate space from Cartesian to polar; an example is shown in Figure 2.6.

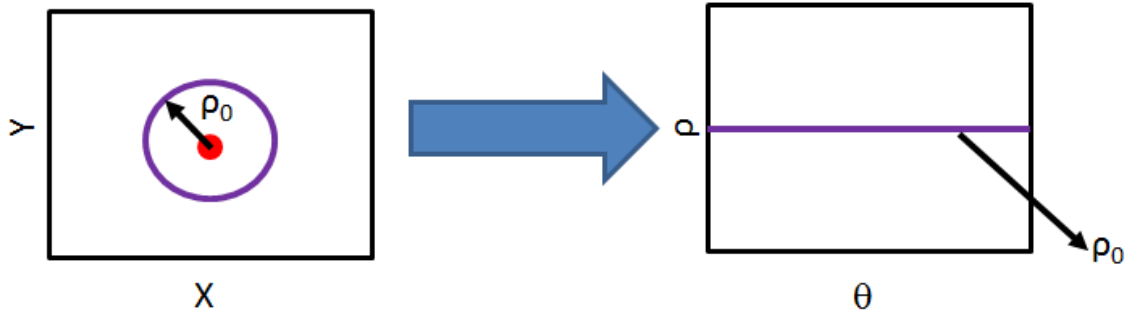


Figure 2.6 Cartesian to polar coordinate change.

This change of coordinates allowed circular objects to be outlined by finding a path in the polar representation of the image. The authors used the dynamic programming technique for finding the optimum path.

Unfortunately, the PDP has two major drawbacks that prevent it from being used as a general-purpose algorithm. First, it requires training data to constrain the size of the object being segmented. The size constraint helps prevent the closed contour from latching onto high-gradient regions that are not associated with the object. The second major drawback is that this algorithm cannot segment shapes for which rays emanating from the selected origin within the shape intersect the shape boundary in more than one point, for example a hand. To address these drawbacks, we developed a PDP with polar variance, which is described in Chapter 3.

### 2.3 Review of State-of-the-Art SAX Segmentation Algorithms

In [11], the authors did a survey on the cardiac segmentation literature. They divided the algorithms in two categories: those using training data (*supervised* algorithms) and those that rely only on analysis of derived features (*unsupervised* algorithms). The main drawback of the supervised algorithms is that when the training data does not accurately represent the test data,

the algorithm may give incorrect results [56]. The drawback of unsupervised algorithms is that they may converge to incorrect regions [57]. The hypothesis was that given “good” training data, supervised algorithms will outperform their unsupervised counterpart.

### 2.3.1 LV Segmentation Algorithms

Some unsupervised algorithms used for segmenting the LV include thresholding, active contours and dynamic programming techniques. The supervised algorithms included probabilistic atlas based schemes [58], active shape models [59] and active appearance models [60].

The 2009 MICCAI challenge showed that the semi-automated unsupervised algorithms that incorporated PDP (Lu *et al.* [61], and Huang *et al.* [63]), outperformed supervised algorithms such as Casta *et al.* [64], Wijnhout *et al.* [65] and O’Brien *et al.* [66].

### 2.3.2 RV Segmentation Algorithms

The most common unsupervised algorithms used for segmenting the RV include thresholding and active contours. The most common supervised algorithms used for RV segmentation included probabilistic atlas [67], active appearance models and active shapes models.

The 2012 MICCAI challenge again showed that semi-automated algorithms outperformed the automated counterparts, but in this case an active shape modeling technique (Grosgeorge *et al.*) [68] yielded the best results.

### 3 POLAR DYNAMIC PROGRAMMING USING POLAR VARIANCE

The PDP algorithm as defined in section 2.2.3, consists of two major drawbacks that prevent it from being used as a general-purpose algorithm. First, it requires training data to constrain the size of the object being segmented. The size constraint helps prevent the closed contour from latching onto high-gradient regions that are not associated with the object. The second major drawback is that this algorithm cannot segment shapes for which rays emanating from the selected origin within the shape intersect the shape boundary in more than one point, for example a hand. To allow the PDP algorithm to segment different-sized objects without needing training data, we introduce a preprocessing step where a polar variance image is calculated from the image. To allow the algorithm to segment complex shapes, we grow low-gradient regions of the contour. We provide experimental results comparing our algorithm, with five other active contour algorithms on a variety of test images.

#### 3.1 Algorithm Description

The proposed PDP algorithm begins with a simple PDP (sPDP) method to generate a closed contour representing a simple object shape. The first step of the sPDP algorithm is to preprocess the input image to obtain a *polar variance image*. The second step is to calculate the cost function needed by the dynamic programming algorithm. This includes generating the cost function in the uniform Cartesian space and later resampling to a uniform polar grid ( $U_p$ ). The third step is to use dynamic programming to generate a closed contour representing the object shape. The PDP algorithm then extends this contour by applying a localized region-growing technique for segmenting complex shapes.

### 3.1.1 Polar Variance Image

To obtain closed contours using dynamic programming, [70] and [73] had to constrain the size of the final segmentation by using training data. They constrained the size because the closed contour may latch onto high-gradient regions that are not associated with the object. Requiring training data to constrain the size of the final segmentation reduces the generalization of the algorithm; therefore, we introduce a preprocessing step to generate what we define as the polar variance image.

Given an image  $I$ , the first step is to normalize the intensities from 0 to 1. We then define each pixel in  $I$  as  $I(x, y)$  where  $(x, y)$  are the coordinates in the uniform grid and  $G(x, y)$  is the edge strength of  $I(x, y)$ . The edge strength with no Gaussian smoothing is generally calculated as

$$G(x, y) = |\nabla I(x, y)|^2, \quad (3.1)$$

whereas with Gaussian smoothing the edge strength is calculated as

$$G(x, y) = |\nabla[G_\sigma(x, y) * I(x, y)]|^2 \quad (3.2)$$

Here,  $G_\sigma(x, y)$  is a 2D Gaussian function with standard deviation  $\sigma$ ,  $*$  denotes linear convolution, and  $\nabla$  is the gradient operator. We assume that  $I(x, y)$  is scalar (i.e., a grayscale image), but the derivation can be generalized for higher dimensionality. Introducing an origin  $(x_o, y_o)$  allows us to represent  $I(x, y)$  and  $G(x, y)$  as  $f(\theta, \rho)$  and  $g(\theta, \rho)$  in polar coordinates as

$$\rho = \sqrt{(x - x_o)^2 + (y - y_o)^2} \quad (3.3)$$

$$\theta = \tan^{-1}\left(\frac{y - y_o}{x - x_o}\right) \quad (3.4)$$

$$f(\theta, \rho) = I(x, y) \quad (3.5)$$

$$g(\theta, \rho) = G(x, y) \quad (3.6)$$

Using the polar representation, we define the polar variance image as

$$V(\theta, \rho) = \int_0^\rho \int_{\theta-\gamma}^{\theta+\gamma} (f(\phi, r) - \bar{f}(\phi, r))^2 dr d\phi \quad (3.7)$$

where

$$\bar{f}(\theta, \rho) = \int_0^\rho \int_{\theta-\gamma}^{\theta+\gamma} f(\phi, r) dr d\phi \quad (3.8)$$

In these equations,  $\gamma$  is a smoothing parameter. The higher  $\gamma$  is, the more smoothed the polar variance image will be. Note that the polar variance image is cumulative because the integral spans radii from the origin to the pixel being analyzed. Although variance as a feature has been used for segmentation [69] and as a preprocessing technique [69][72], to the best of our knowledge ours is the first segmentation algorithm that calculates a cumulative variance based on polar region coordinates. Figure 3.1 shows the results of the polar variance image on two different scenarios. The SAX cardiac MR image, shown in Figure 3.1a, contains high-gradient regions that are not part of the RV (i.e. the object with the dot). Figure 3.1b shows an image where rays emanating from an origin (the dot) will intersect the hand boundary in more than one point. Figure 3.1c shows the polar variance image of Figure 3.1a. Note that the RV has low variance values, whereas high gradient regions that are not associated with the RV have high

variance values. Figure 3.1d shows the polar variance image of Figure 3.1b. Note that the polar variance image does not have low values in the entire hand boundary just in the regions where the rays intersect the shape boundary at only one point.

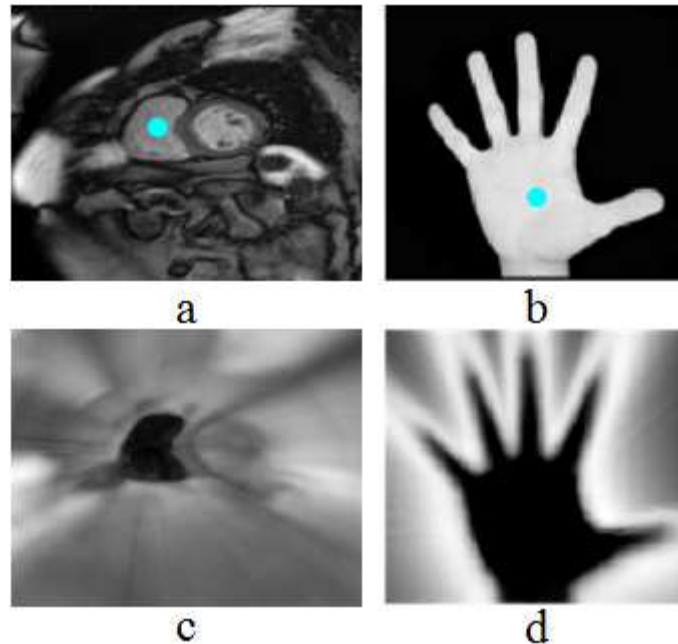


Figure 3.1 Grayscale and polar variance images. (a) SAX cardiac MR image and (b) hand image. (c-d) Polar variance images of (a) and (b) respectively. The dot denotes the object we wish to outline (RV in (a), the entire hand in (b)) and is used to calculate the polar variance image. Black in the polar variance images represents low variance.

### 3.1.2 Cost Function

The gradient and variance values are the features that will be optimized using dynamic programming. As a general rule, we want the variance values inside the closed contour to be low, and we want the gradient values along the contour to be high. Therefore, we define the cost function as

$$C(\theta, \rho) = \alpha V(\theta, \rho) + \beta \exp(-g(\theta, \rho)) \quad (3.9)$$

where  $\alpha$  and  $\beta$  are parameters for determining the importance of each feature.

### 3.1.2.1 Polar Resampling

To use dynamic programming as defined by [40], we require a uniform grid. Due to the discrete nature of  $I$ , its polar representation is not uniformly sampled. Therefore, we resample on a uniform polar grid ( $U_p$ ), which is the lattice comprising points  $(\theta_i, \rho_j) = (i\Delta\theta, j\Delta\rho)$  that span the image domain. We derive the sampling intervals ( $\Delta\rho$  and  $\Delta\theta$ ) to ensure that the polar grid has sufficient resolution to localize each pixel in the rectangular grid. First, we find the  $(x, y)$  coordinates that are farthest from the origin  $(x_o, y_o)$ . We consider a neighboring pixel (e.g., this could be the pixel at  $(x - 1, y)$  if the farthest point is at the upper-right corner), and then we compute the absolute radial difference between these two farthest pixels, which indicates the minimum required radial resolution:

$$\Delta\rho = \left| \sqrt{(x - x_o)^2 + (y - y_o)^2} - \sqrt{(x - 1 - x_o)^2 + (y - y_o)^2} \right| \quad (3.10)$$

As a general rule, the smaller the angular sampling interval ( $\Delta\theta$ ), the bigger the maximum allowed curvature of the extracted contour. To find the minimum  $\Delta\theta$  required to localize every pixel in the image, we find the angular difference between the two neighboring pixels farthest from the origin:

$$\Delta\theta_{min} = \left| \tan^{-1} \left( \frac{y - y_o}{x - x_o} \right) - \tan^{-1} \left( \frac{y - y_o}{x - 1 - x_o} \right) \right| \quad (3.11)$$

The  $\Delta\theta$  values used for analysis are multiples of  $\Delta\theta_{min}$ . Unlike active contours, our cost function (3.9) does not explicitly minimize the curvature of the extracted contour. Instead, the

curvature of the contour of the segmented object is based on the value of  $\Delta\theta$  we select. Figure 3.2 shows how the  $\Delta\theta$  value affects the curvature of the contour.

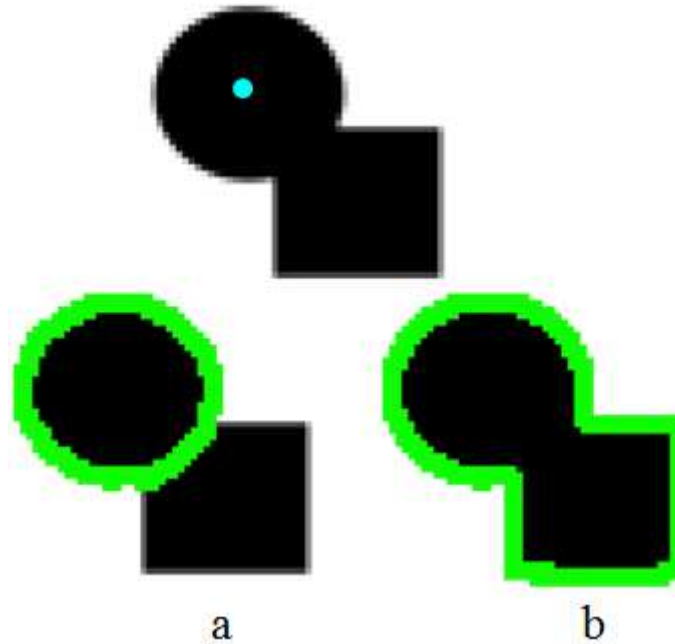


Figure 3.2 Assessing how  $\Delta\theta$  affects closed contour. For this example,  $\alpha$  and  $\beta$  equal 0.5. The dot is the origin used for PDP. Results using a  $\Delta\theta$  of (a)  $5^\circ$  and (b)  $0.1^\circ$ . Closed contours have been dilated for viewing purposes.

### 3.1.2.2 Interpolation

For each point  $(\theta_i, \rho_j) \in U_p$  we compute the corresponding Cartesian coordinates as

$$x = \rho_j \cos(\theta_i) \quad (3.12)$$

$$y = \rho_j \sin(\theta_i) \quad (3.13)$$

Then we use bilinear interpolation [73] to generate the cost function  $(C_P(\theta_i, \rho_j))$  from the cost function values at the four pixels that surround the point  $(x, y)$  in the Cartesian space.

### 3.1.3 Dynamic Programming

After generating a uniformly sampled polar representation of the cost function ( $C_p$ ), the next step is to use dynamic programming to compute the object contour by finding a path, as defined by [40]. This path, denoted as  $\rho_{path}(\theta_i)$ , is a function of  $\theta_i$  because the path will pass through only one radius value for each  $\theta_i$ . Also, the absolute radial difference between adjacent angles will be  $\Delta\rho$  or 0. The general approach is to find the radii that minimize the cumulative sum of the cost function ( $C_p$ ). To obtain a closed contour, the  $\rho_{path}$  value associated with  $\theta_i = 0^\circ$  and  $\theta_i = 360^\circ$  must be the same as [70][73]. To add this constraint to the dynamic programming, we use the technique described by Timp and Karssemeijer [70], which consists of extending  $\theta_i$  in a periodic fashion from  $[0^\circ, 360^\circ]$  to  $[-360^\circ, 720^\circ]$ . This extended version of the cost function is referred as  $C_p^*$ .

Given  $C_p^*$  we initialize the cumulative sum  $M_p$  as follows. To initialize we let  $M_p(-360^\circ, \rho_j) = C_p^*(-360^\circ, \rho_j)$  for each  $\rho_j$ . The other  $M_p$  values are recursively computed:

$$M_p(\theta_i, \rho_j) = \min\{M_p(\theta_i - \Delta\theta, \rho_j - \Delta\rho), M_p(\theta_i - \Delta\theta, \rho_j), M_p(\theta_i - \Delta\theta, \rho_j + \Delta\rho)\} + C_p^*(\theta_i, \rho_j) \quad (3.14)$$

for each  $\theta_i \in (-360^\circ, 720^\circ]$  and for each  $\rho_j$ .

Once  $M_p$  has been generated,  $\rho_{path}$  is initialized as follows:

$$\rho_{path}(720^\circ) = \underset{\rho}{\operatorname{argmin}} M_p(720^\circ, \rho) \quad (3.15)$$

The rest of the path, for  $\theta_i \in [-360^\circ, 720^\circ)$ , is created as follows:

$$\rho_{path}(\theta_i) = \underset{\rho \in \{\rho_{path}(\theta_i + \Delta\theta), \rho_{path}(\theta_i + \Delta\theta) + \Delta\rho, \rho_{path}(\theta_i + \Delta\theta) - \Delta\rho\}}{\operatorname{argmin}} M_p(\theta_i, \rho) \quad (3.16)$$

Note that  $\rho_{path}$  is defined for  $\theta_i \in [-360^\circ, 720^\circ)$ , just like  $M_p$ . To generate the closed contour, we only keep  $\rho_{path}$  for  $\theta_i \in [0^\circ, 360^\circ]$ . To convert to the Cartesian coordinate system, we use (3.12) and (3.13) to convert  $\rho_{path}$  and  $\theta_i$  to  $x$  and  $y$ .

### 3.1.4 Optimizing for Multiple $\Delta\theta$ Values

In case a single  $\Delta\theta$  does not suffice, we generate a closed contour using multiple  $\Delta\theta$  values (i.e., multiple curvature values), which are multiples of  $\Delta\theta_{min}$ , as discussed in Section 3.1.2.1. We select the  $\Delta\theta$  value that optimizes a cost function as follows:

$$\Delta\theta^* = \underset{\Delta\theta}{\operatorname{argmin}} \left( \alpha \int_{\Omega_1} V(x, y) dx dy + \beta \int_{\Omega_2} \exp(g(x, y)) dx dy \right) \quad (3.17)$$

where  $\Omega_1$  is the interior of the extracted closed contour and  $\Omega_2$  is the extracted closed contour.

We define the union of  $\Omega_1$  and  $\Omega_2$  as the mask,  $\Omega = \Omega_1 \cup \Omega_2$ .

### 3.1.5 Localized Region Growing

The simple PDP algorithm (sPDP) presented in Sections 3.1.1-3.1.4 can segment simple shapes for which rays emanating from an origin within the shape intersect the shape boundary in one point without the need for training data. However, this technique may generate undersized contours in the case of more complex shapes. To segment complex shapes, we grow the extracted closed contour ( $\Omega_2$ ) using the localized region growing procedure shown in Figure 3.3.

The procedure begins by localizing weak sub-contours (Figure 3.3 line 2). A weak sub-contour is

a region in  $\Omega_2$  that has a gradient magnitude less than or equal to the mean gradient magnitude in  $\Omega_1$ . For each weak sub-contour, we run SPDP with a new origin located on the weak sub-contour to produce a new mask ( $\Omega_2^{\text{new}}$ ) (Figure 3.3 lines 8-9). If the total length of the weak sub-contours in the new mask is less than the length of the weak sub-contour we are growing, then we keep the new mask (Figure 3.3 lines 11-14). We then mark the weak sub-contour we are growing as closed (Figure 3.3 line 15-16), we add any new weak sub-contours (Figure 3.3 line 19), and proceed to the next sub-contour. This is repeated until all the weak sub-contours have been examined.

```

procedure GROW( $\Omega, I, G, \gamma, \alpha, \beta, \Delta\rho, \Delta\theta$ )
Input  $\Omega$  is the initial segmentation calculated using the user selected
origin  $x_c, y_c$ .  $\Omega$  is the union of  $\Omega_1$  and  $\Omega_2$ , where  $\Omega_1$  is the region inside the
closed contour and  $\Omega_2$  is the extracted contour.  $I$  is the intensity image
and  $G$  is the gradient image.  $\gamma$  is the smoothing parameter for the polar
variance image (default value 5°).  $\alpha$  and  $\beta$  are the weight values for the
cost function (default values 0.5).  $\Delta\rho$  is the radial sampling interval
(default value 0.5) and  $\Delta\theta$  is the angular sampling interval (default value
is a multiple of  $\Delta\theta_{\text{min}}$ ).

Output  $\Omega$  is the grown region.

1. threshold = mean of  $G$  in  $\Omega_1$ 
2. weakEdges =  $(G \leq \text{threshold}) \cap \Omega_2$ 
3. Initialize closedEdges as a zero matrix the size of  $G$ 
4. while sum(weakEdges(:)) > 0 do
5.    $[x_n, y_n]$  = Point of the largest connected component of
6.   weakEdges that is the farthest away from a strong edge.
7.    $\Omega^{\text{new}}$  = SPDP( $I, G, x_n, y_n, \gamma, \alpha, \beta, \Delta\rho, \Delta\theta$ ) \ \ Sections II-A to II-D
8.    $\Omega^{\text{new}}$  =  $\Omega^{\text{new}} \cap \Omega^c \setminus \Omega^c$  is complement of  $\Omega$ 
9.    $\Omega^{\text{new}}$  is the connected component from  $\Omega^{\text{new}}$  that is closest to  $[x_n, y_n]$ .
10.  weakEdgesNew =  $(G \leq \text{threshold}) \cap \Omega^{\text{new}}$ 
11.  if the number of nonzero pixels in weakEdgesNew is smaller than
12.  the largest connected component of weakEdges then
13.     $\Omega = \Omega \cup \Omega^{\text{new}}$ 
14.  end if
15.  Take largest connected component of weakEdges and add it to the
16.  closedEdges
17.  threshold = mean of  $G$  inside the closed contour  $\Omega_1$ 
18.  weakEdgesTemp =  $(G \leq \text{threshold}) \cap \Omega_2$ 
19.  weakEdges =  $(\text{weakEdgesTemp} \cup \text{weakEdges}) \cap \text{closedEdges}^c$ 
20. end while
21. return  $\Omega$ 
end procedure

```

Figure 3.3 Pseudo code of localized region-growing (Section 3.1.5).

## 3.2 Results and Analysis

We compare the PDP algorithm to several segmentation algorithms [46][50][52][54] using a variety of tests. The first test measures the robustness to additive Gaussian noise. The second test measures segmentation accuracy using different grayscale images. The final test shows the robustness to algorithm-specific parameters.

The algorithms' performance is measured using the Dice metric [74] and the average border positioning error (BPE) [75]. The Dice metric finds the mutual overlap between the mask generated by the automated algorithm and the mask generated by manual segmentation (i.e., ground truth). The average BPE gives the mean difference (in pixels) between the automated and manual contours. An automated mask that perfectly matches the manual mask will yield an average Dice value of 1 and an average BPE of 0 pixels.

### 3.2.1 Parameter Selection

To achieve the best performance, the proper set of parameters needs to be used. Table 3.1 shows the algorithm-specific parameters that will be tuned to compare the algorithms. The ranges used for the parameters are the ones specified by the authors[46][52][54] in their work. In [52], the authors note that the CV algorithm[50] is just a specific formulation (zero-degree polynomial) of the generalized Legendre polynomial framework. Therefore, we rename the algorithm using the zero-degree polynomial ( $m = 0$ ) as the algorithm. Higher-degree polynomials are defined as the L2S algorithm. The algorithms described in [54] and [46] are defined as DRLSE and VFC, respectively.

The PDP method uses the following parameters:  $\gamma, \Delta\rho, \Delta\theta, \alpha, \beta, \sigma$ . For the images used in this paper (100 x 100 pixels), we use  $\gamma = 5^\circ$  and  $\Delta\rho = 0.5$  pixels. To further reduce our search space, we let  $\beta = 1 - \alpha$ . Even though (3.17) allows the PDP algorithm to handle multiple curvatures (see Section 3.1.4), for simplicity we use only one curvature value for the parameter selection. Note that the  $\Delta\theta$  values shown in Table I are multiples of  $\Delta\theta_{min}$ . For the images used in this paper,  $\Delta\theta_{min} = 0.1^\circ$ .

Aside from the parameters, the L2S, DRLSE, VFC and CV algorithms require a mask, whereas PDP requires an origin,  $(x_o, y_o)$ .

Table 3.1 Algorithm Specific Parameters.

Technique	Parameters	Description	Values
PDP	$\Delta\theta$	Allowed curvature	0.1,0.5,1,2,3,4,5
	$\alpha$	Variance image weight	From 0 to 0.9, $\Delta = 0.1$
	$\sigma$	Gaussian kernel smoothing	0,1.5
L2S	$m$	Legendre polynomial order	2,3
	$\lambda_1, \lambda_2$	Regularization constraints ( $\lambda_1 = \lambda_2$ )	From 1 to 100, $\Delta = 2$
	$\nu$	Contour smoothness constraint	From 0.05 to 0.6, $\Delta = 0.05$
DRLSE	$\lambda$	Line integral coefficient	From 0 to 10, $\Delta = 1$
	$\alpha$	Area coefficient ( $\alpha < 0$ expands, $\alpha > 0$ shrinks).	From -10 to 10, $\Delta = 1$
	$\sigma$	Gaussian kernel smoothing	0,1.5
VFC	$\tau$	Gradient edge threshold	From 0.1 to 0.8, $\Delta = 0.1$
	$\alpha$	Curvature weight	From 0 to 1, $\Delta = 0.1$
	$\gamma$	VFK decay coefficient	From 1.5 to 3, $\Delta = 0.5$
	$R$	VFK radii, based on the size of the image (N is the size of the image).	N/8,N/7,N/6,N/5,N/4,N/3,N/2
	$\sigma$	Gaussian kernel smoothing	1.5

CV	$\lambda_1, \lambda_2$	Regularization constraints ( $\lambda_1 = \lambda_2$ )	From 1 to 100, $\Delta = 2$
	$\nu$	Contour smoothness constraint	From 0.05 to 0.6, $\Delta = 0.05$

Notation from original papers, and  $\Delta$  is the uniform increment.

### 3.2.2 Sensitivity to Additive Gaussian Noise

To evaluate the performance of PDP under additive Gaussian noise, we add zero-mean Gaussian noise to a simulated crescent-shaped object, shown in Figure 3.4a, using 11 different signal-to-noise ratio (SNR) levels in the 0–10 dB range. The SNR [75] is calculated in terms of the mean intensity values as:

$$\text{SNR} = 10 \log_{10} \left( \frac{|\mu_{\text{object}} - \mu_{\text{background}}|}{\sigma_{\text{background}}} \right) \text{dB} \quad (3.18)$$

To ensure that the results are statistically significant, we used 100 noise realizations at each SNR level. Figure 3.4b and c show an instantiation of the 5 dB and the 0 dB cases. To find the parameters for the different algorithms, we randomly selected an image from each of the 11 noise levels and selected the set of parameters (shown in Table 3.1) that gave the best mean Dice metric. Figure 3.4a shows the initial contour used for L2S, DRLSE, and CV and the origin (shown as a dot) required for PDP. The results (i.e., average Dice and average BPE) for all the algorithms for different SNR levels are shown in Figure 3.5. At low SNR, the PDP and VFC algorithms perform the best, and at high SNR CV and L2S perform the best. One explanation for the low performance for CV and L2S at low SNR is that they do not smooth the input image as a preprocessing step and thus can be influenced by high noise. Conversely, the absence of smoothing allows these algorithms to generate good results at higher SNR levels.

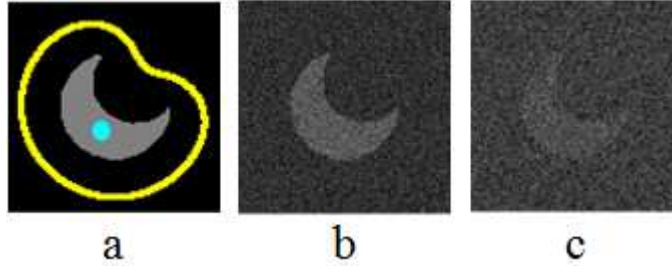
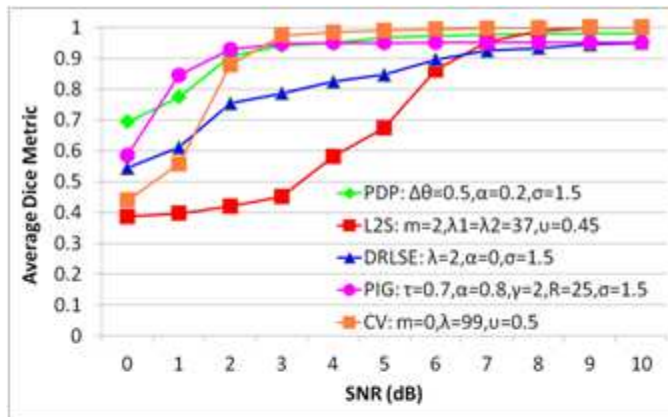
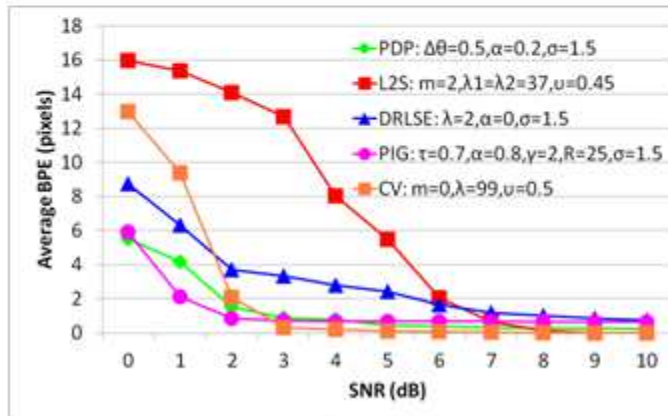


Figure 3.4 Simulated images with SNR values of (a)  $\infty$ , (b) 5 dB and (c) 0 dB. Outline in (a) is the initial closed contour used for L2S, DRLSE, VFC and CV; dot is the origin location used for PDP. Closed contour has been dilated for viewing purposes.



a



b

Figure 3.5 Noise sensitivity performance analysis for (a) average Dice performance and (b) average border positioning error (BPE) in pixels. One hundred noisy images were created for each SNR level by adding Gaussian noise to the image shown in Figure 3.4a.

### 3.2.3 Grayscale Images

To evaluate the performance of the algorithms with different grayscale images we used the non-medical and medical images shown in Figure 3.6. The first row shows the initialization contour for L2S, DRLSE, CV, as well as the initial origin (dot) used for PDP. The other rows show the closed contours obtained with the PDP, L2S, DRLSE, VFC, and CV algorithms. In Figure 3.6e and Figure 3.6f the algorithms are outlining the right ventricle and left atrium on cardiac MR images, respectively. The Dice metric and average BPE for the images are shown in Table 3.2. The proposed algorithm is able to segment high curvature objects with well defined edges similar to L2S or CV (e.g., Figure 3.6a, b, and c), while also being able to segment lower curvature objects with lower contrast (e.g., Figure 3.6d, e, and f), similar to the VFC algorithm.

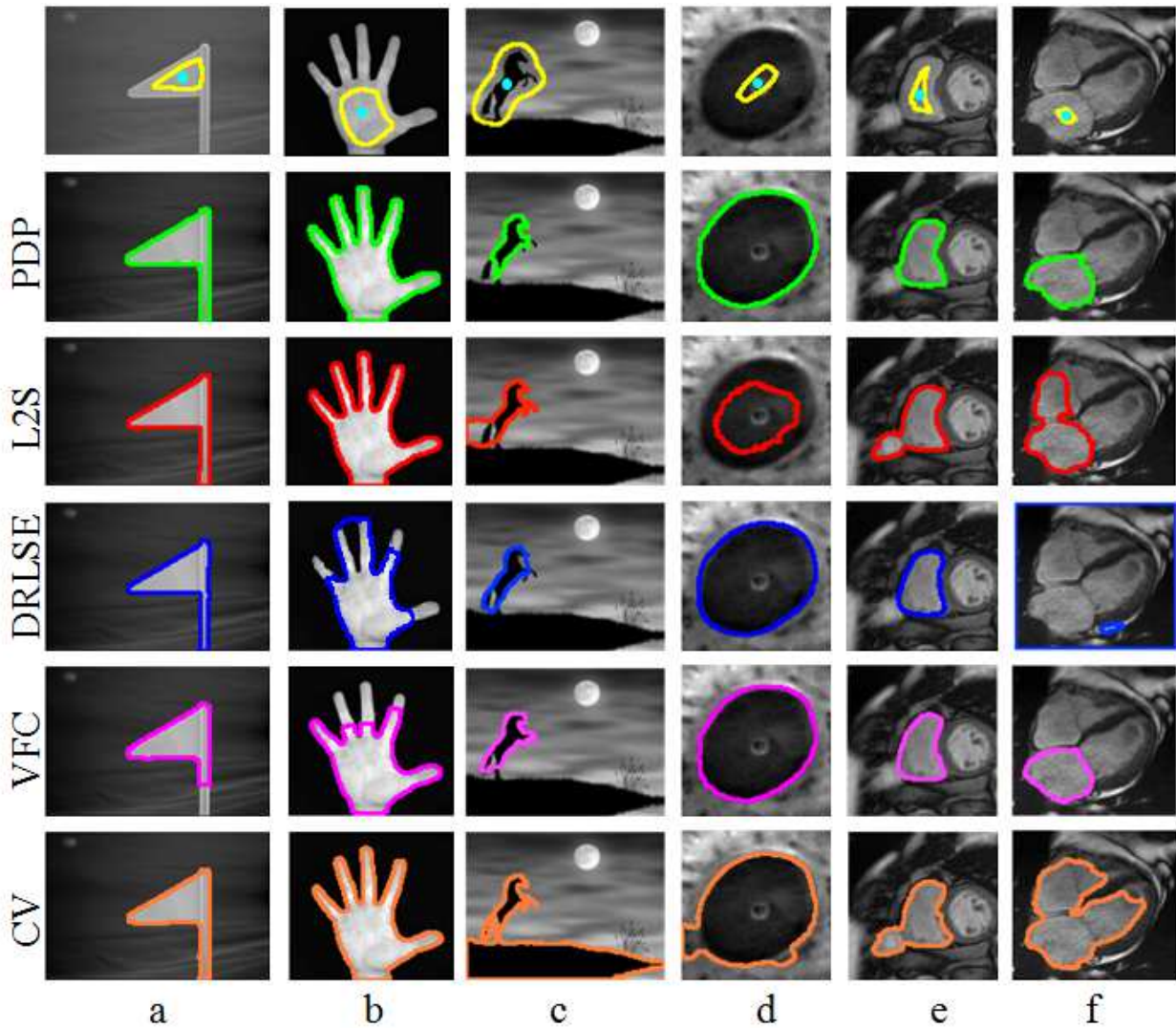


Figure 3.6 Non-medical and medical images. From left to right (a) flag, (b) hand, (c) horse, (d) retina, (e) short-axis and (f) 4CH cardiac image. Upper row shows the initialization for the different algorithms. Short-axis cardiac images (e) have been cropped for display purposes. The image used for analysis is shown in Figure 3.1a. Closed contours have been dilated for viewing purposes.

Table 3.2 Performance of Segmentation Algorithms.

Technique	Flag		Hand		Horse		Retina		SAX RV		4CH left atrium	
	Dice	BPE	Dice	BPE	Dice	BPE	Dice	BPE	Dice	BPE	Dice	BPE
PDP	0.9631	0.5213	0.9491	0.7190	0.8733	1.1024	0.9947	0.2172	0.9543	0.7172	0.9549	0.8186
L2S	0.9399	0.8163	0.9762	0.3451	0.7761	1.7970	0.5694	13.3977	0.8701	2.4988	0.7351	5.6670
DRLSE	0.9159	1.1163	0.8662	2.4240	0.8587	1.1323	0.9895	0.4297	0.9371	0.9655	0.1964	37.1450
VFC	0.9018	2.0213	0.8822	2.7598	0.8756	0.9699	0.9983	0.0685	0.9394	0.9195	0.9335	1.2021
CV	0.9471	0.7340	0.9741	0.3798	0.2618	21.4422	0.9324	2.4891	0.8484	2.7902	0.5187	12.0072

Quantitative performance for images shown in Figure 3.6.

The main limitation of the PDP algorithm is shown in Figure 3.7, which is a schematic of the tail region of the horse shown in Figure 3.6c. Given a weak sub-contour, shown as a thick black line in Figure 3.7a, the localized region-growing (Section 3.1.5) finds a new origin, shown in Figure 3.7b, and generates a new mask. To add the new mask ( $\Omega^n$ ) to the prior mask ( $\Omega$ ), the number of low-gradient pixels in the new extracted closed contour must be less than the number of pixels in the weak sub-contour. Since the sPDP segmentation (Sections 3.1.1-3.1.4) finds the optimum path given that the rays emanating from the new origin within the shape intersect the shape boundary in one point, the new mask is not the entire tail, but a subsection of the tail, shown in Figure 3.7c. Since the weak gradient region of the new mask, shown as a thick black line in Figure 3.7c, is bigger than the weak sub-contour, the weak sub-contour is marked as closed and thus the algorithm fails to outline the horse tail.

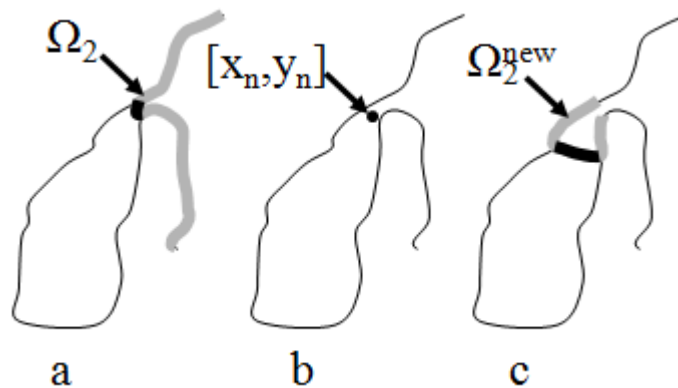


Figure 3.7 Schematic of the tail region of the horse shown in Figure 3.6c. The thin black line represents the high gradient region and the white background is the low gradient region. (a) The gray thick line shows part of the high gradient extracted contour of the original mask. The black thick line is the weak sub-contour. (b) The dot is the new origin positioned in the middle of the weak sub-contour shown in (a). (c) The gray thick line is the high gradient extracted contour that does not intersect with the original mask, (a).

### 3.2.4 Parameter Robustness

Aside from the segmentation accuracy, we also evaluated the robustness of the algorithm-specific parameters shown in Table 3.1. We selected the parameters that generated the masks shown in Figure 3.6 and changed them by  $\pm 1$ ,  $\pm 5$ ,  $\pm 10$  and  $\pm 15$  percent. Table 3.3 shows the mean difference between the performance metrics given the change in parameters. These changes were done with some constraints (shown in Table 3.3) to generate valid values. For example, in PDP and DRLSE there can be smoothing ( $\sigma = 1.5$ ) or no smoothing ( $\sigma = 0$ ). Non-positive  $\sigma$  values are not valid; therefore, in cases where a non-smoothed gradient ( $\sigma = 0$ ) generated the best result,  $\sigma = 0.01, 0.05, 0.1, 0.15$  were used instead.

Positive values in Table 3.3 show performance degradation, meaning that the masks generated with the new parameters yielded a smaller Dice metric or higher average BPE than the ones generated with the initial parameter. A negative value (i.e., improvement) means that using the new parameter generated a mask with either a higher Dice metric or a lower average BPE than the initial parameter. There are cases where the Dice metric gives a positive value while the average BPE shows a negative value. One reason may be that we are using the parameters that optimize the Dice metric, not the average BPE.

As seen in Table 3.3, the performance of PDP is mostly influenced by  $\alpha$ . As a general rule, the value of  $\alpha$  should be selected as follows. To segment an object with one mode (e.g., Figure 3.6e) the value of  $\alpha$  should be in the 0.6-0.9 range. When segmenting an object that has more than one mode, but its gradient magnitude is high compared to the background (e.g., Figure 3.6d), the value of  $\alpha$  should be in the 0-0.3 range. For high-curvature objects (e.g., Figure 3.6b), a  $\Delta\theta$

value close to  $\Delta\theta_{min}$  should be used. For low-curvature objects,  $\Delta\theta$  should be a multiple of  $\Delta\theta_{min}$ . Even though changing  $\Delta\theta$  resulted in a Dice metric improvement, the improvement is negligible.

The L2S algorithm was not affected by changes to  $\lambda_1$  and  $\lambda_2$ ; for  $\nu$  the degradation was fairly small. A change of  $\pm 15\%$  in  $\nu$  produced a degradation of less than 5% in the mean Dice metric and a bias of less than 2 pixels for average BPE. For L2S the polynomial order ( $m$ ) turned out to be a sensitive parameter in this set of images. Unlike most of the parameters shown in Table 3.1,  $m$  could only have two possible values, 2 or 3. We quantified the effect on the performance by using the incorrect polynomial order (e.g.,  $m = 2$  instead of  $m = 3$  for L2S). Using this approach we observe on average a degradation of 0.2 in the Dice metric for selecting the wrong polynomial order.

All the DRLSE parameters were sensitive to small variations. The performance for VFC was sensitive to all the parameters except  $\alpha$ . The main problem of the algorithm was the inability to generate an initial closed contour that was on the object we wanted to segment. This is one of the main drawbacks of using a purely automated method for creating the mask. The most robust algorithm was CV. It was robust to changes in  $\lambda_1, \lambda_2$  and  $\nu$ . A change of  $\pm 15\%$  in  $\nu$  resulted in less than a 1% in degradation in the Dice metric and a bias of less than 0.01 pixel.

Table 3.3 Robustness to Changes in Algorithm-Specific Parameters.

Technique	Parameters	Constraints	$\pm 1\%$		$\pm 5\%$		$\pm 10\%$		$\pm 15\%$	
			$\Delta$ Dice	$\Delta$ BPE						
PDP	$\Delta\theta$	$\Delta\theta > 0$	-0.0019	-0.0179	-0.0020	-0.0238	-0.0016	-0.0253	-0.0026	-0.0348
	$\alpha$	$0 \leq \alpha < 1$	0.0037	0.0732	0.0122	0.1978	0.0904	1.6847	0.094	1.8223
	$\sigma$	$\sigma > 0$	-0.0004	-0.0046	0.0076	0.1158	0.0076	0.1188	0.0138	0.2052
L2S	$m$	If $m_{old} = 2$ $m_{new} = 3$ if $m_{old} = 3$ $m_{new} = 2$	0.1810	3.1189	0.1810	3.1189	0.1810	3.1189	0.1810	3.1189
	$\lambda_1, \lambda_2$	$\lambda_1, \lambda_2 > 0$	0	0	0	0	0	0	0	0
	$\nu$	$0 \leq \nu \leq 1$	0.0001	0.0005	-0.0002	0.0062	0.0384	1.2301	0.044	1.7981
DRLSE	$\lambda$	$\lambda > 0$	0.0359	1.7321	0.0453	2.3018	0.0999	3.997	0.2402	8.0538

	$\alpha$	if $\alpha_{old} > 0, \alpha_{new} > 0$ if $\alpha_{old} < 0, \alpha_{new} < 0$	0.0379	2.0672	0.0598	2.4183	0.1819	4.3407	0.2158	5.1481
	$\sigma$	$\sigma > 0$	0.1118	4.6195	0.1585	7.385	0.1136	5.2672	0.1283	5.8768
VFC	$\tau$	$0 \leq \tau < 0.8$	0.0793	4.3448	0.1025	9.1074	0.1691	8.7681	0.2097	15.0553
	$\alpha$	$0 \leq \alpha \leq 1$	0.0018	0.0691	0.0040	0.1397	0.0026	0.1051	0.0026	0.0941
	$\gamma$	$\gamma > 0$	0.0068	0.1474	0.0882	4.5255	0.0931	4.6330	0.0970	4.6336
	$R$	$R > 0$	0.0814	4.4366	0.0824	4.3897	0.0859	4.4776	0.0923	4.5874
	$\sigma$	$\sigma > 0$	0.1681	8.6817	0.1997	9.2172	0.1799	8.3331	0.1667	8.7000
CV	$\lambda_1, \lambda_2$	$\lambda_1, \lambda_2 > 0$	0	0	0	0	0	0	0	0
	$\nu$	$0 \leq \nu \leq 1$	0.0014	0.0226	0.0011	-0.0149	-0.0016	-0.0047	0.0013	0.0078

Change in Dice metric and BPE when the parameters used in Figure 3.6 are altered by  $\pm 1, 5, 10, 15$ .

### 3.3 Conclusion

We developed an algorithm that uses PDP to outline complex shapes. By introducing the polar variance image, we did not have to constrain the size of the object for correct boundary delineation, something that previous implementations of PDP [70],[73] were not able to accomplish. The proposed algorithm is able to segment high curvature objects, while also segmenting low-gradient objects. We showed that our technique performed favorably when compared to other segmentation algorithms. In future work we will extend the algorithm to segment 3D objects.

## 4 4CH RV SEGMENTATION USING DYNAMIC PROGRAMMING

In this chapter we describe a novel segmentation algorithm for the RV in 4CH CMR images with the goal of using the segmented images to evaluate RV function. As mentioned in Chapter 1 the advantage of using standard 4CH views is that the relevant RV landmarks (i.e., TV plane, apex and free wall) are clearly visible in the 4CH views and there is no need to change the existing CMR protocols. The proposed algorithm uses anatomical constraint lines and user-provided landmarks to segment the RV.

### 4.1 Algorithm Description

The proposed technique consists of the following steps: (1) automatic segmentation of the cardiac region of interest (ROI); (2) user identification of the ED and ES frames along with the appropriate landmarks; (3) automatic propagation of landmarks throughout the cardiac cycle; (4) automatic identification of the septum and (5) final segmentation of the RV (given the septum and the propagated landmarks). (6) The semi-automated RV segmentation masks can be smoothed in the temporal axis to produce a temporally smoothed segmentation mask. (7) As an optional feature, the proposed technique can exclude the trabeculae if needed, when the user chooses to focus only on the blood pool (BP) part of the RV. These steps are outlined in Figure 4.1.

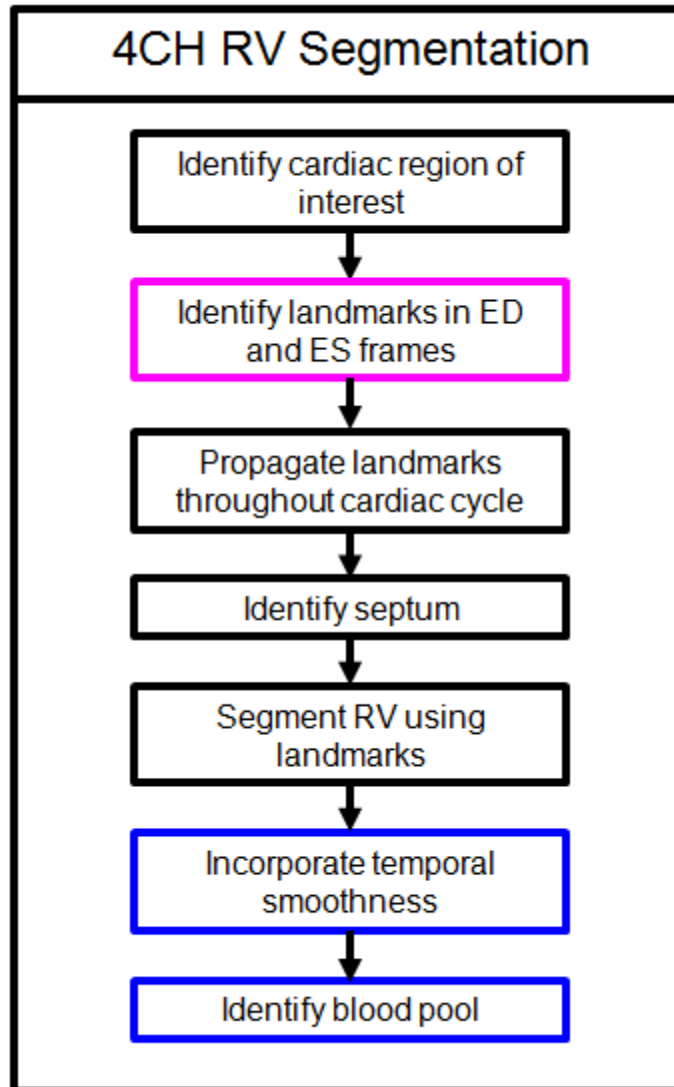


Figure 4.1 4CH Segmentation Flowchart. Magenta denotes the module that requires user interaction; blue denotes optional modules.

#### 4.1.1 Identify Cardiac Region of Interest

The first step of our technique is to identify the cardiac ROI. Consider a 4CH image sequence of the cardiac cycle, where we define each pixel as  $I(x, y, n)$  where  $n$  is the frame number and  $(x, y)$  are the coordinates within the given frame. To automatically identify the cardiac ROI, we

identify the pixels where there is motion – specifically, we check for a high standard deviation of pixel intensity throughout the cardiac cycle. The *standard deviation image* is defined as

$$\sigma_I(x, y) = \sqrt{\frac{1}{N-1} \sum_{i=1}^N |I(x, y, i) - \mu_I(x, y)|^2} \quad (4.1)$$

where

$$\mu_I(x, y) = \frac{1}{N} \sum_{i=1}^N I(x, y, i) \quad (4.2)$$

$N$  is the number of frames in the cardiac cycle; in our experiments  $N = 25$ . High values of  $\sigma_I$  denote high intensity variability throughout the cardiac cycle, which we associate with cardiac movement. Therefore, to find the cardiac ROI we threshold  $\sigma_I$ , using k-means++ [76]; other techniques such as Otsu [77] or fuzzy C-means [78], would also be effective for thresholding. Once we threshold  $\sigma_I$ , we define the cardiac ROI as the bounding box of the largest connected component as illustrated in Figure 4.2a-b. For subsequent processing, we only analyze the pixels that reside cardiac ROI.

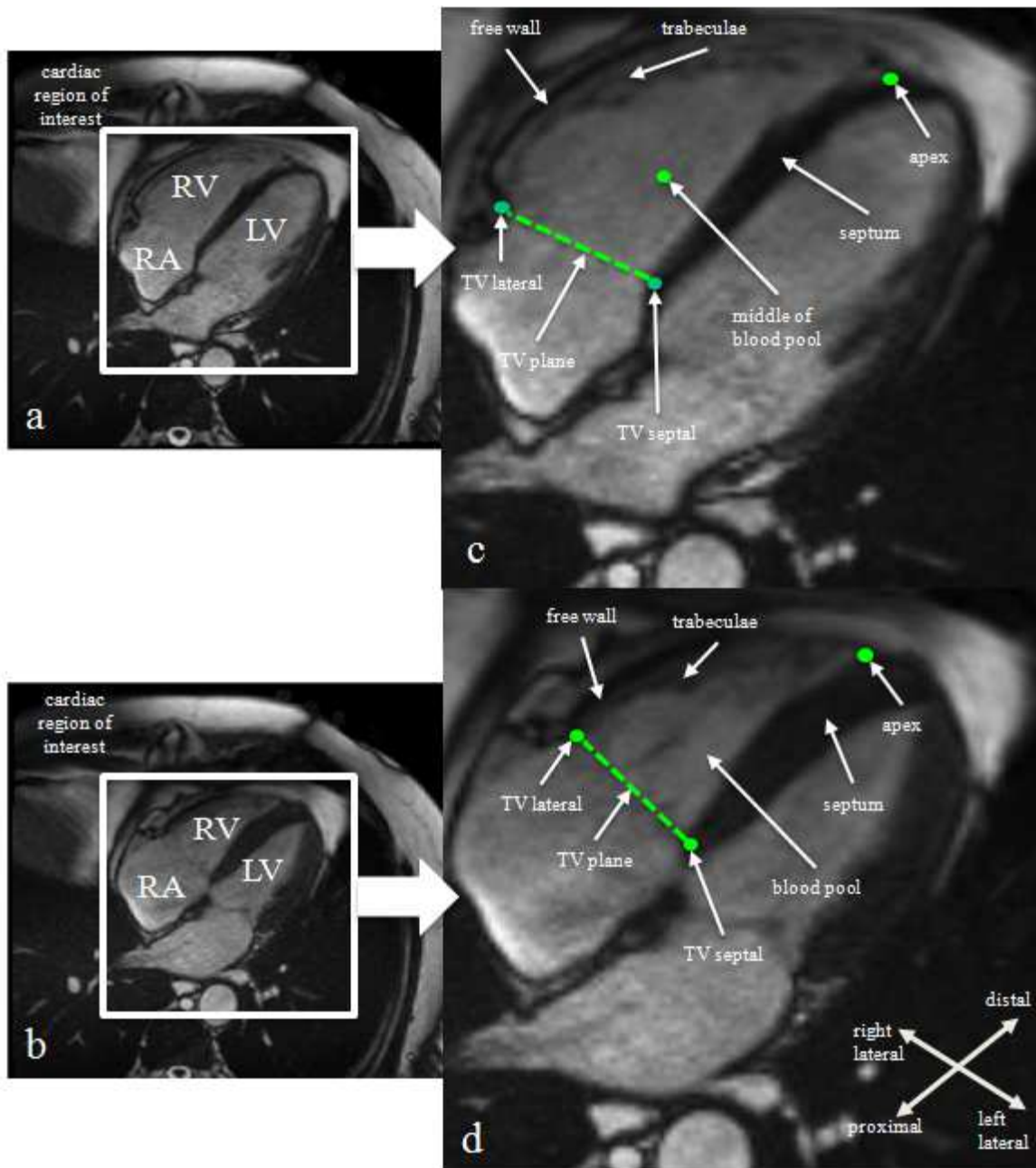


Figure 4.2 4CH CMR image at (a) ED and (b) ES. The zoomed cardiac region of interest at ED and ES is shown in (c) and (d). The RV anatomical landmarks are annotated in (c) and (d). Landmarks that will be selected by users of the technique are shown as circles in (c) and (d).

#### 4.1.2 Identify landmarks in ED and ES frames

The second step in our algorithm is the user identification of the ED and ES frames. The ED frame is the frame that qualitatively shows the RV at its largest size. Once selected, the user identifies the following landmarks: the apex, both sides of the TV (i.e., lateral and septal) and the middle of the BP, shown in Figure 4.2c. The apex can be found by selecting the region where the free wall and the septum intersect. The left lateral side of the TV is located in the proximal part of the septum (i.e. where the septum becomes thinner); the right lateral side of the TV is next to the atrial insertion point (i.e., follow the free wall from the apex, and localize the indentation). Standard anatomic landmarks were utilized to identify the TV. The middle of the BP is a point near the center of the RV that has a high intensity (i.e., blood pixel).

The ES frame is the frame that qualitatively shows the RV at its smallest size. There may be multiple frames that qualitatively appear to contain the smallest RV area. In this case, the ES frame is the frame where the midpoint of the TV looks the closest to the apex. Once the ES frame is selected, the user identifies the apex and both sides of the TV (i.e. lateral and septal). Since the TV is closed in the ES frame, the valve is clearly visible in the image and the TV landmarks are selected from the intersection between the TV line with the free wall (TV lateral landmark) and septum (TV septal landmark). The middle of the BP landmark is not selected in the ES frame because the algorithm propagates the landmark automatically from the ED frame, as indicated below.

#### 4.1.3 Propagate landmarks throughout the cardiac cycle

For each of the user-selected landmarks, the technique finds the minimum cost trajectory of the specific landmark throughout the cardiac cycle. Although there are multiple shortest path algorithms [35],[81], we use dynamic programming [40], which we modify so that the path intersects each frame at just a single point.

The cost function ( $C_f$ ) that is used for the propagating the BP landmarks is the edge strength of  $I(x, y, n)$ , which is calculated by using equation (3.2) on each frame. For the other landmarks, ( $C_f$ ) is  $I$  because the shortest path will follow a low intensity point throughout the cardiac cycle.

To make sure that the technique selects the landmark as part of the path, we add a constant value to  $C_f$ , and we set the cost to zero at the user-selected landmark locations. The constant value is the maximum of the number of elements of  $C_f$  and the maximum value of the array.

For the path to be smooth, we want the location of the landmark at frame 1 to be adjacent to the location of the landmark at frame  $N$ . To add this constraint to the dynamic programming, we extend  $C_f$  along the temporal dimension in a periodic fashion from  $[1, N]$  to  $[-N + 1, 2N]$ . This extended version is referred to as  $C_f^*$ .

Given  $C_f^*$  we initialize the cumulative sum used in dynamic programming to be  $M_f(x, y, -N + 1) = C_f^*(x, y, -N + 1)$  for each  $x, y$ . The other  $M_f$  values are recursively computed:

$$M_f(x, y, n) = \left[ \min_{\Omega} M_f(x_f, y_f, n - 1) \right] + C_f^*(x, y, n) \quad (4.3)$$

where

$$\Omega = \{(x_f, y_f): |x_f - x| \leq d_x, |y_f - y| \leq d_y\} \quad (4.4)$$

for each  $n \in [-N + 2, 2N]$  and for each  $(x, y)$ , where  $(d_x, d_y)$  represent the step size used in the dynamic programming search. For each landmark, the step size  $(d_x, d_y)$  is calculated to be the average landmark displacement per frame:

$$d_x = \frac{|x_{ED} - x_{ES}|}{\tau_{ED,ES}} \quad (4.5)$$

$$d_y = \frac{|y_{ED} - y_{ES}|}{\tau_{ED,ES}} \quad (4.6)$$

where

$$\tau_{ED,ES} = \min(|ED - ES|, N - |(ED - ES)|) \quad (4.7)$$

Here  $(x_{ED}, y_{ED})$  and  $(x_{ES}, y_{ES})$  are the landmark's  $(x, y)$  coordinates for the ED and ES frame, respectively. For the middle of the BP, we set  $d_x = d_y = 1$  to reduce the amount of movement of the landmark throughout the cardiac cycle.

Let us denote the path as  $P = (p_1, \dots, p_{2N})$ , where  $p_n = (x_n, y_n)$ . Once  $M_f$  has been generated, the path is initialized as follows

$$p_{2N} = \underset{x,y}{\operatorname{argmin}} M_f(x, y, 2N) \quad (4.8)$$

The rest of the path is created as follows

$$p_n = \underset{\Omega^*}{\operatorname{argmin}} M_f(x, y, n) \quad (4.9)$$

where

$$\Omega^* = \{(x, y): |x - x_{n+1}| \leq d_x, |y - y_{n+1}| \leq d_y\} \quad (4.10)$$

#### 4.1.4 Identify Septum

The septum is a low intensity region within the cardiac ROI that separates the RV from the LV. The free wall is also a low intensity region, so we use the following technique to ensure that the free wall is not accidentally included as part of the septum. On each frame we threshold  $I(x, y, n)$  to find the low intensity regions inside the cardiac ROI. Then, we modify those low intensity regions to exclude any pixels that fall outside an ellipse of the form,

$$\frac{(x \cos(\alpha) - y \sin(\alpha) + t_x)^2}{a^2} + \frac{(x \sin(\alpha) + y \cos(\alpha) + t_y)^2}{b^2} = 1 \quad (4.11)$$

where

$$a = \frac{\sqrt{(x_{AP} - x_{TV_s})^2 + (y_{AP} - y_{TV_s})^2}}{2} \quad (4.12)$$

$$b = \frac{a}{2} \quad (4.13)$$

$$\alpha = \tan^{-1} \left( \frac{y_{AP} - y_{TV_s}}{x_{AP} - x_{TV_s}} \right) \quad (4.14)$$

$$t_x = \text{round} \left( \frac{x_{AP} + x_{TV_s}}{2} \right) \quad (4.15)$$

$$t_y = \text{round} \left( \frac{y_{AP} + y_{TV_s}}{2} \right) \quad (4.16)$$

Here  $(x_{AP}, y_{AP})$  and  $(x_{TV_s}, y_{TV_s})$  are the  $(x, y)$  coordinates for the apex and the septal part of the TV landmarks, respectively. We assume a 2:1 aspect ratio for the ellipsoidal fit of the septum region.

#### 4.1.5 Segment RV Using Landmarks

Given the propagated landmarks and the septum at each frame, we proceed to segment the RV throughout the cardiac cycle. The contour that outlines the ventricle is obtained as follows: first the technique constructs an RV ROI; second it outlines the free wall; third it finds the endocardial border; and fourth it joins the septal and lateral sides of the TV, using a straight line, to form the border corresponding to the TV. The endocardial border is the high gradient region that divides the BP from the septum and goes from the apex to the septal part of the TV. A smoothing operation is performed to ensure a smooth RV contour. A morphological filling operation [79] is carried out to generate a mask from the contour.

##### *4.1.5.1 Right Ventricular Region of Interest (RV-ROI)*

The segmentation procedure begins by finding a sub-region within the cardiac ROI that pertains to the RV-ROI. For the ED frame the RV-ROI is the overlap between the cardiac ROI and the rectangle consisting of lines  $L_1$ ,  $L_2$ ,  $L_3$  and  $L_4$ , shown in Figure 4.3. Letting  $d$  denote the pixel distance between the lateral and septal sides of the TV, construct  $L_1$  as a line perpendicular to the TV positioned  $d$  pixels right lateral from the lateral side of the TV. Construct lines  $L_2$  and  $L_3$  parallel to the TV positioned  $d/5$  pixels proximal from the TV and distally from the apex, respectively. Finally, construct  $L_4$  as a line perpendicular to the TV positioned  $d/5$  pixels left lateral from the apex. For subsequent frames, the ROI is formed by taking the final, semi-automated RV mask in the ED frame and applying morphological dilation [80] using a  $3 \times 3$  square operator. The pixel locations that fall outside the ROI but inside the cardiac ROI will be given a fixed cost function value in the subsequent steps of the segmentation procedure.

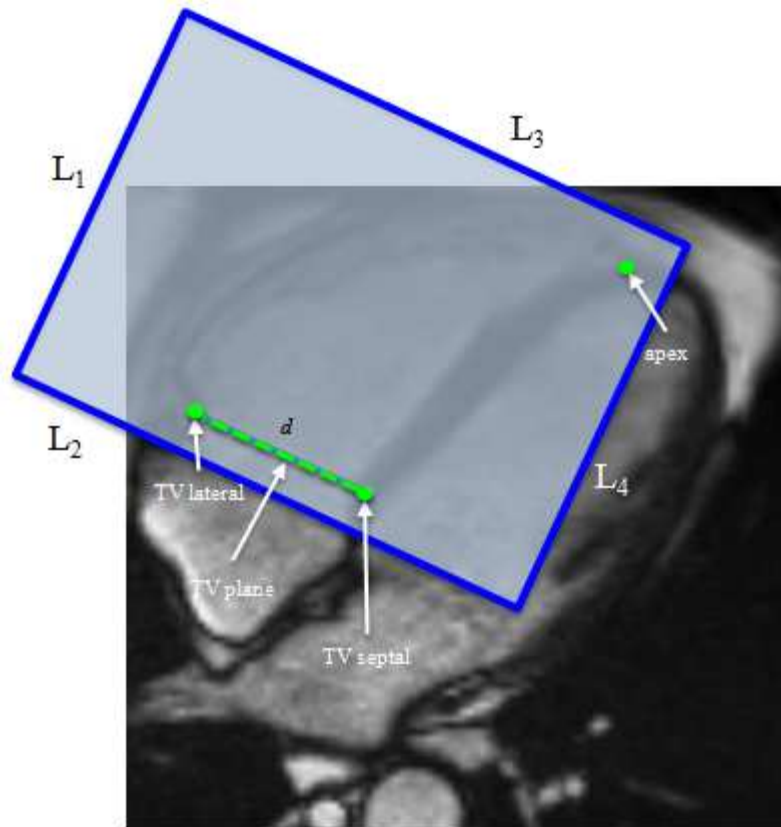


Figure 4.3 The RV-ROI is the overlap between the rectangle created by lines  $L_1$ ,  $L_2$ ,  $L_3$  and  $L_4$  and the cardiac region of interest.

#### 4.1.5.2 Outline the Free Wall

The contrast between the trabeculae and the BP is greater than the contrast between the trabeculae and the free wall. This is why active contour algorithms that rely on gradient strength to achieve a minimum cost spline [46][52][54] will latch onto the trabeculae/blood pool boundary rather than the free wall. Since the free wall has lower mean intensity than the trabeculae, minimum shortest path techniques are used for this task.

We compare three different techniques for outlining the free wall: Dijkstra's shortest-path algorithm [35], Strandmark's ALCT algorithm [81] and a modified version of the algorithm

described in Chapter 3. For [35] and [81] we use  $I(x, y, n)$  as the primary component for the cost function. To restrain the minimum cost path from going into the septum, we set all the pixels in the septum to have the highest value in the cost function for the given frame. Unlike Dijkstra's algorithm, which uses no parameters, ALCT uses an A\* algorithm [38] that incorporates length, curvature and torsion penalties in an active contour model to find the minimum cost path. The method for selecting the parameters for both ALCT and PDP is explained in the section 4.3.3.

The PDP algorithm finds a segmentation mask by finding a path using polar coordinates. The technique used for finding the path is dynamic programming [40]. The inputs to the algorithm described in Chapter 3 are the intensity image  $I(x, y, n)$ , and the gradient strength  $G(x, y, n)$  defined by (3.1) or (3.2). To ensure that the free wall does not latch onto the trabeculae/BP boundary we replace  $G(x, y, n)$  with

$$G(x, y, n) = \max_{x,y} I(x, y, n) - I(x, y, n) \quad (4.17)$$

This new definition of the gradient strength will give high values to the free wall, allowing the PDP to latch to the free wall. Given  $I(x, y, n)$  and  $G(x, y, n)$ , we create the cost function using equations (3.3)-(3.9). The origin used in eqs (3.3) and (3.4) is the middle of the BP landmark.

To incorporate the landmarks into this cost function, we set the cost to zero at the polar coordinates associated with the lateral portion of the TV and the apex for a given frame, and add a constant value to the other cost function values in a given frame ( $n$ ). The constant value is set to the number of elements in the  $C(\theta, \rho, n)$  array. Given the  $C(\theta, \rho, n)$  array we find the closed contour using the technique outlined in section 3.1.3. The algorithm described in Chapter 3

generates a closed contour that may include regions that are proximal to the TV or overlap with the septum. Any part of the segmentation mask that is proximal to the TV or in the septum is removed.

#### *4.1.5.3 Identifying septum-BP border*

Given the free wall, the technique proceeds to find the septum-BP border. For each frame we calculate the cost function by first calculating the edge strength as defined by (3.2). Next we subtract the edge strength from the maximum edge strength. Given this cost function, the septum-BP border is the minimum cost path from the apex to the septal portion of the TV. To find the septum-BP border, we use Dijkstra's shortest-path algorithm.

#### 4.1.6 Incorporate Temporal Smoothness

Given the semi-automated segmentation of the RV in 4CH cardiac images, we smooth the segmentation by applying a 1D median filter [82] in the temporal dimension. For all patients we used a filter size of 5. The median filter in the temporal dimension is implemented as follows: for each  $(x, y)$  coordinate, look at its 2 nearby neighbors in the temporal dimension. Apply a median filter to those binary values. We keep the constraint in the previous section that removes every pixel that is proximal to the TV. The temporal smoothness will remove outlying traces at the expense of reducing metrics such as fractional area change.

#### 4.1.7 Identifying Blood Pool

As shown in Figure 4.2c-d, the RV is composed of the trabeculae and the BP. The impact of including the trabeculae in SAX CMR views is assumed to be small in healthy individuals [83];

no such analysis has been done for 4CH views. An advantage of the proposed technique is that it can automatically exclude trabeculae from the semi-automated segmentation of the RV if needed. The BP is defined as the largest connected component inside the semi-automated segmentation of the RV that has an intensity value higher than a threshold. To find the threshold, we first calculate the histogram of  $I(x, y, n)$  at the locations of the septum and the RV, respectively and compare the frequency for each intensity bin. The threshold is the highest intensity bin where the frequency of the septum is higher than the frequency of the RV.

## 4.2 Manual Tracing Protocol

In [84] Schulz-Menger *et al.* outlined a series of recommendations to improve the reproducibility of the RV segmentation in 4CH and SAX CMR images. One main recommendation is to include the RV trabeculae within the BP volume to improve reproducibility. A second recommendation is to draw a smooth endocardial border. Even though it is not explicitly said in [84], we noticed that the authors approximate the TV using a line that connects the septal and lateral sides of the TV.

Manual tracing was performed two radiologists and a cardiologist, each with at least 5 years of training and experience in the interpretation of CMR images. To allow for human variability and biases in the manual tracing, each tracer was blinded to the others' work.

### 4.3 Data and Performance Metrics

#### 4.3.1 Data

To evaluate the segmentation performance we analyzed 175 images coming from 7 different patients (25 frames per patient). Images were acquired in a Siemens 1.5T Aera scanner, using a cine steady-state free-precession pulse sequence (TR = 2.7-2.8 ms, TE = 1.16 ms, acq. matrix = 168 x 192, FOV = 29.8 x 34 cm; slice thickness = 6 mm) and a phased array flex body coil.

#### 4.3.2 Performance Metrics

The performance metrics used for analysis are the Dice Metric [74], FAC and the correlation coefficient (R) [85]. The latter measures the closeness of data points to a regression line of the form  $y = mx + b$ , and is defined as

$$R = \frac{\sum_{i=1}^N (x_i - \bar{x})(y_i - \bar{y})}{\sqrt{[\sum_{i=1}^N (x_i - \bar{x})^2][\sum_{i=1}^N (y_i - \bar{y})^2]}} \quad (4.18)$$

where

$$\bar{x} = \frac{1}{N} \sum_{i=1}^N x_i \quad (4.19)$$

and

$$\bar{y} = \frac{1}{N} \sum_{i=1}^N y_i \quad (4.20)$$

Here  $x$  and  $y$  represent two samples. For our experiment,  $N = 7$ . The sign of R will be the same as the sign of the slope ( $m$ ) of the regression line. Values of R close to one indicate a strong

positive linear relationship between the variables  $(x, y)$ . Values of  $R$  close to zero indicate  $x$  and  $y$  are independent.

### 4.3.3 Parameter Selection

To achieve best performance, the algorithm-specific parameters that yield the highest mean Dice metric needs to be used. To reduce bias, the traces we used for optimizing the algorithm-specific parameters were not used for the subsequent experiments. The PDP as defined in Chapter 3 has 5 major parameters  $\gamma, \Delta\rho, \Delta\theta, \alpha, \beta$ . We set the smoothing parameter ( $\gamma$ ) to  $5^\circ$ , the radial sampling interval ( $\Delta\rho$ ) to 0.5 pixels and set the parameter that measures the importance of the gradient strength ( $\beta$ ) to be dependent on the importance of the polar variance image ( $\alpha$ ) by the equation  $\beta = 1 - \alpha$ . The range of  $\alpha$  was from 0.3 to 0.6 in 0.1 increments. The range of angular sampling interval ( $\Delta\theta$ ) was from 0.4 to 1.1 in 0.1 increments. The algorithm-specific parameters of  $\alpha = 0.4$  and  $\Delta\theta = 0.8$  yielded the highest mean Dice.

ALCT identifies 3 major parameters  $\rho, \sigma, \nu$ . According to [81], a high torsion regularization ( $\nu$ ) forces the curve to stay within a plane; since we are working with 2D images we set  $\nu = 0$ . For finding the optimum curvature regularization ( $\sigma$ ) we set the length regularization to zero ( $\rho = 0$ ), and vary  $\sigma$  from  $10^{-4}$  to  $10^4$  in  $10^{0.1}$  increments. Given the optimum  $\sigma$ , we vary the length regularization from 0 to 1 in 0.025 increments. The algorithm-specific parameters of  $\sigma = 10^{2.6}$  and  $\rho = 0.35$  yielded the highest mean Dice.

#### 4.4 Results

Table 4.1 shows the results of the Dice analysis (mean and standard deviation based on a total of 175 images) between the physicians. The percent overlap between the traces (which is in the mid to high 80s) reflects the variability between the physicians and serves as reference for evaluating the performance of the semi-automated algorithms.

Table 4.1 Inter-physician manual tracing performance. This table shows the overlap between different trained physicians using the tracing protocol (described in the manual tracing protocol section) to manually trace the 4CH RV throughout the cardiac cycle.

Manual Tracing	Manual Tracing		
	Physician1	Physician2	Physician3
	$\mu \pm \sigma$	$\mu \pm \sigma$	$\mu \pm \sigma$
Physician1	-	$0.8707 \pm 0.0561$	$0.8592 \pm 0.0526$
Physician2	$0.8707 \pm 0.0561$	-	$0.8562 \pm 0.0544$
Physician3	$0.8592 \pm 0.0526$	$0.8562 \pm 0.0544$	-

Table 4.2 shows the results of the Dice between the semi-automated algorithms and the physicians' manual traces. This metric gives insight as to which free wall outlining algorithm (PDP, ALCT or Dijkstra) provided a better match with the physicians' traces. The first column of Table 4.2 shows which physician selected the landmarks, each physician selected 7 landmarks per patient. The second column shows whether the mask used to calculate the Dice is the RV (BP + trabeculae) or the BP. The third column of Table 4.2 denotes the algorithm used for

outlining the free wall. Note that although all Dice values are within physician variability, the PDP consistently outperforms the ALCT and Dijkstra algorithms. When comparing the mutual overlap between the physicians' manual traces and the RV or BP semi-automated masks, we can see that physician 1 has a better overlap with the RV; meanwhile for physicians' 2 and 3 have a higher Dice with the BP. This means that the traces from physician 1 included more trabeculae, while physicians 2 and 3 tended to exclude more trabeculae.

Table 4.2 Comparing physician manual tracing to semi-automated tracing (RV and BP) using physician landmarks.

Landmark Selection	Segmentation	Free Wall	Manual Tracing		
			Physician1	Physician2	Physician3
			$\mu \pm \sigma$	$\mu \pm \sigma$	$\mu \pm \sigma$
Physician1	RV	PDP	0.8970 $\pm$ 0.0418	0.8639 $\pm$ 0.0723	0.8413 $\pm$ 0.0580
		ALCT	0.8912 $\pm$ 0.0493	0.8691 $\pm$ 0.0667	0.8465 $\pm$ 0.0589
		Dijkstra	0.8879 $\pm$ 0.0392	0.8657 $\pm$ 0.0629	0.8418 $\pm$ 0.0554
	BP	PDP	0.8614 $\pm$ 0.0549	0.8835 $\pm$ 0.0463	0.8690 $\pm$ 0.0477
		ALCT	0.8475 $\pm$ 0.0636	0.8784 $\pm$ 0.0533	0.8616 $\pm$ 0.0596
		Dijkstra	0.8516 $\pm$ 0.0527	0.8790 $\pm$ 0.0442	0.8626 $\pm$ 0.0507
Physician2	RV	PDP	0.8953 $\pm$ 0.0434	0.8676 $\pm$ 0.0717	0.8335 $\pm$ 0.0601
		ALCT	0.8884 $\pm$ 0.0539	0.8712 $\pm$ 0.0711	0.8372 $\pm$ 0.0632
		Dijkstra	0.8777 $\pm$ 0.0496	0.8613 $\pm$ 0.0701	0.8254 $\pm$ 0.0615
	BP	PDP	0.8638 $\pm$ 0.0543	0.8874 $\pm$ 0.0452	0.8623 $\pm$ 0.0469

		ALCT	$0.8508 \pm 0.0658$	$0.8810 \pm 0.0562$	$0.8554 \pm 0.0592$
		Dijkstra	$0.8499 \pm 0.0599$	$0.8778 \pm 0.0523$	$0.8529 \pm 0.0542$
<b>Physician3</b>	RV	PDP	$0.8969 \pm 0.0410$	$0.8699 \pm 0.0706$	$0.8372 \pm 0.0514$
		ALCT	$0.8860 \pm 0.0577$	$0.8691 \pm 0.0711$	$0.8378 \pm 0.0606$
		Dijkstra	$0.8880 \pm 0.0444$	$0.8706 \pm 0.0671$	$0.8363 \pm 0.0542$
	BP	PDP	$0.8615 \pm 0.0536$	$0.8872 \pm 0.0452$	$0.8628 \pm 0.0423$
		ALCT	$0.8451 \pm 0.0683$	$0.8772 \pm 0.0584$	$0.8526 \pm 0.0635$
		Dijkstra	$0.8559 \pm 0.0547$	$0.8848 \pm 0.0464$	$0.8592 \pm 0.0488$

The next step was to measure the robustness of the different free wall outlining techniques to landmark selection. Table 4.3a shows the Dice when looking only at the RV semi-automated masks; Table 4.3b shows the Dice when looking only at the BP semi-automated masks. Note that although the Dice values are in the mid to high 90s, the PDP consistently outperforms the ALCT and Dijkstra algorithms.

Table 4.3 Inter-physician performance using semi-automated techniques to do the tracing. The tables calculates the mutual overlap when comparing (a) semi-automated RV masks and (b) semi-automated blood pool (BP) masks.

<b>a</b>	<b>Free Wall</b>	<b>Landmark Selection</b>		
		<b>Physician1</b>	<b>Physician2</b>	<b>Physician3</b>
		$\mu \pm \sigma$	$\mu \pm \sigma$	$\mu \pm \sigma$
<b>Physician1</b>	PDP	-	$0.9629 \pm 0.0212$	$0.9661 \pm 0.0218$

	ALCT	-	$0.9569 \pm 0.0396$	$0.9636 \pm 0.0346$
	Dijkstra	-	$0.9488 \pm 0.0315$	$0.9627 \pm 0.0261$
<b>Physician2</b>	PDP	$0.9629 \pm 0.0212$	-	$0.9670 \pm 0.0244$
	ALCT	$0.9569 \pm 0.0396$	-	$0.9633 \pm 0.0355$
	Dijkstra	$0.9488 \pm 0.0315$	-	$0.9595 \pm 0.0303$
<b>Physician3</b>	PDP	$0.9661 \pm 0.0218$	$0.9670 \pm 0.0244$	-
	ALCT	$0.9636 \pm 0.0346$	$0.9633 \pm 0.0355$	-
	Dijkstra	$0.9627 \pm 0.0261$	$0.9595 \pm 0.0330$	-

<b>b</b>	<b>Landmark Selection</b>	<b>Landmark Selection</b>		
		<b>Physician1</b>	<b>Physician2</b>	<b>Physician3</b>
		$\mu \pm \sigma$	$\mu \pm \sigma$	$\mu \pm \sigma$
<b>Physician1</b>	PDP	-	$0.9674 \pm 0.0190$	$0.9704 \pm 0.0235$
	ALCT	-	$0.9605 \pm 0.0375$	$0.9653 \pm 0.0342$
	Dijkstra	-	$0.9531 \pm 0.0300$	$0.9624 \pm 0.0271$
<b>Physician2</b>	PDP	$0.9674 \pm 0.0190$	-	$0.9708 \pm 0.0261$
	ALCT	$0.9605 \pm 0.0375$	-	$0.9665 \pm 0.0362$
	Dijkstra	$0.9531 \pm 0.0300$	-	$0.9635 \pm 0.0338$
<b>Physician3</b>	PDP	$0.9704 \pm 0.0235$	$0.9708 \pm 0.0261$	-
	ALCT	$0.9653 \pm 0.0342$	$0.9665 \pm 0.0362$	-

	Dijkstra	$0.9624 \pm 0.0271$	$0.9635 \pm 0.0338$	-
--	----------	---------------------	---------------------	---

PDP, polar dynamic programming; ALCT, a\* using length, curvature and torsion penalties;

In Table 4.2, we showed that the semi-automatic techniques generated Dice values that were within human variability. Therefore, we wanted to see if this translates to similar FAC values. The FAC analysis for Table 4.4 and 4.5 was done using the semi-automated segmentation masks generated by the PDP free wall technique. Table 4.4 shows the mean FAC and standard deviation of the three manual traces, the RV and BP FAC values. The results show that the RV and BP FAC have lower standard deviation than the FAC derived from manual tracers. In general, the FAC calculated from the BP is similar to the average manual traces; this is expected since 2 out of the 3 tracers excluded the trabeculae region as part of the RV. The BP FAC is generally higher than the RV FAC. The reason may be that in the ES frame a large percent of the RV is trabeculae and when excluded, the area in the ES frame is lower, resulting in a higher FAC.

Table 4.4 Comparison of FAC derived from three different measurements; manual traces, RV and BP.

Segmentation	Free Wall	Patient						
		1	2	3	4	5	6	7
		$\mu \pm \sigma$						
Manual Trace	-	0.4977 ± 0.0474	0.4823 ± 0.0459	0.5105 ± 0.0520	0.2655 ± 0.0143	0.5435 ± 0.0192	0.4365 ± 0.0574	0.5269 ± 0.0848
RV	PDP	0.4143 ± 0.0134	0.3622 ± 0.0251	0.3706 ± 0.0268	0.2152 ± 0.0103	0.4485 ± 0.0100	0.2470 ± 0.0445	0.3303 ± 0.0277
BP	PDP	0.4943 ± 0.0079	0.4424 ± 0.0150	0.5207 ± 0.0221	0.2394 ± 0.0133	0.5195 ± 0.0083	0.3107 ± 0.0324	0.5355 ± 0.0251

Finally, we use R and confidence intervals from FAC measurements to measure the linear relationship and determine whether the relationship is statistically significant. The statistical analysis was performed comparing the inter-physicians' FAC variance (Table 4.5a), the semi-automated segmentation focusing on BP FAC with the physicians' FAC based on their manual tracing (Table 4.5b), and the semi-automated segmentation focusing on BP FAC among themselves (Table 4.5c). Table 4.5a shows that the correlation coefficients range from 0.9377 to 0.7364 and only the FAC between physicians 1 and 2 turns out to have a p value > 0.05. Table 4.5b shows that the correlation coefficients range from 0.7886 to 0.9238 with p values < 0.05. Finally, Table 4.5c shows the overlap between the semi-automated technique using different physicians' landmarks. Note that all the R values are higher than 0.95 and their respective p values < 0.01.

Table 4.5 R score and P value using FAC. (a) Inter-physician manual tracing performance, (b) physician manual tracing to semi-automated tracing (RV and BP) using physician landmarks, and (c) inter-physician performance using semi-automated technique to do the tracing.

<b>a</b>	<b>Manual Outlining</b>		
	<b>Physician1</b>	<b>Physician2</b>	<b>Physician3</b>
	R	R	R
<b>Physician1</b>	-	0.7364*	0.9377*
<b>Physician2</b>	0.7364*	-	0.7809*
<b>Physician3</b>	0.9377*	0.7809*	-

<b>b</b>	<b>Manual Outlining</b>		
	<b>Physician1</b>	<b>Physician2</b>	<b>Physician3</b>
	R	R	R
<b>Physician1</b>	0.8382*	0.8321*	0.8143*
<b>Physician2</b>	0.9238*	0.8225*	0.9114*
<b>Physician3</b>	0.8692*	0.7886*	0.8680*

<b>C</b>	<b>Landmark Selection</b>		
	<b>Physician1</b>	<b>Physician2</b>	<b>Physician3</b>
	R	R	R
<b>Physician1</b>	-	0.9745✓	0.9740✓
<b>Physician2</b>	0.9745✓	-	0.9843✓
<b>Physician3</b>	0.9740✓	0.9843✓	-

\* p-value < 0.1, †p-value < 0.05, ★p-value < 0.01, ✓p-value < 0.001.

#### 4.5 Analysis

Understanding the functional properties of the cardiac chambers is important for diagnosing both LV and RV related cardiovascular disorders. However, over the years most of the attention has been on the LV, in part due to the lack of optimal imaging tools for looking at the RV [3]. With the advent of CMR, it is now possible to quantify the function of both the LV and RV providing new capabilities related to the latter. Most of the analysis tools available in the clinic are still focused on the LV. The algorithm presented above was developed to provide an easy-to-use tool for the functional analysis of the RV. The algorithm was designed to segment the RV in 4CH views with the option to include or exclude the trabeculae to accommodate for different methods for RV functional analysis [4].

The results described previously show that the proposed technique yields results that are within human variability (Table 4.2), while also being robust to physicians' landmarks (Table 4.3). Using as measurement Dice, PDP outperformed Dijkstra and ALCT in the delineation of the free wall. When the analysis turned to a more clinical measure, FAC BP yielded results similar to the physicians' traces (Table 4.4, Table 4.5b) because two out of the three tracers excluded the

trabeculae from the RV trace. We also show that FACs are robust to the physicians' landmarks (Table 4.5c).

One of the main reasons for the discrepancy between the manual outlines (Table 4.1) is the trabeculae. For instance, if the Dice metric is calculated only on the ED frame, the values are in the low 90s. Yet the Dice metric calculated throughout the cardiac cycle yields values in the mid to high 80s; thus the increase in variability stems from trabeculae found in the systolic portion of the cardiac cycle. The increase in variability stems from trabeculae found in the ES frame. The question whether the trabeculae should or should not be included as part of the physicians' trace is still up for debate [4]. An example of the outline variation can be seen in Figure 4.4. One of the physicians included almost no trabeculae while another physician included most of the trabeculae. These discrepancies lead to the high variability seen throughout the study (i.e., Table 4.1, Table 4.4 and Table 4.5a).

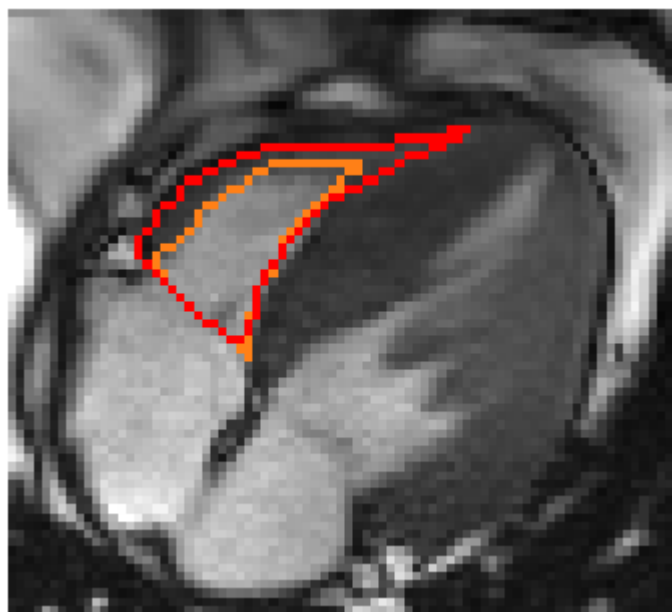


Figure 4.4 ES physicians' trace. Trace from physician 1 (in red) includes most of the trabeculae, while the other trace (orange) excludes most of the trabeculae.

Looking at Table 4.4 we can see that the patients who have mean BP FAC outside a standard deviation of the mean manual traces FAC are patients 2 and 6. The main problem with patient 2 was the selection of the ES frame. The area from the manual outlines consistently identify frame 13 as the ES frame, whereas the physicians visually identified the ES frame in the 9-10 range. When the error between the selected ES frame and the real ES frame is more than 2 frames, the performance, as measured by FAC will suffer. Patient 6 shows the importance of selecting the correct landmark locations. The difference in FAC for this patient can be attributed to the landmark selection, in this particular case, the location of the septal portion of the TV, show in Figure 4.5. An incorrect landmark selection may affect the area of the ventricle in the ED or ES frame and consequently affect the final FAC value.

Another important aspect of this proposed technique is the time component. The proposed method using PDP for outlining the free wall, took on average 2 minutes per patient, while manual tracing took the physicians approximately 15 minutes per patient.

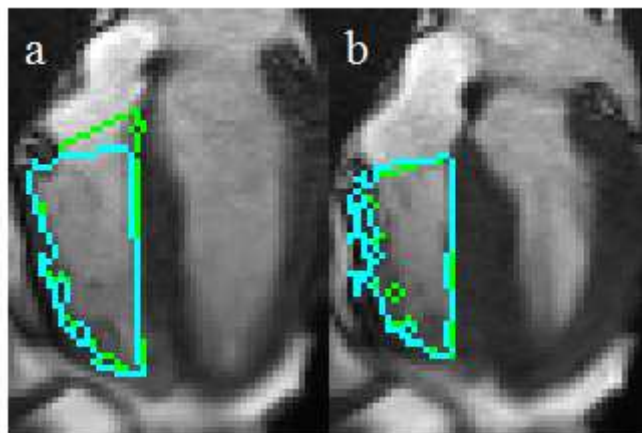


Figure 4.5 BP FAC for different user-selected landmarks in the (a) ED and (b) ES frame. The outline in green yielded the highest BP FAC, while the outline in cyan yielded the lowest BP FAC.

## 4.6 Conclusion

We developed an algorithm based on landmark selection and PDP for the semi-automatic segmentation of the RV in 4CH cine CMR images. The results show that the proposed technique matches the physicians' manual traces and reduces variability among tracers. The results indicate that the algorithm can optimize the workflow associated with the analysis of the RV by reducing the time required for the RV segmentation. We showed that BP FAC matches the results derived from the manual tracers. Future work may use the 4CH segmented RV to measure the free wall motion in the RV similar to the work done by Nagel in the LV [86].

## **5 SAX RV SEGMENTATION USING DYNAMIC PROGRAMMING**

In chapter 3 we describe a PDP technique able to segment non-circular objects, such as the RV in a SAX view (Figure 3.6e). In chapter 4 we described a technique to segment the RV in 4CH view. This exploratory chapter focuses on incorporating the PDP algorithm with the 4CH RV segmentation to segment the RV in the SAX view.

### **5.1 Algorithm Description**

The proposed technique consists of the following steps: (1) 4CH semi-automatic segmentation of the RV; (2) geometric relationship between SAX and 4CH views; (3) 4CH segmentation of the LV; (4) identification of the SAX slices as basal, mid-ventricular or apical; (5) automatic identification of the ROI for each slice; (6) transformation of the 4CH RV and LV masks into the SAX view; and finally the segmentation of the (7) LV and (8) RV. These steps are outlined in Figure 5.1. 4CH semi-automatic segmentation of the RV is explained in Chapter 3.

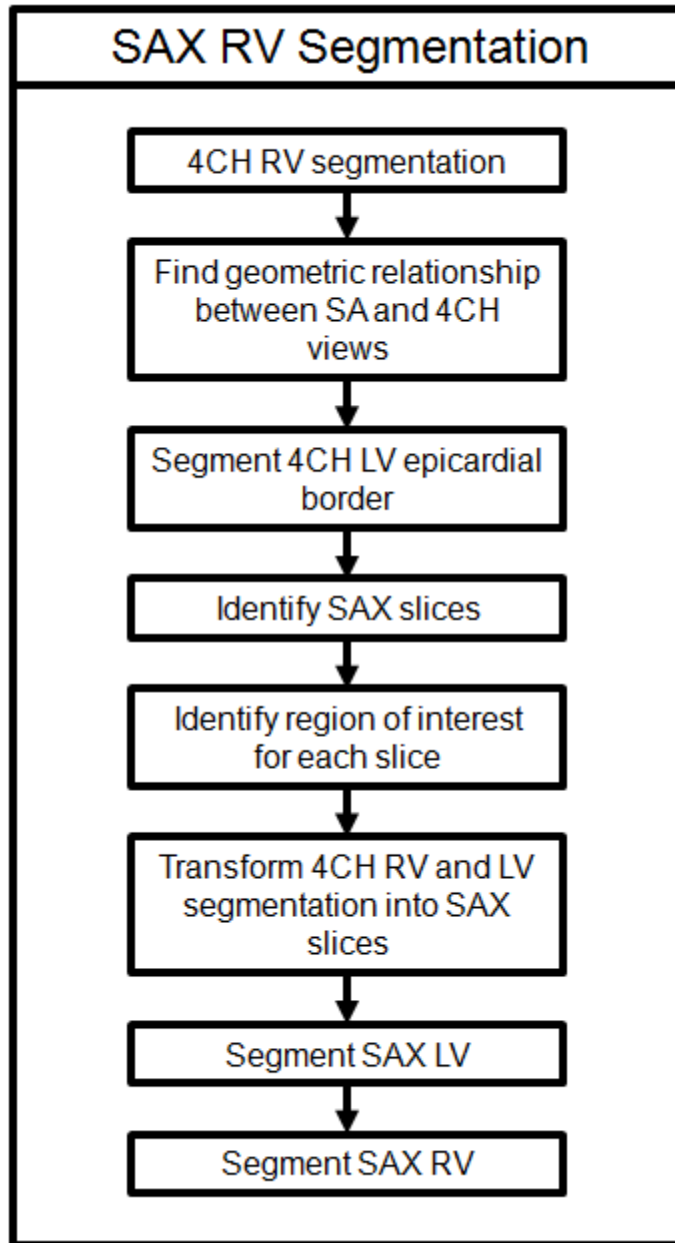


Figure 5.1 SAX RV Segmentation Flowchart.

### 5.1.1 Find geometric relationship between SAX and 4CH views

In section 1.1.2 we explained how to create 2D MR images. These acquired MR images have headers that include the subject's position within the patient coordinate system (PCS)<sup>25</sup> [87]. The image header contains:

1. Image position ( $P_{xyz}$ ): location in 3D space of the first transmitted pixel.
2. Pixel spacing ( $\Delta x, \Delta y$ ): a vector containing the physical distance between adjacent vertical and horizontal pixels. The distance is measured in millimeters.
3. Image orientation ( $X_{xyz}, Y_{xyz}$ ): the direction cosines of the first row and column with respect to the patient.
4. Slice thickness ( $\Delta z$ ): nominal slice thickness. The thickness is measured in millimeters.

Given the above information we create a rotation matrix ( $M_{rot}$ ) that rotates the 2D image from the image plane to PCS.

$$M_{rot} = \begin{bmatrix} X_x \Delta x & Y_x \Delta y & 0 & P_x \\ X_y \Delta x & Y_y \Delta y & 0 & P_y \\ X_z \Delta x & Y_z \Delta y & 0 & P_z \\ 0 & 0 & 0 & 1 \end{bmatrix} \quad (5.1)$$

To make  $M_{rot}$  invertible we fill the third column with:

$$Z_{xyz} = X_{xyz} \times Y_{xyz} \quad (5.2)$$

where  $\times$  is the cross product. This makes (5.1) become:

---

<sup>25</sup> 3D system representing the location of the patient with respect to the imaging modality. The x-axis increases to the left hand side of the patient, the y-axis increases to the posterior side of the patient and the z-axis increases going to the head of the patient.

$$M_{rot} = \begin{bmatrix} X_x \Delta x & Y_x \Delta y & Z_x \Delta z & P_x \\ X_y \Delta x & Y_y \Delta y & Z_y \Delta z & P_y \\ X_z \Delta x & Y_z \Delta y & Z_z \Delta z & P_z \\ 0 & 0 & 0 & 1 \end{bmatrix} \quad (5.3)$$

Let's define  $M_{rot}^{4CH}$  and  $M_{rot}^{SA}$  as the rotation matrices that takes the data from the 4CH image plane and SAX image planes, respectively, and rotate them to the PCS. Using right hand side matrix multiplication, we can define the rotations matrices that go from the SAX view to the 4CH view as

$$M_{SA-4CH} = (M_{rot}^{4CH})^{-1} M_{rot}^{SA} \quad (5.4)$$

To go from the 4CH view to the SAX view just invert (5.4).

### 5.1.2 Segment 4CH LV epicardial border

The epicardial border of the LV in 4CH view is shown in Figure 5.2. Note that inside the epicardial border there are bright pixels (corresponding to the BP of the LV) and pixels with similar intensity to the trabeculae in the RV. To find the LV epicardial border we look for intensities that are similar to those of the RV (both BP or trabeculae) and are left lateral to the RV.

Even if the thresholding technique includes regions that are not part of the epicardial border, the results will be fine-tuned in the “segment SAX LV” section.

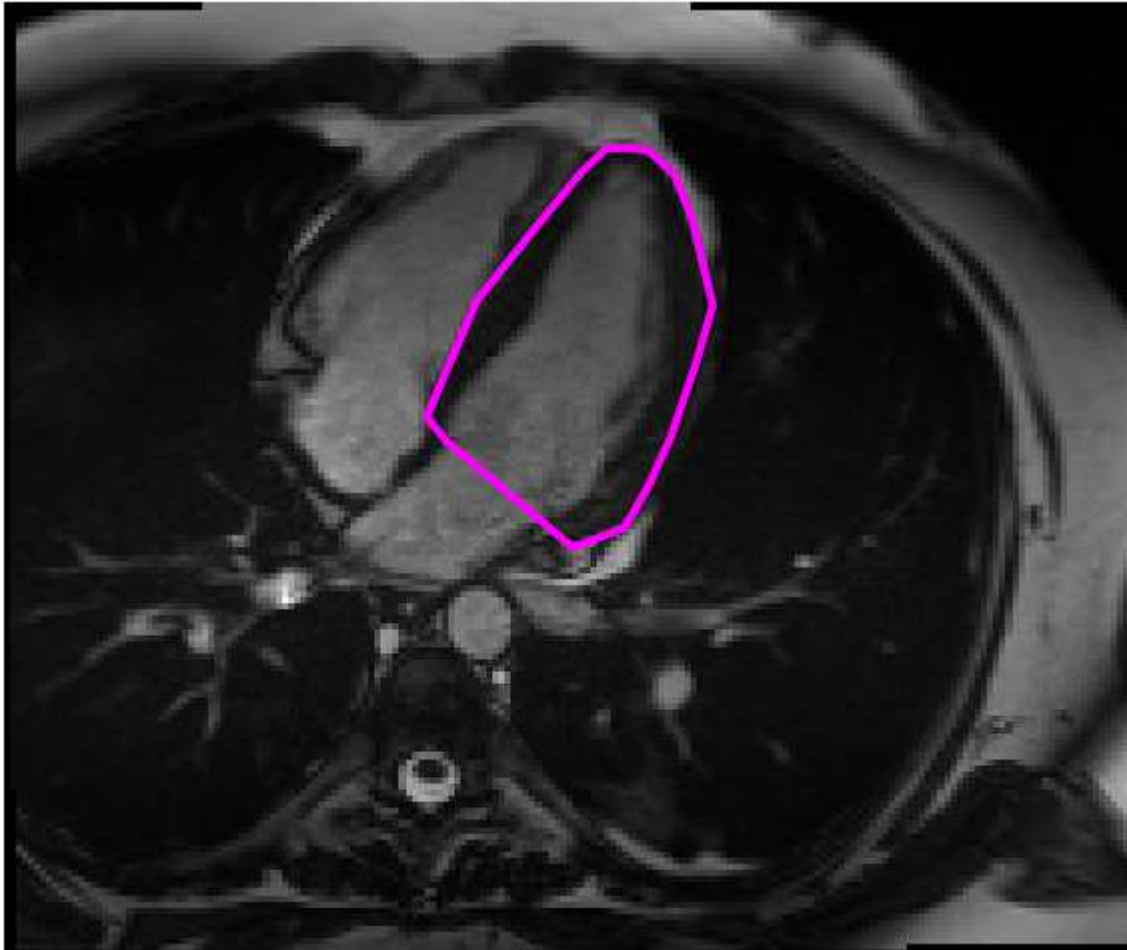


Figure 5.2 LV epicardial border (magenta outline).

### 5.1.3 Identify SAX Slices

Consider the array containing the SAX slices as  $I(x, y, z, n)$ , where  $n$  is the frame number ( $x, y$ ) are the coordinates within the given frame and  $z$  is the SAX slice index. There is a need to identify the SAX slices as different parts of the RV have different properties (e.g., RV being divided in two regions at the basal slices). The first step is to take the SAX slices and transform them to the 4CH view using (5.4). The SAX slices that overlap with the 4CH segmented RV area will be categorized into three classes: basal, mid-RV and apical slices (as shown in Figure

5.3). Going from proximal to distal, the most proximal third of the slices will be classified as the basal slices; the next third will be classified as mid-RV slices; the last third of the slices will be the classified as apical slices.

Aside from the general classification of the slices we also need a representative slice to generate the RV model that will be used throughout the SAX RV segmentation process. The RV representative slice is the most proximal mid-RV slice. We use this slice because it is not part of the basal region, has an area comparable to the basal slices and contains fewer trabeculae than the apical slices.

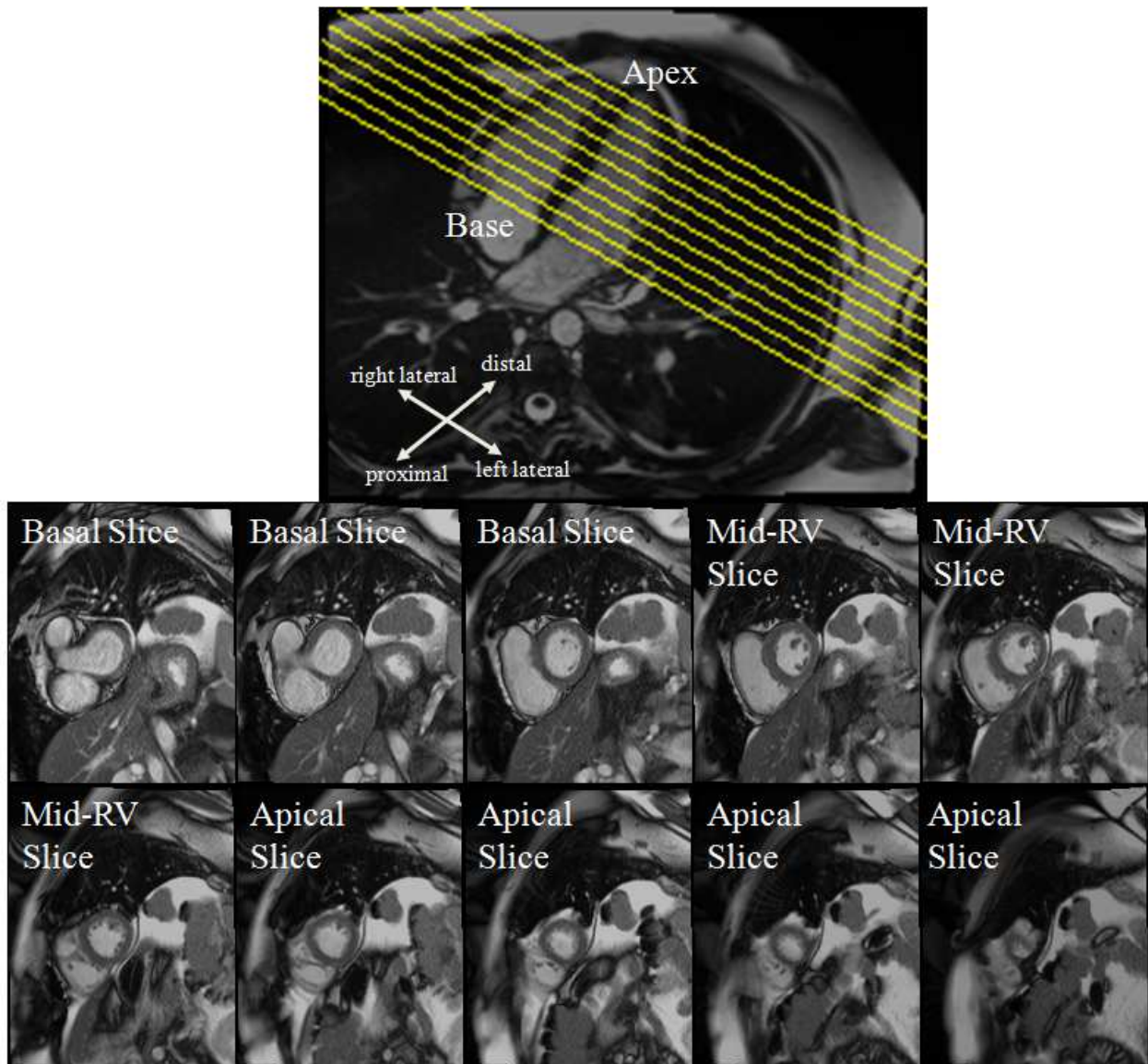


Figure 5.3 Overlap between SAX and 4CH views. The yellow lines show how the SAX views overlap with the 4CH view. CMR images of SAX views are shown from the base (upper left from the SAX stacks) all the way to the apex (lower right from the SAX stacks).

#### 5.1.4 Transform 4CH RV and LV Segmentation into SAX Slices

To transform 4CH RV and LV segmentation masks to the SAX view we use the inverse of (5.4). This technique helps reduce the ROI by giving a rough estimate of the LV and RV in SAX views. An example is shown on Figure 5.4.

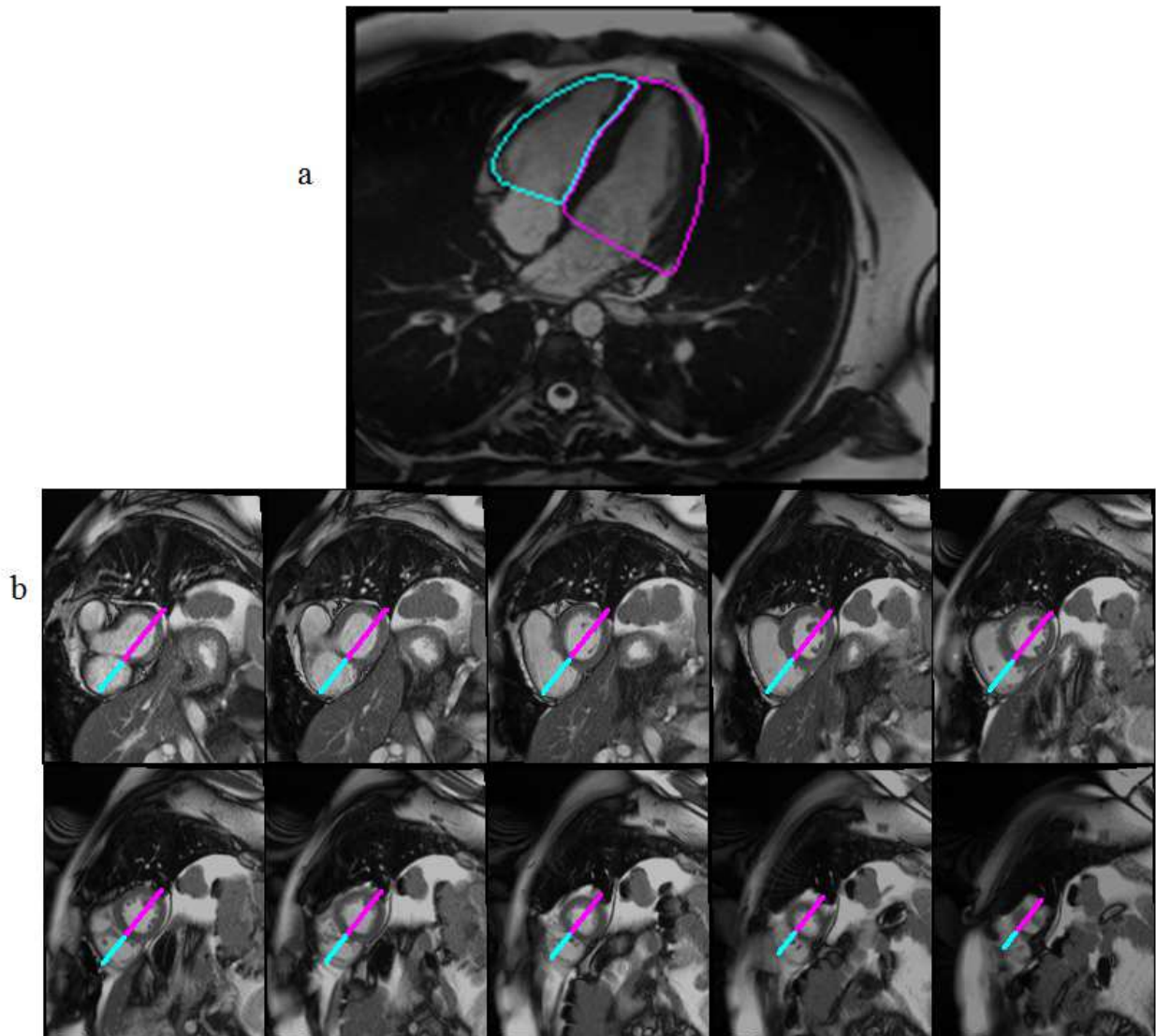


Figure 5.4 4CH RV (cyan) and LV segmentation (magenta) (a) displayed onto the 4CH view. (b) The 4CH segmentations are rotated into SAX slices and displayed as lines each of the SAX slices. Lines in SAX slices have been dilated for viewing purposes.

#### 5.1.5 Identify ROI for each SAX Slice

To automatically identify the ROI within each slice, the algorithm looks for high standard deviation of pixel intensities throughout the cardiac cycle. The standard deviation image is calculated using (4.1). To get an initial binary mask ( $m(x, y)$ ), the standard deviation image is thresholded using k-means++. Given an initial mask, we calculate the vertical profile as:

$$h(y) = \int m(x, y) dx \quad (5.5)$$

Given the vertical profile, the technique looks for the peak value ( $\tau_{vert}$ ). Then it thresholds  $h(y)$  to find values greater than  $0.1\tau_{vert}$ . The row-wise extension of the ROI ( $y_{max}, y_{min}$ ) is the largest connected component of the thresholded  $h(y)$ .

$$h(x) = \int_{y_{min}}^{y_{max}} m(x, y) dy \quad (5.6)$$

Given the horizontal profile, the technique looks for the peak value ( $\tau_{horz}$ ). Then it thresholds  $h(x)$  to find values greater than  $0.1\tau_{horz}$ . The technique will keep all connected components with an area greater than 25 percent of the area of the largest connected component. The 25 percent threshold is used because in some cases the binary mask associated with the motion of the free wall is not connected to the binary mask associated with the motion of the myocardium. The column-wise extension of the ROI ( $x_{max}, x_{min}$ ) are the minimum and maximum column of the connected components. Subsequent analysis will focus on pixels that reside inside the ROI.

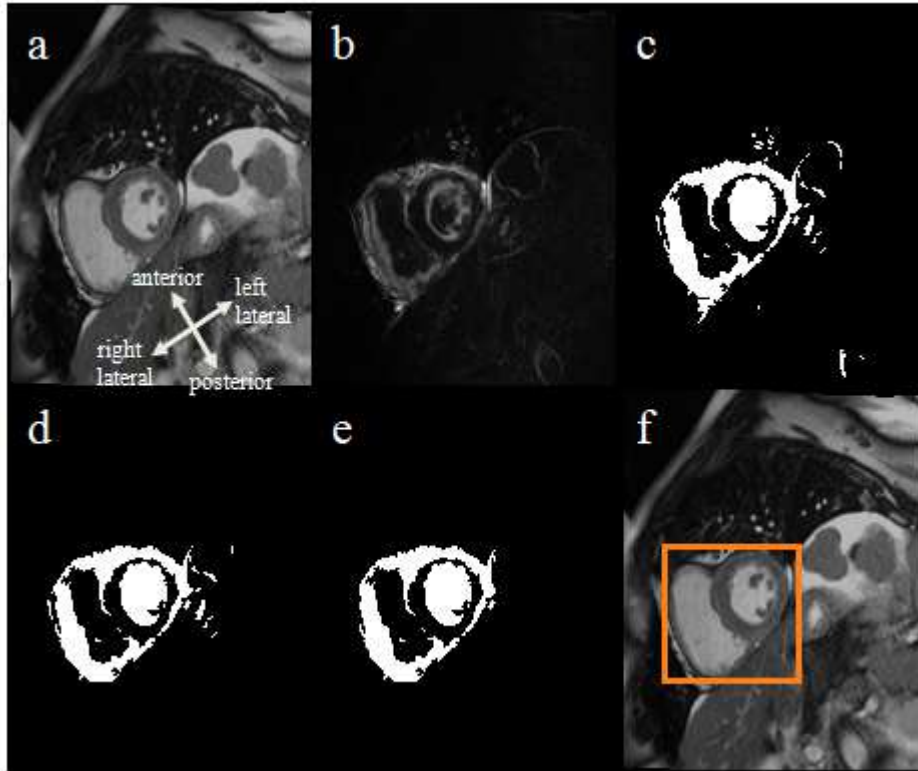


Figure 5.5 Identifying SAX ROI. (a) An image in the SAX view; (b) standard deviation image for the given slice; (c) thresholded standard deviation image; (d) ROI reduction using horizontal profiling; (e) ROI reduction using vertical profiling and (f) final ROI used for LV and RV segmentation.

## 5.1.6 Segment SAX LV

### 5.1.6.1 Segment SAX LV Endocardial Border

To segment the SAX LV endocardium border, we first identify BP regions in the SAX slice. For the representative slice, this is done by clustering the image using k-means++ with  $k = 3$  where the BP and fat pixels contain the highest mean intensity. The pixels with the lowest mean intensity are associated with air, either from the lungs or outside the patient. For the other slices we use the statistics calculated from the LV endocardial border in the representative slice to identify BP regions. The BP regions (shown in Figure 5.6b) associated with the LV

endocardium are those which are adjacent to the 4CH LV segmentation rotated into the SAX view (magenta line in Figure 5.6c).

Specifically, let's define  $l_{LV}$  and  $(x_{LV}, y_{LV})$  as the length and centroid of the 4CH LV segmentation, respectively, rotated into the SAX view. Any BP region whose centroid is closer than  $l_{LV}/4$  to  $(x_{LV}, y_{LV})$  will be associated with the LV endocardium (Figure 5.6d). These regions are joined by applying a convex hull [61] similar to Lu *et al.* [62] (Figure 5.6e). Any pixel whose intensity is larger than the 99<sup>th</sup> percentile of the LV endocardial border pixels, is identified as a fat pixel.

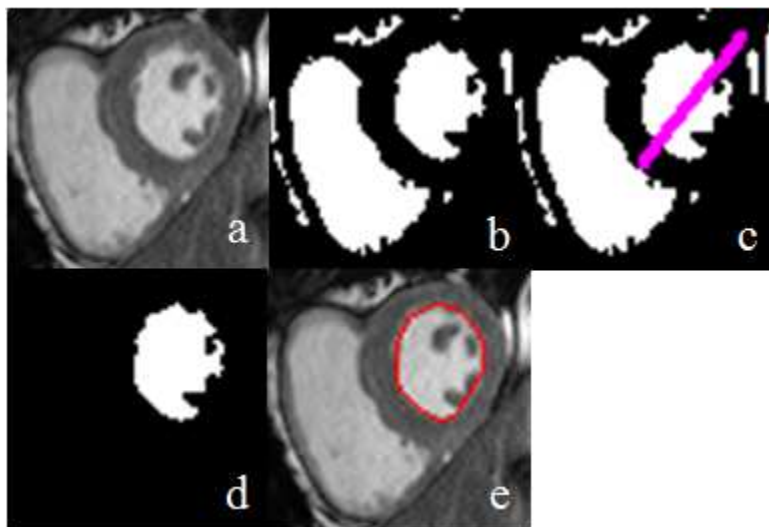


Figure 5.6 Segmentation of LV endocardial border. (a) cropped SAX view of representative slice; (b) BP regions; (c) 4CH epicardial border of LV on SAX view; (d) LV BP region and (e) LV endocardial border.

### 5.1.6.2 Segment SAX LV Epicardial Border

Given the endocardial border of the LV, we outline the epicardial border using PDP, similar to the work of Lu *et al.* [61], and Huang *et al.* [63]. The origin used for segmenting the SAX LV epicardial border is the centroid of the BP regions associated with the SAX LV endocardial

border (described in section 5.1.6.1) and the cost function is based on the edge strength of  $I(x, y, z, n)$  with a few modifications. For example, we know that there is a high gradient region just outside of the epicardium therefore any edge strength adjacent to the epicardium region will be set to 0. We also know that the epicardial border should not include BP regions not associated with the LV endocardial border (e.g., SAX LV BP), therefore BP regions outside the endocardial border will be given a high cost value (i.e., a fake gradient). We also know that the endocardial border should not include any air pixels; therefore, a high cost value will be given to air pixels (i.e., lowest intensity cluster in the image) as well. With these modifications we run PDP as defined in Chapter 3. Note that since the LV is a circular object, we do not look for convex regions (i.e., by skipping the algorithm described in section 3.1.5) and set the algorithm-specific parameters as follows:  $\Delta\theta = 3^\circ$ ,  $\alpha = 0.8$ ,  $\beta = 0.2$ .

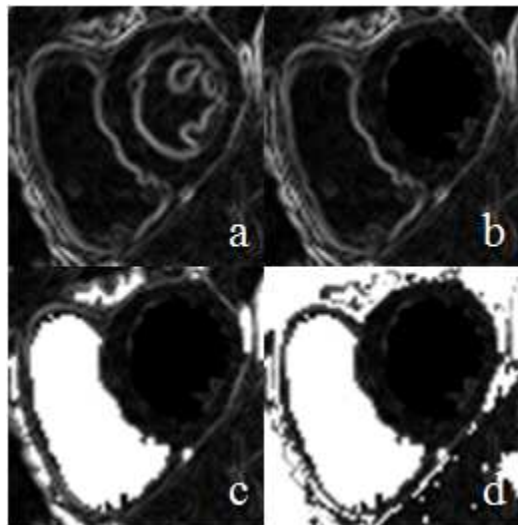


Figure 5.7 Change of cost function as explain in section 5.1.6.2.

### 5.1.7 Segment SAX RV

The 4D segmentation of the epicardial border of the SAX RV is done in the following order: first segment the SAX RV in the representative slice in the ED frame. This generates an RV model which we will use for propagating the segmentation of the RV in the ED frame throughout the different slices (i.e., spatial propagation). Once every slice has a model, the algorithm propagates the RV model for each slice throughout the cardiac cycle (i.e., temporal propagation).

If we look at the segmentation of the epicardial border of the SAX RV more generally it can be decomposed in the following steps: (1) reduce the ROI, (2) find rough segmentation (3) identify origin candidates, (4) update gradient image, (5) segment the RV using PDP, (6) join the segmentation masks that come from the different origin candidates and if necessary, (7) refine results.

The endocardial border of the RV SAX is the convex hull of the BP regions that reside inside the epicardial border of the RV SAX.

#### 5.1.7.1 Reducing the ROI

In section 5.1.5 we identified a ROI that includes the LV and the RV for each slice. For the segmentation of the RV the algorithm further reduces the ROI. This is done by removing any region that is right lateral to the 4CH RV segmentation rotated into the SAX slice and by removing any region that is left lateral to the centroid of the LV. For apical slices we also remove any region that is anterior or posterior to the epicardial border of the LV.

When performing the temporal propagation, the ROI in a given slice can be further reduced by analyzing only the morphological dilation of the convex hull of the RV and LV epicardial border for the given slice in the ED frame.

### 5.1.7.2 Finding Rough Segmentation

This section describes the process by which a SAX RV model is propagated to another slice or frame using an affine transformation followed by an additional rotation matrix. This propagation is used for identifying BP regions that will be used for generating origin candidates. For spatial propagation  $V_{model}$  is the SAX RV segmentation at the representative slice in the ED frame. For temporal propagation (i.e., throughout the cardiac cycle),  $V_{model}$  is the SAX RV segmentation in the slice being analyzed in the ED frame. Let's define  $V_{affine}$  as the affine transformation of  $V_{model}$ , where the origin is the centroid of the  $V_{model}$ .

$$V_{affine} = M_p * V_{model} \quad (5.7)$$

Here  $M_p$  is the affine transformation matrix:

$$M_p = \begin{bmatrix} s_x \cos(\alpha) & -\sin(\alpha) & 0 \\ \sin(\alpha) & s_y \cos(\alpha) & 0 \\ t_x & t_y & 1 \end{bmatrix} \quad (5.8)$$

where,

$$s_x = \frac{\max(x_{slice}) - \min(x_{slice})}{\max(x_{rep}) - \min(x_{rep})} \quad (5.9)$$

and for the mid-RV and apical slices:

$$s_y = \frac{\max(y_{slice}) - \min(y_{slice})}{\max(y_{rep}) - \min(y_{rep})} \quad (5.10)$$

Here  $(x_{slice}, y_{slice})$  and  $(x_{rep}, y_{rep})$  are the coordinates of the 4CH RV rotated into the SAX view for the slice being analyzed and the representative slice, respectively. For the basal slices, we set  $s_y = 1$ , because the movement of the RV in the anterior/posterior direction is restricted due to cartilages [88]. For the mid-RV and apical slices the translation values  $[t_x, t_y]$  measure the movement needed in order for  $V_{affine}$  to be adjacent to the LV epicardial border. For the basal slices, the translation values  $[t_x, t_y]$  measure the movement required to move the right lateral part of the  $V_{affine}$  contour to the right lateral part of the 4CH RV rotated in the SAX view. Next, we rotate  $V_{affine}$  using as origin the centroid of the LV mask:

$$V_C = M_R * V_{affine} \quad (5.11)$$

where

$$M_R = \begin{bmatrix} \cos(\alpha^*) & -\sin(\alpha^*) & 0 \\ \sin(\alpha^*) & \cos(\alpha^*) & 0 \\ 0 & 0 & 1 \end{bmatrix} \quad (5.12)$$

Note that we have not defined the rotation angles  $\alpha$  and  $\alpha^*$ . For the mid-RV and apical slices, we set  $\alpha$  and  $\alpha^*$  to the values that maximize the number of BP pixels in  $V_C$ . For the basal slices we set  $\alpha = 0$  and only optimize  $\alpha^*$ . The optimization is done using exhaustive search where  $-15^\circ \leq \alpha \leq 15^\circ$  and  $-50^\circ \leq \alpha^* \leq 0$  both with  $1^\circ$  increments.

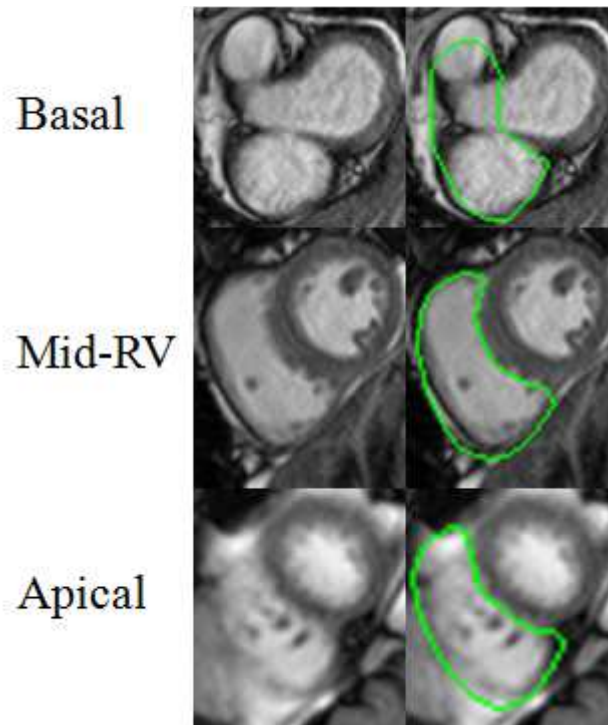


Figure 5.8 Rough segmentation for basal, mid-RV and apical slices.

### 5.1.7.3 Identifying Origin Candidates

The origin candidates used for SAX RV segmentation are based on the BP regions that form part of the rough SAX RV segmentation (explained in section 5.1.7.2). For the representative slice, the rough SAX RV segmentation is the 4CH RV segmentation rotated into the SAX slice line.

Given the BP regions, the algorithm calculates an Euclidean distance transform [89], thresholds the distance transform to include only regions that are 0.4 of the maximum distance value and then performs a morphological thinning operation [90]. The candidate origins are ordered in a descending order based on the Euclidean distance transform. Once an initial RV SAX segmentation mask is calculated (see section 5.1.7.5), the candidate origins that overlap with the mask are eliminated. This is repeated until no origins are left.

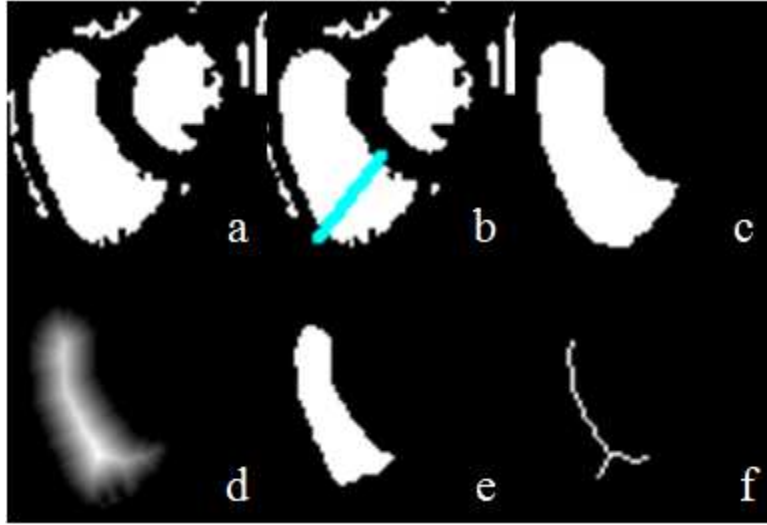


Figure 5.9 Finding candidate origins in representative slice in the ED frame. (a) BP regions, (b) 4CH RV rotated into the representative SAX slice (cyan line), (c) BP region associated with the RV, (d) distance transform of (c), (e) binary mask of distance transform and (f) candidate origins.

#### 5.1.7.4 Upgrade Gradient Image

To segment an image using PDP we need a gradient image ( $G$ ), an origin  $(x_0, y_0)$  and an intensity image ( $I$ ). The gradient image used for the technique is

$$G(x, y, z, n) = \max_{x,y} I(x, y, z, n) - I(x, y, z, n) \quad (5.13)$$

Once (5.7) is created the algorithm takes any pixel in the gradient image that falls outside the reduced ROI and set it to 0. Next the algorithm finds the coordinates of the low intensity regions in  $I(x, y, z, n)$  (e.g., air) and changes the values in  $G(x, y, z, n)$  to 0.

For mid-RV and apical slices, we also want to make sure that the left lateral side of the RV is adjacent to the right lateral side of the LV epicardial border. Therefore, we make the right lateral LV epicardial border have the maximum gradient value in (5.7). A pictorial representation of the changes incurred by the gradient image in a mid-RV slice is shown in Figure 5.10.

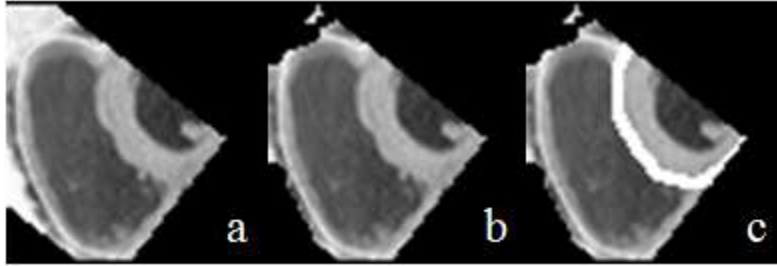


Figure 5.10 Gradient image creation. (a) Gradient image, defined by (5.7), where regions that are outside the reduced ROI are removed. (b) Setting air pixels in the gradient image to 0, and (c) high gradient value given to the right lateral portion of the LV epicardial border.

#### 5.1.7.5 Using PDP to Segment the RV

The RV is segmented using PDP as described in Chapter 3. The angular sampling interval used for segmenting the SAX RV in the mid-RV slices is:  $\Delta\theta = [3^\circ \ 2^\circ \ 1^\circ]$ , whereas for the basal and apical slices  $\Delta\theta = 3^\circ$ . For cost function (3.9), we use  $\alpha = 0.6$  and  $\beta = 0.4$ . A morphological filling operation [79] is carried out to generate a mask from the contour. For each segmentation mask created, the number of candidate origins will be reduced. The algorithm will keep generating segmentation masks until all candidate origins have been eliminated, which may result in multiple segmentation masks.

#### 5.1.7.6 Joining Segmentation Masks

The algorithm finds the area for each mask created in section 5.1.7.5 and keeps the minimum number of masks that overlap with the candidate origins. For the apical and mid-RV slices, the RV mask will be all masks that meet these criteria. For the basal slices it will keep the masks with the two largest areas.

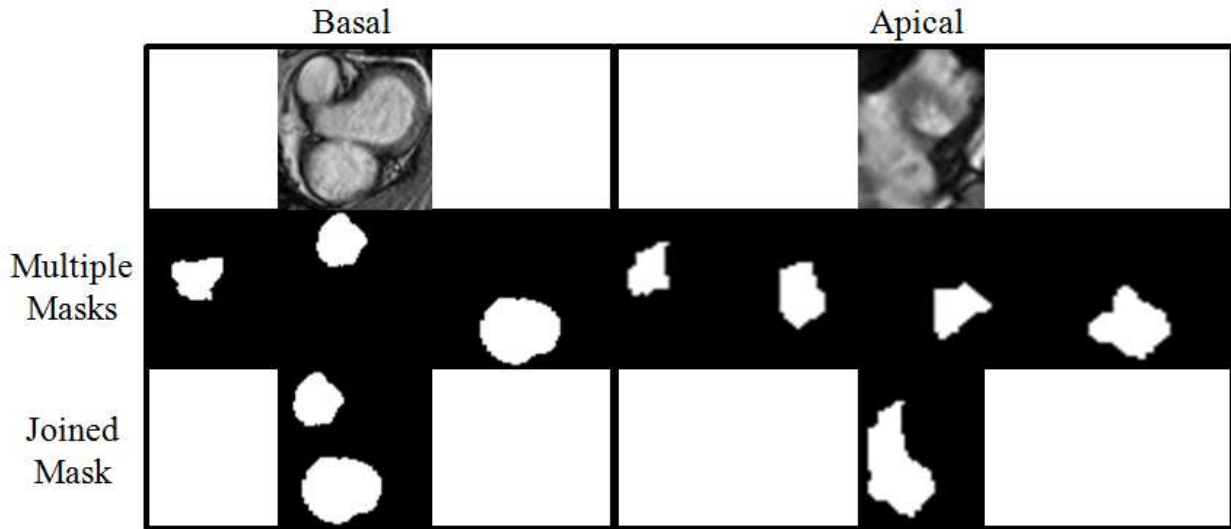


Figure 5.11 Joining segmentation masks examples. For the basal slices, the technique will only pass two masks with the largest area, while in the apical slices it will pass the number of masks that minimize the amount of overlap.

#### 5.1.7.7 Refining Segmentation Masks

If the number of connected components for the RV segmentation of the mid-RV and apical slices is more than one, the technique will join all the connected components into a single connected component using the convex hull technique. This is followed by a smoothing operation to ensure a smooth RV contour. For the basal slices the algorithm will go to each connected component and perform a smoothing operation to ensure a smooth RV contour, followed by a pixel-wise multiplication of the rough segmentation based on the affine transformation of the RV model. Regions of the RV segmentation that overlap with the LV segmentation will be removed.

## 5.2 Data and Performance Metric

### 5.2.1 Data Acquisition

Images were acquired in a Siemens 1.5T Aera scanner, using a cine SSFP sequence in the 4CH view (TR = 2.7-2.8 ms, TE = 1.16 ms, acquisition matrix = 156 x 192, FOV = 26 x 32 cm, slice thickness = 6 mm) and SAX views (TR = 2.7-2.8 ms, TE = 1.16ms, acquisition matrix = 192 x 156, FOV = 30 x 24.4 cm, slice thickness = 8 mm).

### 5.2.2 Performance Metric

The performance metric used for analysis is the Dice metric [74].

## 5.3 Results

The segmentation results for a patient are shown in Figure 5.12 and Figure 5.13. In the ED frame (Figure 5.12) the Dice metrics for the epicardial border in the mid-RV slices are in the range of high 80s to low 90s. The Dice metric in the apical slices decreases mainly due to the reduction in the area of the apical slices. A smaller area generally yields lower Dice metric values. This effect can also be seen in the ES frame where the Dice metric is consistently lower than its ED counterpart [9]. The largest discrepancy between the semi-automated and manual traces (in both ED and ES frames), as measured by Dice metric, occurs in the basal slices.

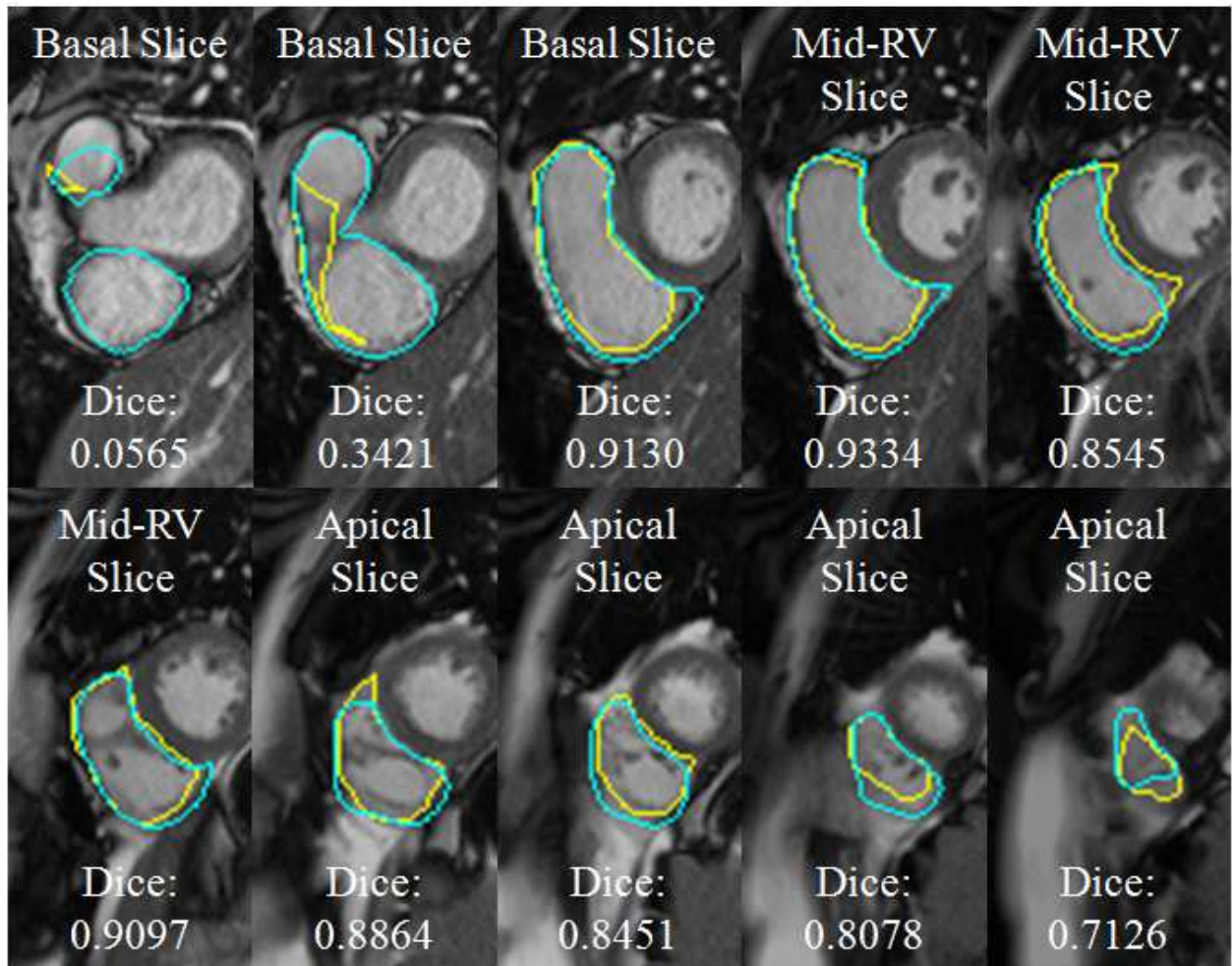


Figure 5.12 Dice metric for RV epicardial border in the ED frame. The semi-automated results are shown in cyan; manual trace in yellow.

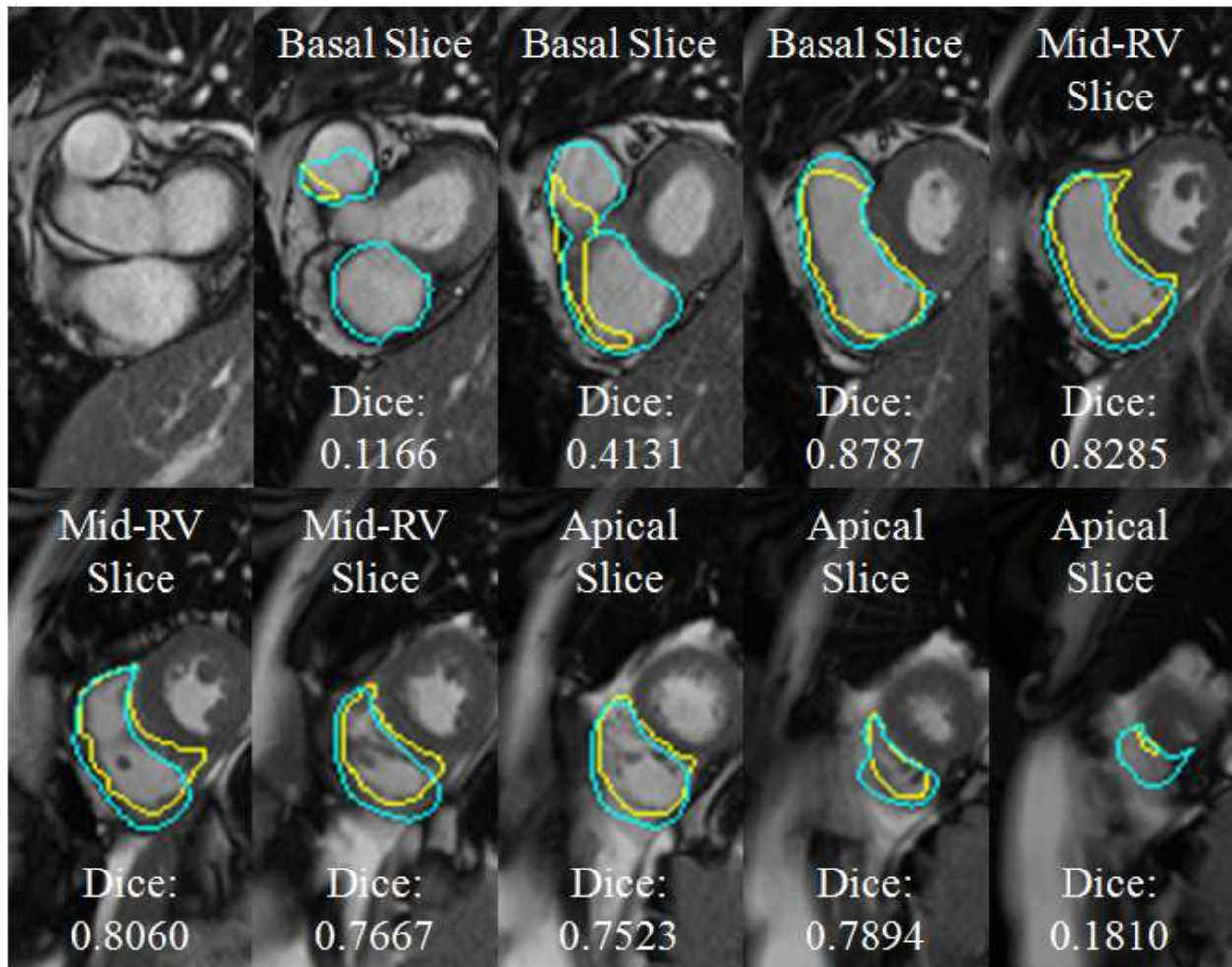


Figure 5.13 14 Dice metric for RV epicardial border in the ES frame. The semi-automated results are shown in cyan; manual trace in yellow.

#### 5.4 Analysis

The disagreement between the semi-automated technique and the manual traces in the basal slices requires more research. Based on the geometry transforms (section 5.1.1) the algorithm classifies as basal, slices where chamber being imaged is the RA. In those slices the expert traces of the RV are clearly different than the ones obtained by the semi-automatic segmentation. Incorrect classification of RA slices as basal slices is probably due to differences in breath

holding; the 4CH and SAX views are acquired in different breath holds which may lead to differences in position. To account for this discrepancy, we may need to add a correlation step to the geometry transforms to better match the 4D SAX views with the 3D 4CH views.

There are also small BP regions in the mid-RV slices that the semi-automated technique excludes, but the manual tracer includes. These regions could be added if we modify the candidate origins selection process to identify BP regions that are adjacent to the LV epicardial border. However, adding these regions may have the unintended consequence of adding BP regions that are outside the RV epicardial border just because they are adjacent to the LV epicardial border, an example is shown in Figure 5.15.

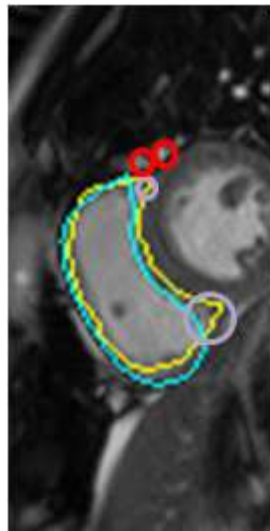


Figure 5.15 Purple circles denotes BP regions that form part of the SAX RV segmentation and are adjacent to LV epicardial border. Red circles denote BP regions that do not form part of the SAX RV segmentation but are adjacent to the LV epicardial border.

## 5.5 Conclusion and Future Work

We are developing a technique that takes user inputs for the RV in 4CH view and generates a 4D RV segmentation in a SAX view. This chapter offered exploratory analysis on the segmentation of the RV in SAX views and in future work we wish to increase the amount of patients being analyzed and as well as the number of trained physicians tracing the patients. This will allow us to develop a technique that has a Dice metric that is within user variability. For the LV this value was in the high 80s low 90s. As of today no such technique exists for SAX RV segmentation. Our technique shows promise, but requires more testing. Once a mature technique is developed, we will compare our technique with standardized RV SAX datasets such as the one used in the 2012 MICCAI RV segmentation challenge. We also plan to derive clinical metric (e.g., EF) and compare to the results obtained from experts manually tracing the RV.

The ultimate goal of the semi-automated segmentation algorithms developed as part of this dissertation is to provide unique tools for the analysis of RV function in a clinical setting.

## REFERENCES

- [1] (2016). heart. *Encyclopaedia Britannica*. Available: <http://academic.eb.com/EBchecked/topic/258344/heart>
- [2] V.H. Rigolin, P.A. Robiolio, J.S. Wilson, J.K. Harrison and T.M. Bashore, "The forgotten chamber: the importance of the right ventricle," *Catheterization and cardiovascular diagnosis*, vol. 35, no. 1, pp. 18-28, May 1995.
- [3] J. Sanz, J. Conroy and J. Narula, "Imaging of the right ventricle," *Cardiology Clinics*, vol. 30, no. 2, pp. 189-203, May 2012.
- [4] M.M. Driessen, V. J. Baggen, H.G. Freling, P.G. Pieper, A.P. van Dijk, P.A. Doevendans, R.J. Snijder, M.C. Post, F.J. Meijboom, G.T. Sieswerda, T. Leiner, T.P. Willems, "Pressure overloaded right ventricles: a multicenter study on the importance of trabeculae in RV function measured by CMR," *The International Journal of Cardiovascular Imaging*, vol. 30, no. 3, pp. 599-608, Mar. 2014.
- [5] K. Goetschalckx, F. Rademakers and J. Bogaert, "Right ventricular function by MRI," *Current Opinion in Cardiology*, vol. 25, no. 5, pp. 451-455, Sept. 2010.
- [6] A. Khalfa, D. Tani, S. Tadros, S. Madan, "Right and left-ventricular strain evaluation in repaired pediatric Tetralogy of Fallot patients using magnetic resonance tagging," *Pediatric Cardiology*, vol. 34, no. 5, pp. 1206-1211, Jun. 2013.
- [7] C.J. François, D.S. Fieno, S.M. Shors and J.P. Finn, "Left ventricular mass: manual and automatic segmentation of true fisp and flash cine MR images in dogs and pigs 1," *Radiology*, vol. 230, no. 2, pp. 389-395, Feb. 2004.
- [8] A.H. Mahnken, G. Mühlenbruch, R. Koos, S. Stanzel, P.S. Busch, M. Niethammer, R.W. Günther and J.E. Wildberger, "Automated vs. manual assessment of left ventricular function in cardiac multidetector row computer tomography: comparison with magnetic resonance imaging," *European Radiology*, vol. 16, no. 7, pp.1416-1423, Jul. 2006.
- [9] C. Petitjean, M.A. Zuluaga, W. Bai, J.N. Dacher, D. Grosgeorge, J. Caudron, S. Ruan, I.B. Ayed, M.J. Cardoso, H.S. Chen, D Jimenez-Carretero, M.J. Ledesma-Carbayo, C. Davatzikos, J. Doshi, G. Erus, O.M.O. Maier, C.M.S. Nambakhsh, Y. Ou, S. Ourselin, C.W. Peng, N.S. Peters, T.M. Peters, M. Rajchl, D. Rueckert, A. Santos, W. Shi, C.W. Wang, H. Wang and J. Yuan, "Right ventricle segmentation from cardiac MRI: a collation study," *Medical Image Analysis*, vol. 19, no. 1, pp. 187-202, Oct. 2014.
- [10] P. Radau, Y. Lu, K. Connelly, G. Paul, A. Dick and G. Wright, "Evaluation framework for algorithms segmenting short axis cardiac MRI," *The MIDAS Journal*, vol. 49, no. 6, Sept. 2009.
- [11] C. Petitjean and J.N Dacher, "A review of segmentation methods in short axis cardiac MR images," *Medical Image Analysis*, vol. 15, no. 2, pp. 169-184, Apr. 2011.
- [12] F.M. Groedel, "Roentgen cinematography and its importance in medicine," *British Medical Journal*, vol. 1 no. 2521, pp. 1003, Apr. 1909.
- [13] I. Edler and C.H. Hertz, "The user of ultrasonic reflectoscope for the continuous recording of the movement of heart walls," *Clinical Physiology and Functional imaging*, vol. 24, no. 3, pp. 118-136, May 2004.
- [14] R. Gramiak, R. Waag and W. Simon, "Cine ultrasound cardiography," *Radiology*, vol. 107, no. 1, pp. 175-180, Apr. 1973.

- [15] G.M. Pohost, "The history of cardiovascular magnetic resonance," *Cardiovascular Imaging*, vol. 1, no. 5, pp. 672-678, Feb. 2008.
- [16] T.D. Karamitsos, J.M. Francis, S. Myerson, J.B. Selvanayagam and S. Neubauer, "The role of cardiovascular magnetic resonance imaging in heart failure," *Journal of the American College of Cardiology*, vol. 54, no. 15, pp. 1407-1424, Oct. 2009.
- [17] G. Simonneau, N. Galie, L.J. Rubin, D. Langleben, W. Seeger, G. Domenighetti, S. Gibbs, D. Lebrec, R. Speich, M. Beghetti, S. Rich and A. Fishman, "Clinical classification of pulmonary hypertension," *Journal of the American College of Cardiology*, vol. 43, no. 12, pp. S5-S12, Jun. 2004.
- [18] E.K. Louie, S.S. Lin, S.I. Reynertson, B.H. Brundage, S. Levitsky and S. Stuart, "Pressure and volume loading of the right ventricle have opposite effects on left ventricular ejection fraction," *Circulation*, vol. 91, no. 3, pp. 819-824, Feb. 1995.
- [19] M.R. Bristow, L.S. Zisman, B.D. Lowes, W.T. Abraham, D.B. Badesch, B.M. Groves, N.F. Voelkel, D.M.B. Lynch and R.A. Quaife, "The pressure-overloaded right ventricle in pulmonary hypertension," *Chest*, vol. 114, no. 1, pp. 101S-106S, Jul. 1998.
- [20] (2016), *Pulmonary Hypertension Treatments*. Available: <http://www.phassociation.org/Treatments>
- [21] M. Ritchie, A.D. Waggoner, V.G. Dávila-Román, B. Barzilai, E.P. Trulock and P.R. Eisenberg, "Echocardiographic characterization of the improvement in right ventricular function in patients with severe pulmonary hypertension after single-lung transplantation," *Journal of the American College of Cardiology*, vol. 22, no. 4, pp. 1170-1174, Oct. 1993.
- [22] L. Schulman, D.W. Leibowitz, T. Anandarangam, M.R. DiTullio, C.C. McGregor, C.R. Smith and S. Homma, "Variability of right ventricular functional recovery after lung transplantation," *Transplantation*, vol. 62, no. 5, pp. 622-625, Sept. 1996.
- [23] (2016), *Congenital Heart Disease*. Available: [http://www.heartandstroke.com/site/c.ikiQLcMWJtE/b.3484063/k.E84C/Heart\\_disease\\_Congenital\\_heart\\_disease.htm#treatment](http://www.heartandstroke.com/site/c.ikiQLcMWJtE/b.3484063/k.E84C/Heart_disease_Congenital_heart_disease.htm#treatment)
- [24] A. De Luc, L. Stefani, and G. Galanti, "Right ventricle chamber of young trained athletes: morphology and function," *Asian Journal of Sports Medicine*, vol. 4, no. 4, pp.281-288, Dec. 2013.
- [25] F. Maffessanti, D. Muraru, R. Esposito, P. Gripari, D. Ermacora, C. Santoro, G. Tamborini, M. Galderisi, M. Pepi and L.P. Badano, "Age-, body size-, and sex-specific reference values for right ventricular volumes and ejection fraction by three dimensional echocardiography: a multicenter echocardiographic study in 507 healthy volunteers," *Circulation on Cardiovascular Imaging*, vol. 6, no. 5, pp. 700-710, Sept. 2013.
- [26] G. Tamborini, D. Brusoni, J.E. Torres Molina, C.A. Galli, A. Maltagliati, M. Muratori, F. Susini, C. Colombo, F. Maffessanti and M. Pepi, "Feasibility of a new generation three-dimensional echocardiography for right ventricular volumetric and functional measurements," *American Journal of Cardiology*, vol. 102, no. 4, pp. 499-505, Aug. 2008.
- [27] J. Stewart, *Calculus Concepts and Contexts*, Second Edition. Pacific Grove CA: Thomson Learning; 2001; Sect 5.9 pp. 421-422.

- [28] T. Geva, "MRI is the preferred method for evaluating right ventricular size and function in patients with congenital heart disease," *Circulation on Cardiovascular Imaging*, vol. 7, no. 1, pp. 190-197, Jan. 2014.
- [29] M.D. Puchalski, R.V. Williams, B. Askovich, L.L. Minich, C. Mart and L.Y. Tani, "Assessment of right ventricular size and function: echo versus magnetic resonance imaging," *Congenital Heart Disease*, vol. 2, no. 1, pp. 27-31, Jan. 2007.
- [30] T. Kukulski, L. Hubbert, M. Arnold, B. Wranne, L. Hatle and G.R. Sutherland, "Normal regional right ventricular function and its change with age: a Doppler myocardial imaging study," *Journal of American Society of Echocardiography*, vol. 13, no. 3, pp. 194-204, Mar. 2000.
- [31] S.L. Naik, J.J. Rodriguez, K. Nishant and V.L. Sorrell, "Tricuspid annular plane systolic excursion (TAPSE) revisited using CMR," *Journal of Cardiovascular Magnetic Resonance*, vol. 14, suppl. 1, pp. P299-P300, Feb. 2012.
- [32] J.Z. Lee, S.W. Low, S. Yun, P. Dherange, A.A. Desai, E. Juneman, K.S. Lee, P. Suryanarayana, "Comparison of tricuspid annular plane systolic excursion to fractional area change for evaluation of right ventricular systolic function: systematic review and meta-analysis," *Circulation*, vol. 132, suppl. 3, pp. A16722-A16722, Nov. 2015.
- [33] L.G. Rudski, W.W. Lai, J. Afilalo, L. Hua, M.D. Handschumacher, K. Chandrasekaran, S.D. Solomon, E.K. Louie, N.B. Schiller, "Guidelines for the echocardiographic assessment of the right heart in adults: a report from the american society of echocardiography," *Journal of the American Society of Echocardiography*, vol. 23, no. 7, pp. 685-713, Jul. 2010.
- [34] R.C. Gonzalez and R.E. Wood, *Digital Image Processing*, Second Edition. Upper Saddle River NJ: Prentice-Hall; 2002; Sect. 1.1, pp.1-2;
- [35] (2013), K. Ruohonen, *Graph Theory*. Available <http://math.tut.fi/~ruohonen/english.html>.
- [36] E. Kreyszig, *Advanced Engineering Mathematics*, Tenth Edition. Jefferson City MO: John Wiley & Sons; 2011; Sect. 23.2, pp.975;
- [37] E.W. Dijkstra, "A note on two problems in connexion with graphs," *Numerische Mathematik*, vol. 1, no. 1, pp. 370-379, Dec. 1959.
- [38] P.E. Hart, N.J. Nilsson, B. Raphael, "A formal basis for heuristic determination of minimum cost paths," *IEEE Transactions on Systems Science and Cybernetics*, vol. 4, no. 2, pp. 100-107, Jul. 1968.
- [39] R. Bellman, *Dynamic Programming*, 1957, Princeton University Press.
- [40] M. Sonka, V. Hlavac and R. Boyle, *Image Processing, Analysis and Machine Vision*, Fourth Edition. Stanford CT: Cengage Learning, 2015; Sect. 6.2.5, pp. 206-210.
- [41] R.C. Gonzalez and R.E. Wood, *Digital Image Processing*, Second Edition. Upper Saddle River NJ: Prentice-Hall; 2002; Sect. 10, pp.567-568;
- [42] M. Kass, A. Witkin and D. Terzopoulos, "Snakes: Active contour models," *Int. J. Comput. Vis.*, vol. 1, no. 4, pp. 321-331, Jan. 1987.
- [43] C. Davatzikos and J.L. Prince, "An active contour model for mapping the cortex," *IEEE Transactions on Medical Imaging*, vol. 14, no. 1, pp. 65-80, Mar. 1995.

- [44] A.J. Abrantes and J.S. Marques, "A class of constrained clustering algorithms for object boundary extraction," *IEEE Transactions on Image Processing*, vol. 5, no. 11, pp. 1507-1521, Nov. 1996.
- [45] C. Xu and J.L. Prince, "Snakes, shapes, and gradient vector flow," *IEEE Transactions on Image Processing*, vol. 7, no. 3, pp. 359-369, Mar. 1998.
- [46] L. Bing and S. T. Acton, "Active contour external force using vector field convolution for image segmentation," *IEEE Transactions on Image Processing*, vol. 16, no. 8, pp. 2096-2106, Aug. 2007
- [47] S. Osher and J. Sethian, "Fronts propagating with curvature-dependent speed: algorithms based on Hamilton-Jacobi formulations," *Journal of Computer Physics*, vol. 79, no. 1, pp. 12-49, Nov. 1988.
- [48] V. Caselles, F. Catte, T. Coll, and F. Dibos, "A geometric model for active contours in image processing," *Numerische Mathematic*, vol. 66, no. 1, pp. 1-31, Dec. 1993.
- [49] R. Malladi, J.A. Sethian, and B.C. Vemuri, "Shape modeling with front propagation: a level set approach," *IEEE Transactions on Pattern Analysis and Machine Intelligence*, vol. 17, no. 2, pp. 158-175, Feb. 1995.
- [50] T. Chan and L. Vese, "Active contour without edges," *IEEE Transactions on Image Processing*, vol. 10, no. 2, pp. 266-277, Feb. 2001.
- [51] H.K. Zhao, T. Chan, B. Merriman, and S. Osher, "A variational level set approach to multiphase motion," *Journal of Computer Physics*, vol. 127, no. 1, pp. 179-195, Aug. 1996.
- [52] S. Mukherjee and S.T. Acton, "Region based segmentation in presence of intensity inhomogeneity using Legendre polynomials," *IEEE Signal Processing Letters*, vol. 22, no. 3, pp. 298-302, Mar. 2015.
- [53] D. Peng, B. Merriman, S. Osher, H. Zhao, and M. Kang, "A PDE based fast local level set method," *Journal of Computer Physics*, vol. 155, no. 2, pp. 410-438, Nov. 1999.
- [54] C. Li, C. Xu, C. Gui and M. D. Fox, "Distance regularized level set evolution and its application to image segmentation," *IEEE Transactions on Image Processing*, vol. 19, no. 12, pp. 3243-3254, Dec. 2010.
- [55] D.H. Ballard, "Generalizing the Hough transform to detect arbitrary shapes," *Pattern Recognition*, vol. 13, no. 2, pp. 111-122, 1981.
- [56] S. Antunes, C. Colantoni, A. Palmisano, A. Esposito, S. Cerutti and G. Rizzo, "Automatic right ventricle segmentation in CT images using novel multi-scale edge detector approach," *Computing in Cardiology*, vol. 40, pp. 815-818, Sept. 2013.
- [57] S.C. Mitchell, B.P.F. Lelieveldt, R.J. van der Geest, H.G. Bosch, J.H.C. Reiber and M. Sonka, "Multistage hybrid active appearance model matching: segmentation of left and right ventricles in cardiac MR images," *IEEE Transactions on Medical Imaging*, vol. 20, no. 5, pp. 415-423, May 2001.
- [58] P.M. Thompson and A.W. Toga, "Detection, visualization and animation of abnormal anatomic structure with a deformable probabilistic brain atlas based on random vector field transformations," *Medical Image Analysis*, vol. 1, no. 4, pp. 271-294, Sept. 1997.
- [59] T.F. Cootes, C.J. Taylor, D.H. Cooper, and J. Graham, "Active shape models – their training and application," *Computer Vision and Image Understanding*, vol. 61, no. 1, pp. 38-59, Jan. 1995.

- [60] T.F. Cootes, G. J. Edwards and C.J. Taylor, "Active appearance models," *IEEE Transactions on Pattern Analysis and Machine Intelligence*, vol. 23, no. 6, Jun. 2001.
- [61] R.C. Gonzalez and R.E. Wood, *Digital Image Processing*, Second Edition. Upper Saddle River NJ: Prentice-Hall; 2002; Sect. 9.5.4, pp.539-540;
- [62] Y. Lu, P. Radau, K. Connelly, A. Dick and G. Wright, "Automatic image-driven segmentation of left ventricle in cardiac cine MRI," *MICCAI 2009 Workshop on Cardiac MR Left Ventricle Segmentation Challenge, MIDAS Journal*, Sept. 2009.
- [63] S. Huang, J. Liu, L.C. Lee, S.K. Venkatesh, L.L.S. Teo, C. Au and W.L. Nowinski, "Segmentation of the left ventricle from cine MR images using a comprehensive approach," *MICCAI 2009 Workshop on Cardiac MR Left Ventricle Segmentation Challenge, MIDAS Journal*, Sept. 2009.
- [64] C. Casta, P. Clarysse, J. Schaerer and J. Pousin, "Evaluation of the dynamic deformable elastic template model for the segmentation of the heart in MRI sequences," *MICCAI 2009 Workshop on Cardiac MR Left Ventricle Segmentation Challenge, MIDAS Journal*, Sept. 2009.
- [65] J. Wijnhout, D. Hendriksen, H. van Assen and R.J. van der Geest, "LV challenge lkeb contribution: fully automated myocardial contour detection," *MICCAI 2009 Workshop on Cardiac MR Left Ventricle Segmentation Challenge, MIDAS Journal*, Sept. 2009.
- [66] S. O'Brien, O. Ghita and P.F. Whelan, "Segmenting the left ventricle in 3D using a coupled asm and a learned non-rigid spatial model," *MICCAI 2009 Workshop on Cardiac MR Left Ventricle Segmentation Challenge, MIDAS Journal*, Sept. 2009.
- [67] M. Lorenzo-Valdez, G. Sanchez-Ortiz, A. Elkington, R. Mohiaddin and D. Ruecker, "Segmentation of 4D cardiac MR images using a probabilistic atlas and the EM algorithm," *Medical Image Analysis*, vol. 8, no. 3, pp. 255-265, Sep. 2004.
- [68] D. Grosgeorge, C. Petitjean, J.N. Dacher and S. Ruan, "Graph cut segmentation with a statistical shape model in cardiac MRI," *Computer Vision and Image Understanding*, vol. 117, no. 9, pp. 1027-1035, Sept. 2013.
- [69] D. C. Chang and W. R. Wu, "Image contrast enhancement based on a histogram transformation of local standard deviation," *IEEE Transactions on Medical Imaging*, vol. 17, no. 4, pp. 518-531, Aug. 1998.
- [70] S. Timp and N. Karssemeijer, "A new 2D segmentation method based on dynamic programming applied to computer aided detection in mammography," *Medical Physics*, vol. 31, no. 5, pp. 958-971, May 2004.
- [71] Y. Zhang, B. J. Matuszewski, L. K. Shark and C. J. Moore, "A novel medical image segmentation method using dynamic programming," *IEEE International Conference on BioMedical Visualization*, pp. 69-74, Jul. 2007.
- [72] P. K. Bocher and K. R. McCloy, "The fundamentals of average local variance – part I: detecting regular patterns," *IEEE Transactions on Image Processing*, vol. 15, no. 2, pp. 300-310, Feb. 2006.
- [73] *Handbook of Computer Vision Algorithms in Image Algebra*, 2<sup>nd</sup> edition, CRC Press Inc., Boca Raton, FL, 2000, pp. 313.
- [74] L. R. Dice, "Measures of the amount of ecologic association between species," *Ecology*, vol. 26, no. 3, pp. 297-302, Jul. 1945.

- [75] R. D. Fiete and T. Tantaló, "Comparison of snr image quality metrics for remote sensing systems," *Opt. Eng.*, vol. 40, no. 4, pp. 574-585, Apr. 2001.
- [76] D. Arthur, S. Vassilvitskii, "K-means++: the advantages of careful seeding," *Proceeding of the Eighteenth Annual Association of Computing Machinery-Society for Industrial and Applied Mathematics, Symposium on Discrete Algorithms*, pp. 1027-1035, 2007.
- [77] N. Otsu, "A threshold selection method from gray-level histograms," *IEEE Transactions on Systems, Man, and Cybernetics*, vol. 9, no. 1, pp. 62-66, Jan. 1979.
- [78] N.R. Pal and J.C. Bezdek, "On cluster validity for the fuzzy c-means model," *IEEE Transactions on Fuzzy Systems*, vol. 3, no. 3, pp. 370-379, Aug. 1995.
- [79] P. Soile, *Morphological Image Analysis: Principles and Applications*, Second Edition. New York NY: Springer-Verlag, 2004; Sect. 6.3.7, pp. 208.
- [80] P. Soile, *Morphological Image Analysis: Principles and Applications*, Second Edition. New York NY: Springer-Verlag, 2004; Sect. 3.1-3.4, pp. 63-70.
- [81] P. Strandmark, J. Ulén, F. Kahl and L. Grady, "Shortest path with curvature and torsion," *IEEE International Conference on Computer Vision*, pp. 2024-2031, Dec. 2013.
- [82] R.C. Gonzalez and R.E. Wood, *Digital Image Processing*, Second Edition. Upper Saddle River NJ: Prentice-Hall; 2002; Sect. 5.3.2, pp.234;
- [83] M.M. Winter, F.J.P. Bernink, M. Groenink, B.J. Bouma, A.P.J van Dijk, W.A. Helbing, J.G.P. Tijssen and B.J.M. Mulder, "Evaluating the systemic right ventricle by CMR: the importance of consistent and reproducible delineation of the cavity," *Journal of Cardiovascular Magnetic Resonance*, vol. 10, no. 40, pp. 1-8, Jun. 2008.
- [84] J. Schulz-Menger, D.A. Bluemke, J. Bremerich, S.D. Flamm, M.A. Fogel, M.G. Friedrich, R.J. Kim, F. von Knobelsdorff-Brenkenhoff, C.M. Kramer, D.J. Pennell, S. Plein and E. Nagel, "Standardized image interpretation and post processing in cardiovascular magnetic resonance: society for cardiovascular magnetic resonance (SCMR) board of trustees task force on standardized post processing," *Journal of Cardiovascular Magnetic Resonance*, vol. 15, no. 35, pp. 15-35, May 2013.
- [85] W.G. Sullivan, E.M. Wicks and J.T. Luxhoj, *Engineering Economy*, Thirteenth Edition. Upper Saddle River NJ: Prentice-Hall, 2006; Sect. 3.4, pp. 107.
- [86] E. Nagel, H.B. Lehmkuhl, W. Bocksch, C. Klein, U. Vogel, E. Frantz, A. Ellmer, S. Dreyse and E. Fleck, "Noninvasive diagnosis of ischemia-induced wall motion abnormalities with the use of high-dose dobutamine stress MRI: comparison with dobutamine stress echocardiography," *Circulation*, vol. 99, no. 6, pp. 763-770, Feb. 1999.
- [87] (2016), National Electrical Manufacturers Association, *Digital Imaging and Communications in Medicine (DICOM) Standard*. Available: <http://medical.nema.org/>
- [88] M.D. Silver, J.H.C. Lam, N. Ranganathan and E.D. Wigle, "Morphology of the human tricuspid valve," *Circulation*, vol. 43, no. 4, pp. 333-348, Apr. 1971.
- [89] C. Mauerer, R. Qi and V. Raghavan, "A linear time algorithm for computing exact Euclidean distance transforms of binary images in arbitrary dimensions," *IEEE Transactions on Pattern Analysis and Machine Intelligence*, vol. 25, no. 2, pp. 265-270, Feb. 2003.

- [90] L. Lam, L. Seong-Whan and C.Y. Suen, "Thinning methodologies – a comprehensive survey," *IEEE Transactions on Pattern Analysis and Machine Intelligence*, vol. 14, no. 9, pp. 879, Sept. 1992.